UNIVERSITY OF OKLAHOMA

GRADUATE COLLEGE

MODELING CCN EFFECTS ON ELECTRIFICATION WITHIN HIGH AND LOW PRECIPITATION SUPERCELLS

A THESIS

SUBMITTED TO THE GRADUATE FACULTY

in partial fulfillment of the requirements for the

Degree of

MASTER OF SCIENCE IN METEOROLOGY

By

JESSICA P. BLAIR
Norman, Oklahoma
2021

MODELING CCN EFFECTS ON ELECTRIFICATION WITHIN HIGH AND LOW PRECIPITATION SUPERCELLS

A THESIS APPROVED FOR THE
SCHOOL OF METEOROLOGY

BY THE COMMITTEE CONSISTING OF

Dr. Donald MacGorman (Chair)

Dr. Vanna Chmielewski

Dr. Edward Mansell

Dr. Greg McFarquhar

Dr. Jens Redemann

Dr. Micheal Biggerstaff

Acknowledgments

This thesis would not have been possible without the guidance from my advisors, Vanna Chmielewski, Edward Mansell and Donald MacGorman, and suggestions from my entire committee, including Greg McFarquahr, Jens Redemann, and Micheal Biggerstaff. The feedback and advice I received from my committee was priceless and crucial for the development of my thesis. I especially want to thank Vanna Chmielewski and Edward Mansell for the continued support and answers to the multitude of questions that came up throughout my research and thesis. Regarding data support, I want to thank Micheal Biggerstaff for providing the radar data set used in this study and for providing important background on both the data set and Geary, OK case study.

Last, but by far not least, I cannot thank my family and friends enough for the continued support and encouragement throughout my master's. From Massachusetts, New York, and Oklahoma, my support system really helped me get through the tough times and I am very appreciative for that. I especially want to thank my parents, sister, my dog Zoe, Kristy Fitzpatrick, Andjelija Milosevic, and many others!

This thesis was supported by the University of Oklahoma's School of Meteorology, the University of Oklahoma's Cooperative Institute for Mesoscale Meteorological Studies (CIMMS), NOAA's National Severe Storm Laboratory (NSSL), National Science Foundation (NSF) Award #1523331, and NOAA Award #NA16OAR4320115. Computing was executed on the University of Oklahoma Supercomputing Center for Education and Research (OSCER) Schooner supercomputer.

Table of Contents

List Of Tables

List Of Figures

Abstract

Cloud condensation nuclei (CCN) are known to affect both the electrical and the dynamic evolution of storms, but the effects on storm electrification in different storm modes have not been thoroughly examined. We will detail the impacts of CCN in simulations of the high-precipitation Geary, Oklahoma supercell storm from the Thunderstorm Electrification and Lightning Experiment (TELEX) on 29-30 May 2004, as well as in the simulations of the lower-precipitation Kimball, Nebraska supercell storm from the Stratosphere-Troposphere Experiment: Radiation, Aerosols, and Ozone-A (STERAO-A) on 10 July 1996. The simulations were run and analyzed using five different CCN concentrations (100, 300, 500, 1000, and 2000 cm^{-3}) in the Collaborative Model for Multi-scale Atmospheric Simulation (COMMAS), a three-dimensional cloud model using a three-moment microphysics scheme with six hydrometeor types, and with a bulk electrification scheme utilizing both inductive and non-inductive charging. The simulations provide details on changes in storm dynamics, kinematics, and electrification as a function of a controlled change in a single variable, the CCN. The CCN concentration of each model run significantly affected the storm dynamics, kinematics, and electrification in both storms. There were differences in storm polarity and charging rates across the different CCN concentrations.

Similar patterns were observed in both case studies. In both case studies, very low CCN concentrations had opposite vertical polarity structure than that of higher CCN concentrations in our control simulations. The overall evolution of the storm also differed with CCN concentration including the spatial extent (horizontal and vertical), lifetime of the storm, as well as the evolution of warm and cold rain processes. These variables were analyzed and compared for both the TELEX and STERAO-A case studies. Upon analysis, differences due to CCN concentration were present regardless of amount of precipitation within the storm. Further sensitivity studies were conducted

using two non-inductive charging and microphysics schemes. Results from the simulations of both case studies were compared to observations collected during the TELEX and STERAO-A field campaigns.

Chapter 1

Introduction

The electrical structure of a thunderstorm is closely related to the microphysical composition of the storm. Aerosols that act as cloud condensation nuclei (CCN) can significantly impact the microphysical, electrical, and dynamic structures of a thunderstorm (Tao et al., 2012). Past studies have noted these impacts observationally and numerically, some of which are described below, but the full extent of CCN effects on thunderstorm structures has yet to be studied in all storm modes. Cloud-aerosol processes are still not fully understood, yet anthropogenic aerosols have a significant impact on radiative and convective properties of clouds. The Intergovernmental Panel on Climate Change (IPCC) lists aerosol indirect effects as one of the key uncertainties in our changing environment in their fourth and fifth annual reports (Solomon et al., 2007; Stocker et al., 2013). Although the scale of these effects may initially be on the microphysical scale, when summed over larger spatial and temporal scales they can be significant. Better understanding these integrated processes over various storm modes and environments provides a more detailed picture of the effect CCN has on the electric and dynamic structure of supercells, as well as the potential severe weather threats of a changing environment.

Also originating at the microphysical scale, non-inductive collisional charging is believed to be the primary driver of thunderstorm electrification and occurs primarily in the mixed phase region of the storm where ice crystals, riming graupel, and supercooled liquid water are all present (Reynolds et al., 1957; Takahashi, 1978; Saunders and Peck,

1998; Saunders et al., 2006). Net charge and ice mass are transferred during collisions of riming graupel and ice crystals (Mason and Dash, 2000). The polarity of the charge transferred is dependent on ambient temperature, liquid water content, and impact speed of the colliding particles. Many laboratory experiments have been conducted (e.g., Takahashi, 1978; Jayaratne and Saunders, 1983; Pereyra et al., 2000; Saunders et al., 1991; Saunders and Peck, 1998; Saunders et al., 2006) to determine net polarity of riming graupel electrification following a rebounding collision. It has been hypothesized that whichever particle is growing more rapidly by vapor diffusion gains a net positive charge during the rebounding collision (Baker et al., 1987) through the transfer of mass from the quasi-liquid layer surrounding each particle (Baker and Dash, 1994). There is substantial uncertainty stemming from the various constraints of the laboratory studies which have been performed, and thus there are multiple non-inductive electrification parameterizations (Fig. 1.1) available for modeling the electric structure of storms, a single one of which may not be fully representative of electrification as it occurs in nature (Saunders et al., 2006; Mansell et al., 2005).

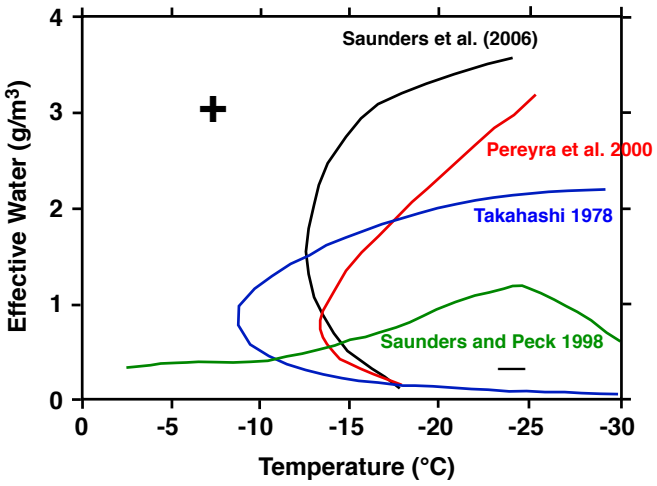

Figure 1.1: Non-inductive charge separation sign-reversal curves for Takahashi (1978); Pereyra et al. (2000); Saunders and Peck (1998); Saunders et al. (2006). [Figure adapted from Saunders et al. (2006)]

How the particles separate net charge in the mixed phase region of the storm will later determine the storm's charge structure. After particles separate charge on the microphysical scale, storm kinematics and differential fall speeds control the motions of these particles resulting in large-scale charge separation and the formation of net charge layers or regions. Updrafts advect cloud ice to relatively high altitudes in the storm, while denser hail and graupel remain at lower altitudes of the storm via differential sedimentation. The magnitude of charge separated ultimately depends on the number and size of colliding particles, liquid water content and ambient temperature. The typical charge structure of an unsheared thunderstorm is a positive-negative-positive vertical charge layer structure (Fig.1.2b), also referred to as a positive (normal) tripole structure (e.g., Williams, 1989). In the normal tripole structure, following collisions at high altitudes and cold temperature within the mixed phase region, negatively charged

graupel tends to accumulate in the middle of the cloud and positively charged ice crystals are carried up to higher parts of the cloud. At some lower altitude and warmer temperatures determined by the reversal curve, the polarities reverse with negatively charged ice crystals congregating in the middle layer, and positively charged graupel sedimenting in the bottom layer. The polarity reversal is a function of ambient temperature, liquid water content, and impact speed of the colliding particles. These reversal curves have been studied in various laboratory experiments, as mentioned above. An inverted (anomalous, negative) tripole structure (Fig.1.2d) would have vertical charge layers in a negative-positive-negative order (Marshall et al., 1995). Storms can also have a dipole structure, where only two main vertical charge layers exist. A positive dipole structure (Fig.1.2a) would be a positive layer over a negative layer of charge, while an inverted dipole structure(Fig.1.2c) would be reversed (Seimon, 1993).

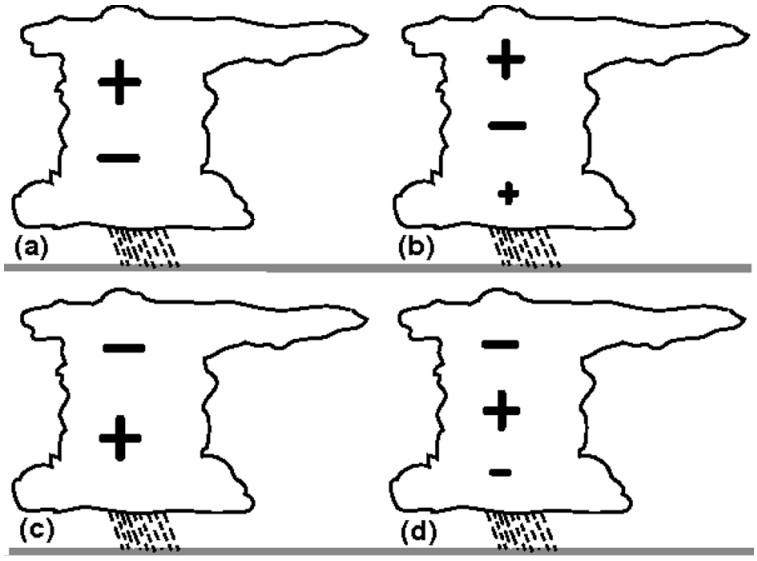

Figure 1.2: Conceptual model of charge structure of a thunderstorm. (a) Normal dipole model, containing upper positive and lower negative charge centers. (b) Normal tripole model, containing upper positive, main negative, and smaller lower positive charge centers. (c) Inverted dipole, lower positive charge and upper negative charge centers. (d) Inverted tripole, main positive with upper and lower negative charge centers. [Figure and caption adapted from Kuhlman et al. (2005)].

Adding vertical wind shear to the environment or turbulent motions within the storm add a horizontal component to the particle motions impacting charge separation and horizontal inhomogeneities in the microphysical environment, which can impact the polarity or magnitude of hydrometeor electrification. With the addition of vertical wind shear, the charge structure of supercells can be rather complicated. Current dipole/tripole models are too simplistic to apply to all mature thunderstorms and mesoscale convective systems (Rust and Marshall, 1996). Stolzenburg et al. (1998) suggested a more complex charge structure for high shear thunderstorms, consisting of four main charge regions near the updraft and six charge regions outside the updraft in the convective precipitation region. In severe storms, typically a lot of small pockets of

charge exists in the vicinity of the updraft. Brothers et al. (2018) through simulations found charge advection tendency was more textured inside the updraft region of the storms where more resolved eddy-rich flow was present. Despite the complexity of the net charge, however, the potential was much simpler and reflected the local charge sedimentation tendency, which ultimately determines the lightning structure.These small pockets of high electric potential are more conducive to more numerous and smaller flashes, which is especially seen around the updraft region where charge structures tend to be more complex (Bruning and Macgorman, 2013).

The environmental CCN concentration significantly influences the microphysics of warm and cold rain processes, thereby affecting the process of non-inductive charging. CCN serve as the key ingredient of heterogeneous droplet nucleation in warm rain processes (Pruppacher and Klett, 1978). For cold rain processes, ice nuclei (IN) are needed for heterogeneous nucleation. Not every aerosol will serve as a good IN particle, so changes made to CCN concentration would have a more direct effect on warm than on cold rain processes. Although homogeneous droplet nucleation is possible in laboratory experiments, the extreme supersaturation required for this process is not typically found in nature. In convective clouds, an increase in CCN results in more numerous liquid droplets with a smaller radius, resulting in a narrower drop size distribution. Environments with a large number of CCN and a narrow drop size spectrum, produce weak collision and coalescence processes resulting in suppressed or delayed onset of precipitation (Twomey, 1977; Albrecht, 1989; Gunn and Phillips, 1957). Polluted mixed-phase clouds typically contain relatively high concentrations of ice (Lance et al., 2011). Higher ice concentrations can be a result of delayed warm-rain processes preserving a larger cloud water content to low temperatures. Small droplets are easily lofted into the colder levels of the cloud and reaching homogeneous freezing

temperatures, resulting in a high concentrations of ice particles at upper levels which might influence the charging mechanisms aloft.

The microphysical impact aerosols have on thunderstorms further extends into the large-scale dynamics of the storm. A higher concentration of CCN leads to increased latent heat release by both condensational and freezing processes within mixed phase clouds (Li et al., 2011; Rosenfeld et al., 2008; Khain et al., 2005). An increase in latent heat release invigorates convection, enhancing updrafts and encouraging secondary convection; however, an excess of CCN can result in suppression of the coalescence and collision processes and result in a weaker storm. Fan et al. (2009) found invigoration of convective strength by aerosols in cases where weak windshear is present but found the contrary to be true under strong wind shear. As an updraft becomes more vigorous, more hydrometeor mass is lofted into the mixed phase region of the storm instead of falling out as precipitation. This in turn causes charge separation to occur more rapidly, as more particles are colliding in mixed phase regions. It can also eventually result in turbulent structures at the interface of the updraft, which produce a lot of small flashes in the updraft region and thereby enhance overall flash rates more than a simple increase in charging rates would imply (Bruning and Macgorman, 2013).

Observationally, impacts of CCN on lighting and thunderstorm charge structures have been inferred by using remote satellite data and various lightning ground networks to understand the cloud's composition and structure. Many of these studies have been conducted over urban areas (e.g., Pawar et al., 2017; Hu et al., 2019; Ren et al., 2018; Sun et al., 2021) or in the vicinity of wildfires (e.g., Kochtubajda et al., 2011; Altaratz et al., 2010). Hu et al. (2019) compared CCN retrievals from the Visible Infrared Imaging Radiometer Suite (VIIRS) onboard the Suomi National Polar-Orbiting Partnership (NPP) satellite with measurements by polarimetric radar and a Lightning Mapping Array (LMA) in the Houston, Texas region. This study a found positive relationship

between CCN concentrations and convective intensity as measured by maximum echo top height below concentrations of 1,000 CCN cm^{-3}. Hu et al. (2019) also found that lightning flash rates increased by an order of magnitude between CCN concentrations of 400 to 1,000 cm^{-3} but decreased beyond that. This is similar to the findings of Altaratz et al. (2010); Pawar et al. (2017); Ren et al. (2018), and Kochtubajda et al. (2011), which all found positive relationships between flash rates and aerosols concentrations until a threshold concentration. Ren et al. (2018) found this pattern of enhanced lighting at higher CCN was more evident when convective available potential energy (CAPE) values were low and wind shear weak. It has also been suggested that aerosols can influence the development of net charge structures in a storm. Pawar et al. (2017) found thunderstorms with inverted polarity occurred on days with significantly higher (Aerosol Optical Depth) AOD than days with more normal polarity non-severe thunderstorms, however many other variables showed strong correlations to inverted polarity days, such as high dewpoint depressions. Kochtubajda et al. (2011) suggested the presence of smoke with elevated cloud bases may have contributed to enhanced +CG production, indicative of anomalous charge structures. Kochtubajda et al. (2011) also found positive peak current strengths during wild fire season increased by more than 30 kA, while the negative peak current strengths were weaker than climatology by as much as 20kA. The downside of these observational studies is that much of the data from satellites and ground networks only give a partial picture of the processes occurring within the cloud. The natural environment changes quickly and has many variables, so it is hard to find a pure comparison between different CCN concentrations within an otherwise uniform environment.

Idealized simulations in numerical models can be used to isolate the response of such electric and dynamic properties to changes made solely to CCN concentration, while holding all other environmental conditions constant. Similar to the observational

studies, CCN impacts on the electrical structure of thunderstorms have been investigated using numerical models (e.g., Mitzeva et al., 2006; Zhao et al., 2015; Mansell and Ziegler, 2013; Sun et al., 2021). Mansell and Ziegler (2013) modeled CCN effect on updraft volume, speed, and electrification on a low-shear ordinary thunderstorm and found lightning rates had a weak response to CCN concentrations below 700 cm^{-3}, until Hallett-Mossop rime-splintering ice multiplication becomes more active. However, beyond that point, rates increased with increasing CCN and until very high concentrations. Mansell and Ziegler (2013) also found that high CCN concentrations acted to invigorate updrafts via increased latent heat release and resulted in suppression of precipitation. Sun et al. (2021) and Zhao et al. (2015) found delays in lightning activity and higher charge densities in polluted air than clean air, as a result of more ice particles participating in the electrification process. In polluted cases, Zhao et al. (2015) and Mitzeva et al. (2006) found that aerosol loading led to increased cloud water content, which resulted in more negative charging aloft and the addition of an upper-level negative charge region, above the main positive charge center, which was weaker on non-existent in their clean/maritime simulations. This implies a change in the active non-inductive electrification regimes experienced within the storms. These studies all link the changes in the electric structure to the effect aerosols have on the microphysical and dynamic processes occurring within the storm.

Numerical studies have also found the dynamic evolution of the storm to be sensitive to CCN concentrations (e.g., Storer et al., 2010; Seigel and Van Den Heever, 2012; Kalina et al., 2014; Lerach and Cotton, 2012; Khain et al., 2011). Storer et al. (2010) modeled aerosol impacts on convective storms in different environments. They found that in more polluted simulations, surface rainfall rates and evaporative cooling near the surface was lower and therefore affected the extent and depth of cold pool formations, which was also found in the studies by Lerach and Cotton (2012) and Khain et al.

(2011). The formation of the cold pool further affected the evolution of the strength and spatial extent of storm. Storms in environments with lower aerosols had larger and deeper cold pools, and the storms themselves had a larger spatial extent with a longer life span (Storer et al., 2010). In a two-dimensional model framework, Khain et al. (2011) found that the reaction of cold pool formations to different CCN concentrations was highly dependent on environmental conditions, where under relatively dry low-level conditions cold pools were smaller at high CCN, but with moist low-level conditions with moderate vertical wind shear, the cold pool area is nearly constant with respect to CCN concentration. Storer et al. (2010) also found that many of the changes seen because of varying aerosol concentrations were of either the same order or larger magnitude than those brought about by changing the convective environment in terms of CAPE.

In this paper, we present sensitivity studies on how CCN affects the dynamic and electric structure in two different supercell regimes using the Collaborative Model for Multi-scale Atmospheric Simulation (COMMAS) model. Sensitivity studies were conducted to test the reaction of microphysical and dynamic processes to various CCN concentrations. These sensitivities were compared in simulations of both the high-precipitation (HP) Geary, Oklahoma supercell storm from the Thunderstorm Electrification and Lightning Experiment (TELEX) on 29-30 May 2004 and the low-precipitation (LP) Kimball, Nebraska supercell storm from the Stratosphere-Troposphere Experiment: Radiation, Aerosols, and Ozone-A (STERAO-A) on 10 July 1996. This thesis is organized as follows: Chapter 2 presents data and methodology used in the study, Chapters 3 & 4 presents the modeling results of the HP and LP case studies respectively, Chapter 5 provides a comparison of the simulated supercells to observational data from both case studies, and Chapter 6 completes this thesis with discussion and conclusions.

Chapter 2

Data/Methods

In this study, five CCN concentrations (100, 300, 500, 1000, and 2000 cm^{-3}) will be compared in two different case studies; the high precipitation supercell from the TELEX field campaign and the low-precipitation supercell from the STERAO-A field campaign as described below. These simulations were run using two different non-inductive charging schemes (Takahashi, 1978; Saunders and Peck, 1998), and resulting changes in the electrical characteristics of the storms were compared with a single microphysics scheme. As a sensitivity test, simulations with these five concentrations were also completed using both the two-moment (2M) and three-moment (3M) options of the National Severe Storms Laboratory (NSSL) microphysics scheme (Mansell et al., 2010) with a single electrification scheme. This resulted in a total of 15 simulations for each case study. Radar data were available from both cases, but only TELEX had three-dimensional observations of total lightning activity. Thus, results from the simulations of the Geary, Oklahoma storm were compared with observed electrical, as well as kinematic, characteristics for this case. While the STERAO-A simulations are only compared to the observed kinematic characteristics.

2.1 Model Background

2.1.1 Numerics

All simulations were run using the Collaborative Model for Multi-scale Atmospheric Simulation (COMMAS) model, a three-dimensional cloud model (Wicker and Wilhelmson, 1995) which incorporates parameterizations of lightning and both inductive and non-inductive charging (Mansell et al., 2010). The model uses the basic equation set from Klemp and Wilhelmson (1978) for momentum, pressure, potential temperature, and turbulence kinetic energy (Coniglio et al., 2006). The model used a third-order Runge-Kutta time integration scheme (Wicker and Skamarock, 2002), with fifth-order upwind differencing on the first two iterations and ninth-order weighted essentially non-oscillatory (WENO) scheme on the final step (Jiang and Shu, 1996; Shu, 2003; Balsara and Shu, 2000).

2.1.2 Microphysics

The model describes form and phase changes among six hydrometeor types: cloud droplets, raindrops, cloud ice crystals, snow particles, hail, and graupel. The microphysics schemes used in these simulations were adapted from Ziegler (1985) and Straka and Mansell (2005). The scheme predicts both the mixing ratio (3rd moment) and number concentration (zeroth moment) for the six hydrometeor categories, and the three-moment version further predicts the reflectivity (6th moment) for rain, graupel, and hail. Bulk particle density is predicted for graupel and hail. This is further described in Mansell et al. (2010) and Dawson et al. (2014). Hydrometeor size distributions are assumed to follow a gamma function distribution. Microphysical processes include cloud droplet and cloud ice nucleation, condensation, deposition, evaporation,

sublimation, collection–coalescence, variable-density, riming, shedding, ice multiplication, cloud ice aggregation, freezing and melting, and conversions between hydrometeor categories (Mansell and Ziegler, 2013). The model does not assume any aerosol type and CCN concentration is predicted with a bulk activation spectrum ($NCCN_a$=CCN $\times$ S^k,where k= 0.6, $NCCN_a$= number of activated CCN, and S= supersaturation) tracking the number of un-activated CCN and depleting local CCN concentrations as particles becomes activated (Mansell et al., 2010; Mansell and Ziegler, 2013). CCN particles are subject to advection and subgrid mixing via turbulence but have no other interactions with hydrometeors. Initial CCN concentrations are initialized to have a constant number mixing ratio (# kg^{-1}) across the domain and are assumed to be well mixed. Initial concentrations are scaled by sea-level air density (CCN(z) = CCN_{base} $[\rho_{air}(z)/\ \rho_o]$), following that in Mansell and Ziegler (2013).

2.1.3 Electrification

COMMAS has options for various bulk non-inductive (NI) charging schemes as well as inductive (or polarization) graupel-droplet charging. Both NI and inductive charging are utilized in this study. Laboratory and modeling experiments suggest that NI charging is the primary process responsible for generating large electric fields within storms (e.g., Saunders and Peck, 1998; Takahashi, 1978; MacGorman and Rust, 1985). NI charging is used in the model when riming graupel and ice crystals/snow collide and rebound in the presence of supercooled water. In this study we will compare results using the Takahashi (1978) NI electrification scheme (henceforth TAK; Fig. 2.1) to simulations using the NI electrification parameterization based on the results of the Saunders and Peck (1998) laboratory experiments (henceforth SP98; Fig. 2.2). The SP98 scheme has been modified to follow Brooks et al. (1997) for temperatures above -15^{o}C (T>-15^{o}C) (Mansell et al., 2010). More information on this scheme and its

modification can be found in Calhoun et al. (2014). SP98 determines sign of charge exchanged between rebounding particles as a function of rime accretion rate (RAR) and ambient temperature. The sign and magnitude of the charge transferred to the graupel during a rebounding collision is strongly influenced by the amount of water accreted on the graupel (i.e., the rimer) as negative charge typically goes in the direction of mass transfer. In the TAK scheme the sign of charge transferred to rimer during a rebounding collision depends on cloud water content and temperature (Takahashi, 1978), with a weaker dependence on crystal size and impact speed (Takahashi, 1984).

There are a couple of methods through which inductive charging occurs. Inductive charging occurs in the presence of an electric field when two polarized hydrometeors pass charge upon a rebounding collision. It is believed to also affect a storm's charge structure, but not to the same magnitude as NI charging (Mason 1988; Brooks and Saunders 1994). The model assumes that, in the presence of an electric field, inductive charge transfer during collisions between frozen particles is too slow to have a significant effect and collisions between liquid particles are likely to result in coalescence rather than charge exchange. Thus, inductive collisional charging only occurs in the model when graupel and hail undergoing dry growth collide and rebound with water droplets Hydrometeors can also gain (or lose) charge via attachment of free ions under the influence of both the pre-existing hydrometeor charge and the ambient electric field, another inductive charging method. For example, electric fields outside a cloud can drive ion currents that attach to cloud particles at cloud edges to form screening charge layers. More details of the non-inductive and inductive charging parametrizations can be found in Mansell et al. (2005).

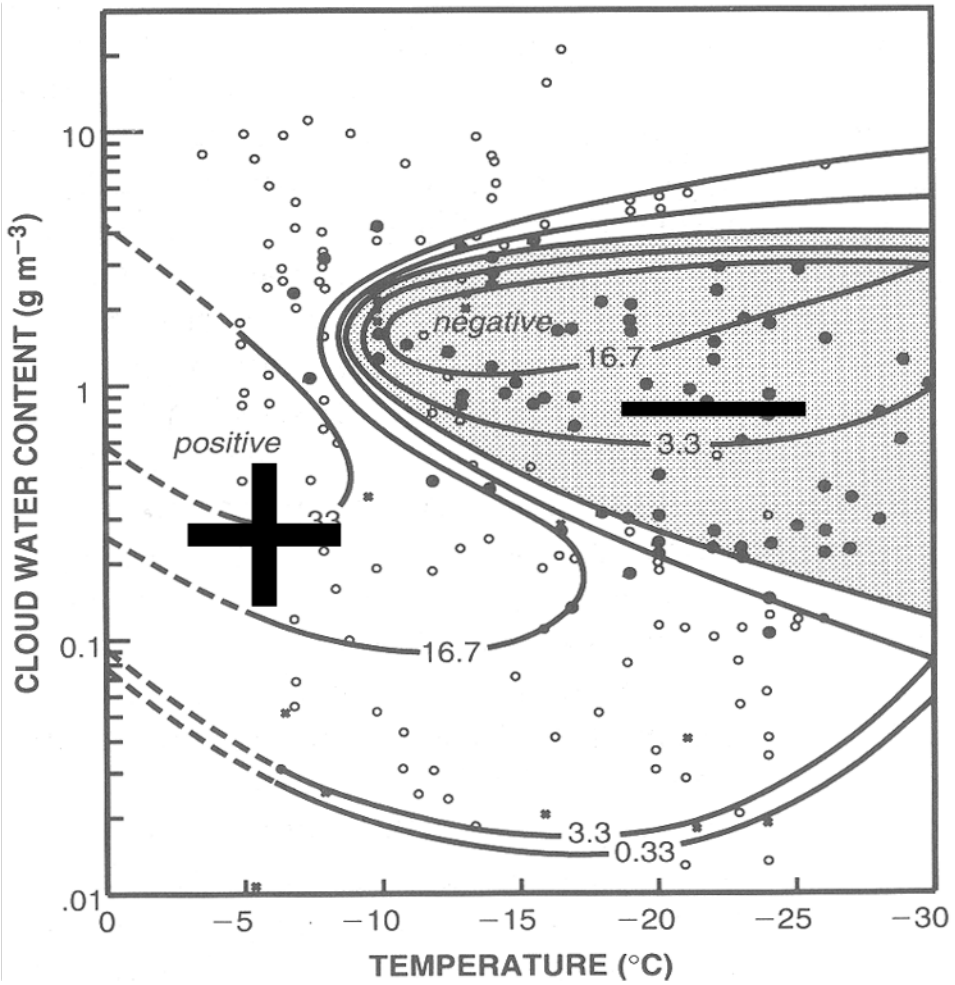

Figure 2.1: Electrificiation of rime using drop distributions. open circles show positive charge, solid circles negative charge and crosses represent uncharged cases. The electric charge of rime per ice crystal collision is shown in units of 10^{-4} esu given by the contours. [Adapted from Takahashi (1978).]

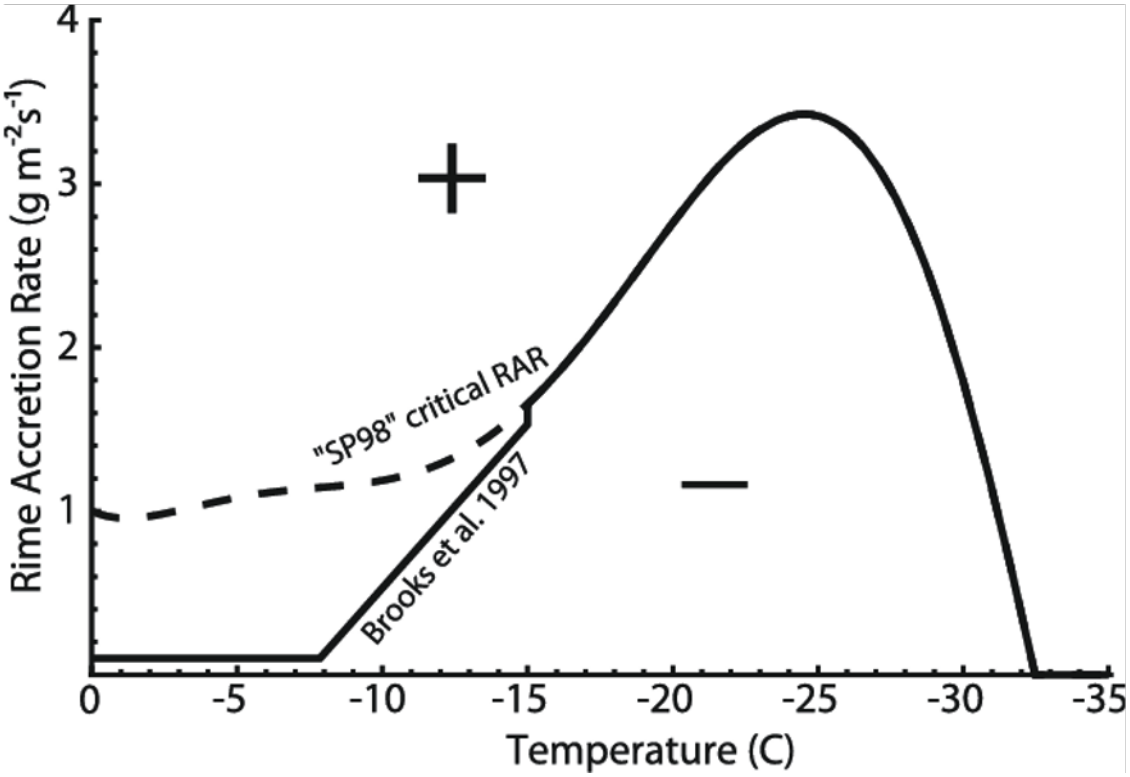

Figure 2.2: Non-inductive charge separation sign-reversal curve by the polarity of the charge transferred to the rimer. The critical RAR curve follows Saunders and Peck (1998) for T < -15^{o}C (shown as dashed curve for T > -15^{o}C) and Brooks et al. (1997) at warmer temperatures. Charge transfer is set to zero for T < -33^{o}C. [Adapted from Mansell et al. (2010).]

The charge density on each of the six hydrometeor types is explicitly predicted from collisions rates between the various types and is transferred between categories in proportion to the mass transferred from one category to another. Charge is conserved within the model domain and follows the charge continuity equation from Mansell et al. (2005). Charge is not completely conserved, however, due to charge movement from ion currents entering or exiting the domain, advection through a lateral boundary, or transport to ground by lightning. Conservation equations account for both positive and

negative ions and take into account advection, mixing, drift motion (ion motion induced by the electric field), cosmic ray generation, ion recombination, ion attachment to hydrometeors, corona discharge from the ground, and release of ions from evaporating hydrometeors (Mansell et al., 2005). A fair-weather state is also implemented from Gish (1944) and includes background ions generated by cosmic rays.

Lightning flashes are parameterized by a stochastic dielectric breakdown model as described by Mansell et al. (2002, 2005). A flash is initiated when the electric field magnitude exceeds a height-dependent threshold for breakdown. A flash's lightning channels are then simulated by a stochastic 3D-branched parameterization, in which positive (negative) leaders having very high conductivity carry positive (negative) charge and tend to propagate preferentially through regions of net negative (positive) charge density (MacGorman et al., 2001; Mansell et al., 2002) until the electric field at the tip of the channel drops below the threshold for continued propagation. As the flash develops, the electric potential of each point on the conducting channels is computed. After the propagation of all channels in a flash ends, the charge on channels is computed by Gauss's Law from the difference in potential compared with the points surrounding each channel. The resulting lightning charge is deposited at each point on the channel as small ions (Mansell et al., 2010).

2.1.4 Model Domain and Initialization

For the Geary, OK case study, the model was initialized to be horizontally homogeneous in an environment (Fig. 2.3) based on the combination of two soundings. Below 400 mb, the sounding was taken from an environmental sounding released near Weatherford, OK and above 400 mb, the data were from the sounding released at the Norman, OK, National Weather Service office at 0000 UTC (Fig. 2.4). This is similar to the sounding used by Calhoun et al. (2014) except it has been smoothed to remove neutral layers

(personal communications, C. Zeigler 2021). A single thermal bubble (3K) was inserted into the boundary layer to initiate convection. The bubble has a horizontal radius of 10 km and a vertical radius 1.4 km. The size of the model domain was 100 km x 120 km x 24 km, with a horizontal grid spacing of 500 m and a vertical grid spacing of 200 m stretched to a maximum of 500 m at 20 km over 63 grid points. The model was run for 4 hours with a time step of 1 second.

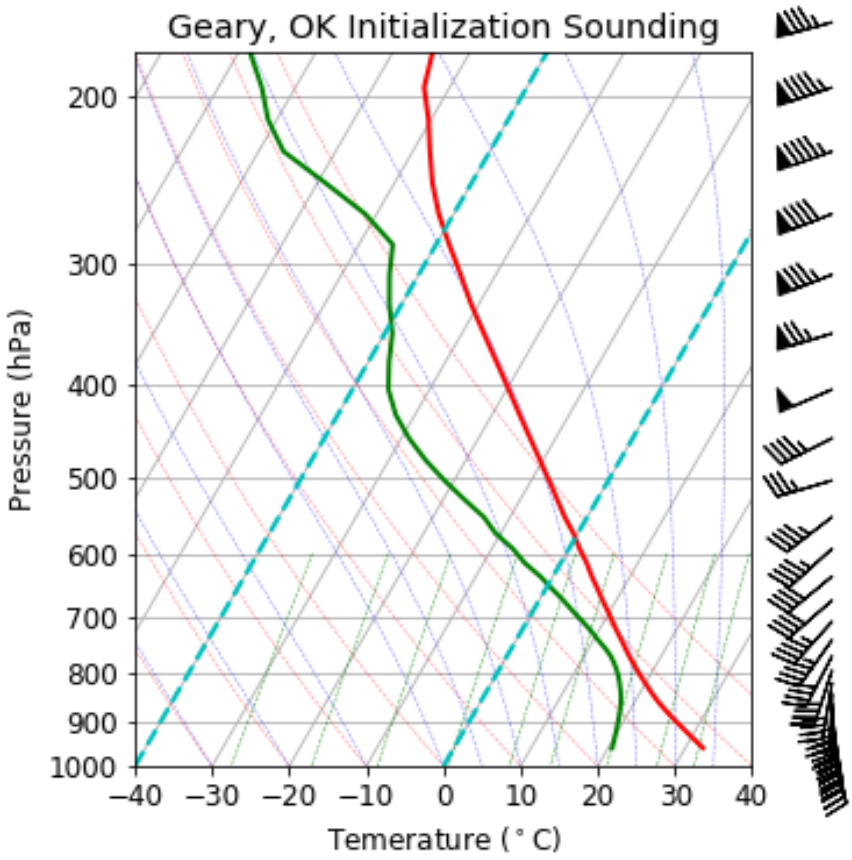

Figure 2.3: Initialization atmospheric sounding used to simulate Geary, Oklahoma case study

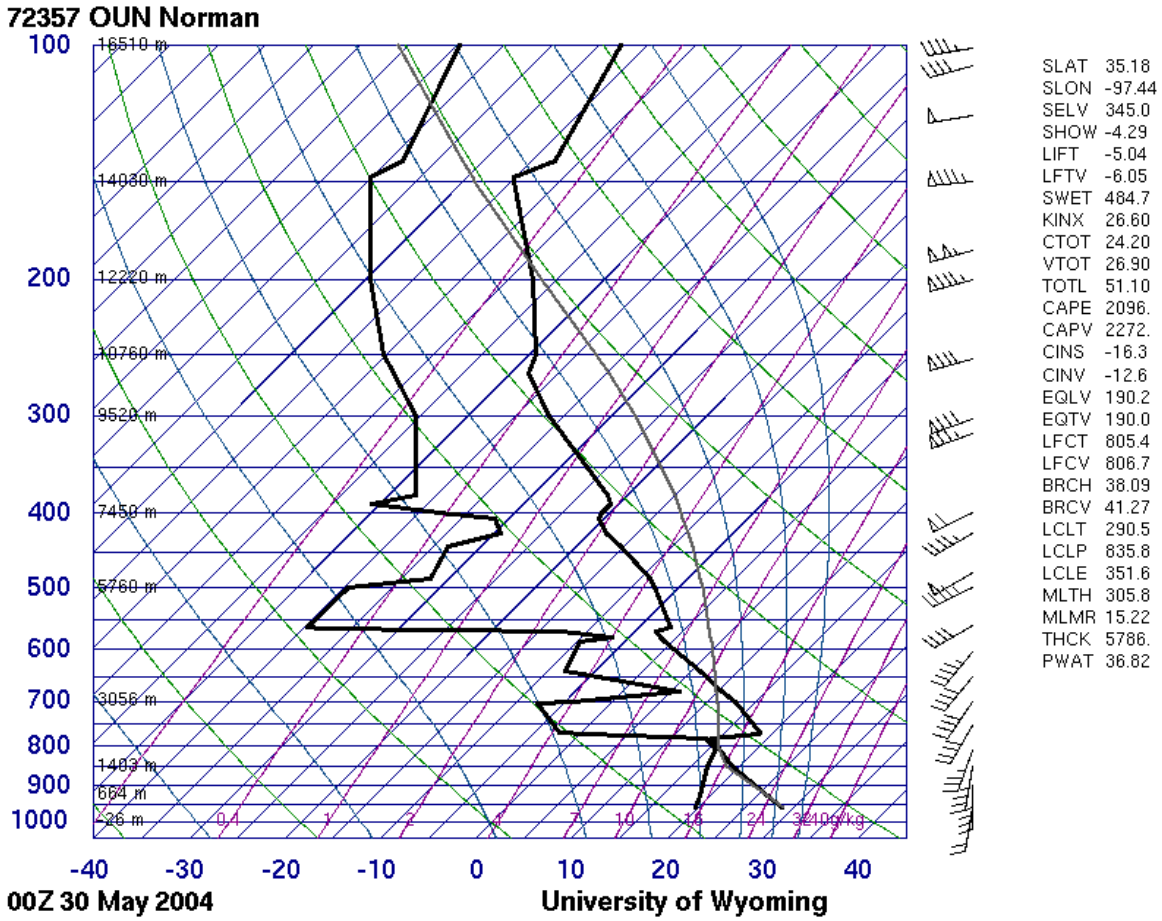

Figure 2.4: Atmospheric Sounding launched from Norman, Oklahoma NWS (OUN) at 0000 UTC 30 May 2004 (Plot courtesy of the University of Wyoming [2])

The Kimball, NE simulation also used a horizontally homogeneous environment based on the sounding from Skamarock et al. (2000)(Fig.2.5). A simple thermal impulse was unable to sustain convection, so in this case a forcing region in the boundary layer initiated convection with a vertical acceleration term. The region has a horizontal radius of 10 km and a vertical radius 1.4 km and a central acceleration of 0.06 m s^{-2}, and the forcing was maintained for the first 30 minutes of the simulation. The size of the model domain was 100 km x 100 km x 24 km, with a horizontal grid spacing of

[2]http://weather.uwyo.edu/upperair/sounding.html

500 m and a vertical grid spacing of 200 m stretched to a maximum of 500 m at 20 km over 63 grid points. The model was run for 3 hours with a time step of 2 seconds.

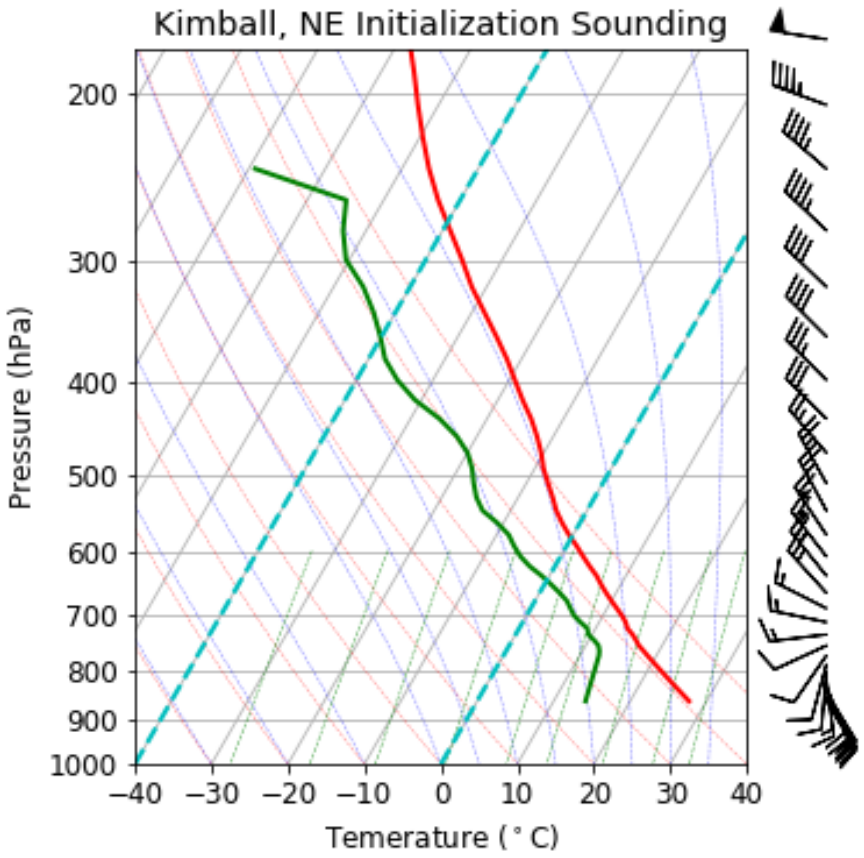

Figure 2.5: Initialization atmospheric sounding used to simulate Kimball, NE case study

2.2 Overview of Observed Storms

2.2.1 Geary, OK Case Study

The Geary, Oklahoma supercell began late on 29 May 2004 in west-central Oklahoma, roughly 45 miles west of Oklahoma City, and lasted 12 hours into 30 May. This storm

was an intense isolated high-precipitation supercell which underwent a storm split early in its lifecycle. It produced 18 tornadoes before decaying near the Arkansas-Oklahoma border (Potvin et al., 2013; Calhoun et al., 2013; Betten et al., 2018). This event was documented as part of the Thunderstorm Electrification and Lightning Experiment (TELEX) field campaign, which was focused on exploring the relationship of storm electrification and lightning to storm dynamics and microphysics. TELEX concentrated multiple observational resources on this supercell storm until it passed east of Oklahoma City (Calhoun et al. 2014). Due to the comprehensive documentation of this case, multiple observational and numerical studies have focused on this storm (e.g., Potvin et al., 2013; Calhoun et al., 2013; Betten et al., 2018). Similar to the analyses in previous studies, this study will mainly focus on the right-mover. Storm analysis will be taken from the 90-minute period of 2350-0120 UTC, analyzed by Betten et al. (2018).

The synoptic set-up for this event included a broad upper-level trough over the northwest United States and a short ridge over the Mississippi valley. A deepening surface low was located over southeastern Colorado and propagated eastward into Kansas through the analysis time (Calhoun et al., 2013). In the mid-levels, westerly winds advected warm dry air, setting up an elevated mixed layer as observed in the 0000 UTC 30 May upper-air sounding launched from Norman, OK (OUN; Fig. 2.4). Low-level southerly winds advected warm moist air from the Gulf of Mexico. Temperatures in the 0000 UTC sounding were super-adiabatic from the surface up until 800 mb and created a capped environment, with roughly 2100 J Kg $^{-1}$ of CAPE above the cap. The storm was initiated by an approaching dryline around 2130 UTC 29 May (Betten et al., 2018). Dewpoints ahead of the dryline ranged from 20 to 22^{o}C and behind it ranged from -8 to -3^{o}C, marking a large axis of instability. Further details on this evolution can be found in Calhoun et al. (2013) and Betten et al. (2018).

2.2.2 Kimball, NE Case Study

The Kimball, Nebraska supercell began 10 July 1996 near the southern end of the Wyoming-Nebraska border, along the Cheyenne Ridge and traveled south-southeast into Colorado. This storm was part of the Stratosphere-Troposphere Experiment: Radiation, Aerosols, and Ozone-A (STERAO-A) field experiment, which was focused on understanding thunderstorms' roles in the distribution of chemical components in the troposphere, especially NO_x production by lightning and NO_x transport by convective and mesoscale features. Multiple numerical studies have analyzed this particular storm (e.g., Skamarock et al., 2000; Lang et al., 2000; Barth et al., 2007; Dye et al., 2000). It was a single, intense low-precipitation storm that evolved from a multicellular line of storms.

Synoptic conditions for this case included a broad ridge over the southern plains, and an upper-level shortwave trough that propagated from northwest New Mexico eastward into the region. This shortwave passed through too early in the period (1200 to 0000 UTC, 10-11 July) to serve as a forcing mechanism for the observed convection of that day. A surface stationary front extending from Western South Dakota down through eastern New Mexico served as a baroclinic zone with cool moist air (dew points from 13 to 16^{o}C) to the east and warm dry air (dew points from 3 to 10^{o}C) to the west of the boundary (Skamarock et al., 2000). On the warm side, the 0000 UTC upper-air sounding from Denver (Fig. 2.6), Colorado (DNR) shows a very dry boundary layer, with easterly surface winds veering with height. On the cool side, the 0000 UTC sounding from Dodge City, Kansas (DDC; Fig. 2.7) shows a moist boundary layer extending up to about 850 mb, with southeasterly surface winds also veering with height. The DDC sounding showed a strong cap which would prevent any surface-based convection.

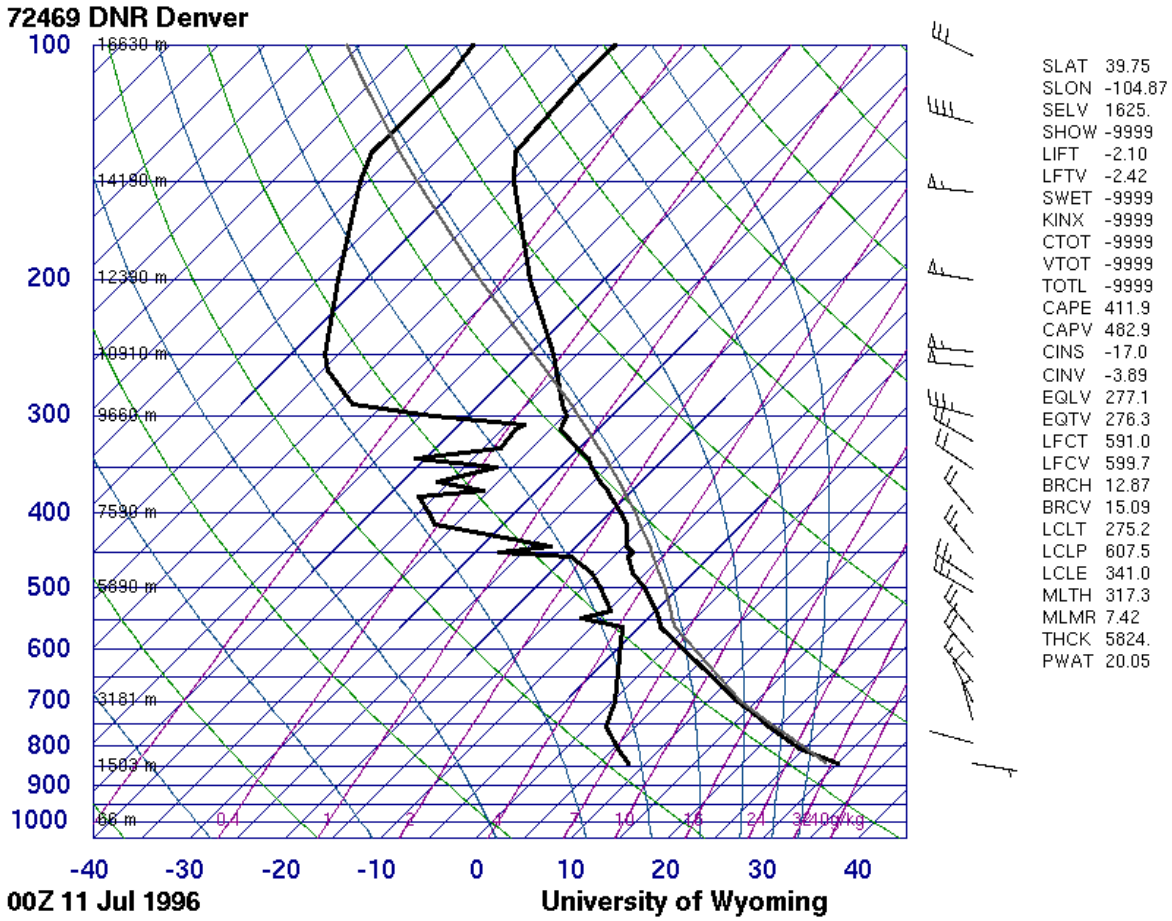

Figure 2.6: Atmospheric Sounding launched from Denver, Colorado NWS (DNR) at 0000 UTC 11 July 1996 (Plot courtesy of the University of Wyoming[4])

[4]http://weather.uwyo.edu/upperair/sounding.html

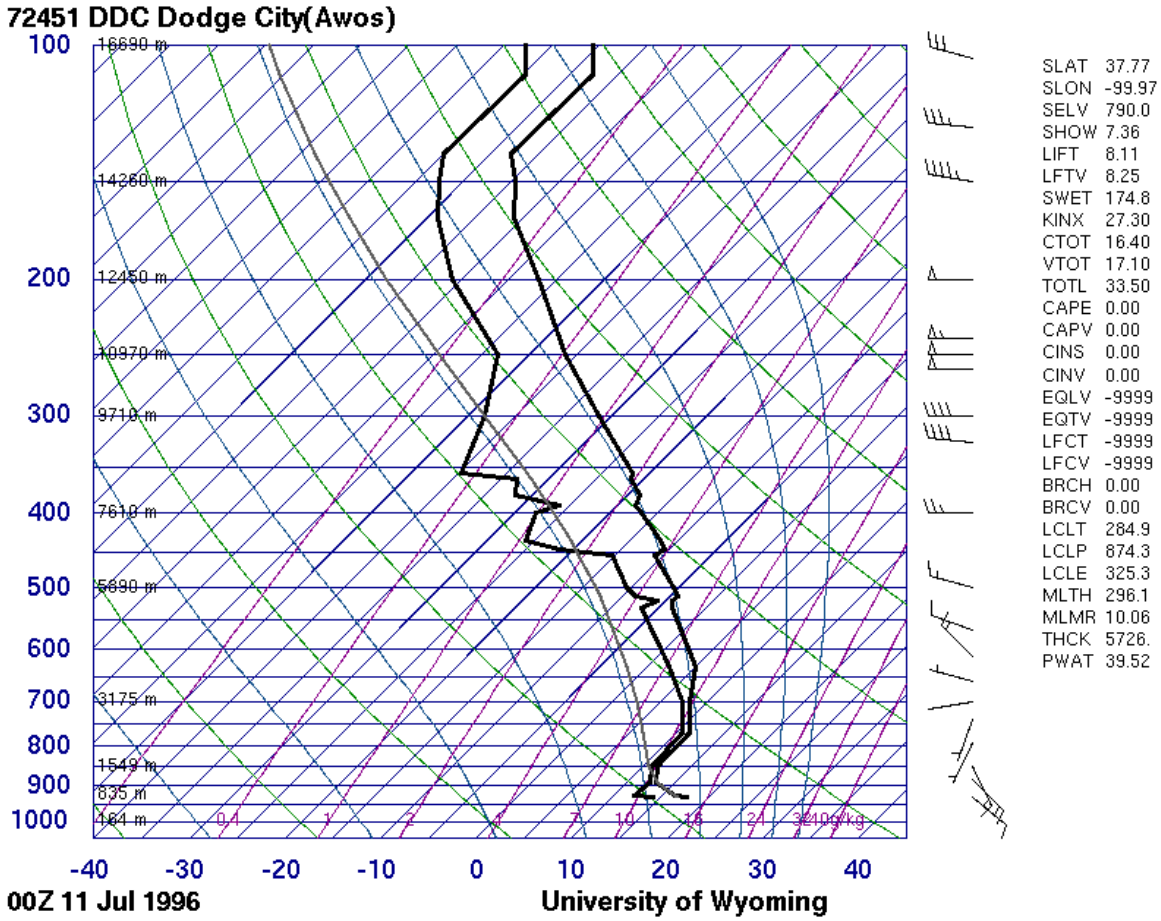

Figure 2.7: Atmospheric Sounding launched from Dodge City, Kansas (DDC) at 0000 UTC 11 July 1996 (Plot courtesy of the University of Wyoming [6])

Around 2200 UTC 10 July, convection began along the eastern edge of the Cheyenne Ridge as a result of elevated heating and upslope flow from the south. The multicellular formation was apparent on satellite imagery by 2300 UTC, with the strongest updrafts just east of the Wyoming-Nebraska border just after 0000 UTC on 11 July. The particular cell in this case study originated just outside Kimball, NE at this time and continued to strengthen and move eastward over the following two hours. Further details on this evolution can be found in Skamarock et al. (2000) and Dye et al. (2000).

[6] http://weather.uwyo.edu/upperair/sounding.html

2.3 Observational Data

2.3.1 SMART Radars

The Geary, OK case study was well documented by various observational data sets. In this study, a comparison between the various model runs and observations will be conducted to evaluate model configurations. Radar data was collected using two C-band Shared Mobile Atmospheric Research and Teaching (SMART) radars with a beam width of 1.5^o (Biggerstaff et al., 2005). The SMART radars collected very high resolution (in both space and time) reflectivity and velocity data for an intense observational period, completing sector volume scans approximately every 3 minutes over 120^o sectors. The radars were able to capture about three hours of the storm life cycle. The 90-minute period from 2350-0120 UTC described by Betten et al. (2018) which will be used in this study included the dissipating stage of one mesocyclone, the entire lifecycle of a second mesocyclone, and the organizing stage of a third mesocyclone. Earlier evolution is described in Calhoun et al. (2014). Elevation angles ranged from 0.5^o to 59^o, with increments of 0.3^o–3.0^o (Biggerstaff et al., 2005; Calhoun et al., 2014; Betten et al., 2018). The three-dimensional wind field was derived using Dual-Doppler analysis from the Custom Editing and Display of Reduced Information in Caresian Space (CEDRIC, Mohr et al. (1986)) by the National Center for Atmospheric Research (NCAR). Analysis was performed on a grid with 0.75 km horizontal spacing and 0.5 km vertical spacing at 22 analysis times as fully described in Betten et al. (2018).

2.3.2 Lightning Data

Oklahoma Lightning Mapping Array (OKLMA, Thomas et al. (2004); MacGorman et al. (2008)) data was also collected for the Geary, OK case study. The OKLMA is a three-dimensional lightning locating system used to map intracloud and cloud to ground lightning flashes. The OKLMA triangulates timings and locations of very high frequency (VHF) radiation pulses emitted by developing lightning channels by using the time of arrival of VHF peaks at the various stations in a cluster at 80 µs intervals with an accuracy of 40 ns. A central processor determines whether the times of arrival from multiple stations are grouped together closely enough to possibly be from a single source. If so, it computes the location and time of a source that minimizes the reduced chi-squared statistic.

For VHF sources to be considered valid for this analysis, they must be detected by at least six stations and have a reduced chi-squared value less than one, although other values are sometimes used by other studies. The updraft of the Geary supercell during the study period was within 71 km of the center of the OKLMA, corresponding to $\geq$88% flash detection efficiency and standard deviations in altitude solutions of $\leq$0.15 km at the time of the storm following Chmielewski et al. (2019).

VHF sources were then grouped into flashes with lmatools (Fuchs et al., 2016). For VHF sources to be considered a flash and not random environmental noise we required at least 10 VHF sources, the distance between adjacent sources must be within 3 km, and time between any two sources must be within 0.15 s. The maximum expected flash duration allowed by our study was 3 s. These criteria are consistent with values that have been used by other studies (e.g., Fuchs et al., 2016; Calhoun et al., 2013; Chmielewski et al., 2020). VHF sources have been subjectively assigned charge polarity (e.g., Calhoun et al., 2013; Coleman et al., 2003; Rust et al., 2005) following standard expectations of a bidirectional flash (Kasemir, 1960; Mazur and Ruhnke, 1993; Rison

et al., 2016) and physical differences in negative and positive breakdown processes. This analysis corresponds well to net charge regions and electric potential observed by in situ measurements and can be overlaid on radar-observed storm structure to get insight on the charge structure and evolution of the storm (e.g., Lang et al., 2004; Rust et al., 2005; MacGorman et al., 2005; Wiens et al., 2005; Maggio et al., 2009; Chmielewski et al., 2020)

Chapter 3

Geary, OK Case Study

3.1 Dynamic Structure

A few dynamic differences stood out between the five CCN concentrations in the Geary, OK storm. These differences were compared using both the two-moment (2M) and three-moment (3M) microphysics options described in Chapter 2 to test for overall sensitivity. The electrification has no feedback to microphysics or the dynamic structure, so only the SP98 scheme will be discussed in this section. We will refer to the 3M SP98 simulations as the control set.

Geary, OK Supercell Evolution					
	100 CCN	300 CCN	500 CCN	1000 CCN	2000 CCN
Initial Precipitation	10 minutes	12 minutes	12 minutes	14 minutes	15 minutes
Storm Split	40 minutes	42 minutes	44 minutes	50 minutes	52 minutes
Initial Flash	24 minutes	24 minutes	26 minutes	24 minutes	24 minutes

Table 3.1: Table of important times in the evolution of Geary, OK simulations (control set of simulations)

The initial onset of precipitation (e.g., reflectivity > 0) was delayed with high CCN concentrations (Table 3.1). In the control simulations, the 100 CCN cm^{-3} simulation shows precipitation aloft starting around Time (T)=10 minutes into the simulation, at T=12 minutes for 300 and 500 CCN $^{-3}$, T=14 minutes for 1000 CCN cm^{-3}, and T= 15 minutes for 2000 CCN (Table 3.1). Although slight differences in timing were noted between the 2M and the control simulations, the overall pattern of delayed precipitation at high CCN concentrations remained the same (Fig. 3.2). This pattern agrees with the findings of Twomey (1977); Albrecht (1989) and Gunn and Phillips (1957), where increased CCN was found to suppress the initial onset of precipitation via weakened collision and coalescence processes. Along with the initial delay in precipitation, the altitude at which this initial precipitation was occurring is also different among the different CCN concentrations. At higher CCN concentrations, the altitude of the initial precipitation was also higher (Fig. 3.1). This pattern was also evident in the 2M simulations (Fig. 3.2).

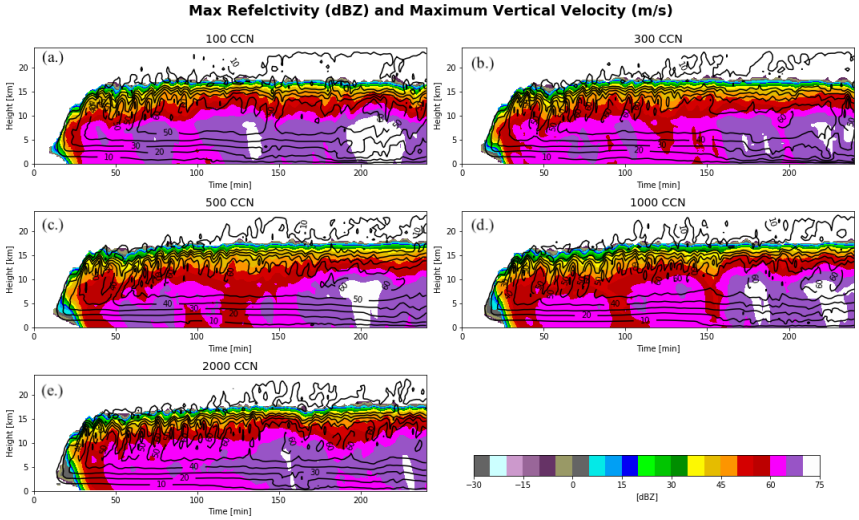

Figure 3.1: Time-height plot of maximum (Reflectivity (color fill; dBZ) and maximum vertical velocity (black contours; m/s) for Geary, OK case simulations (control simulations) just for the right-moving cell

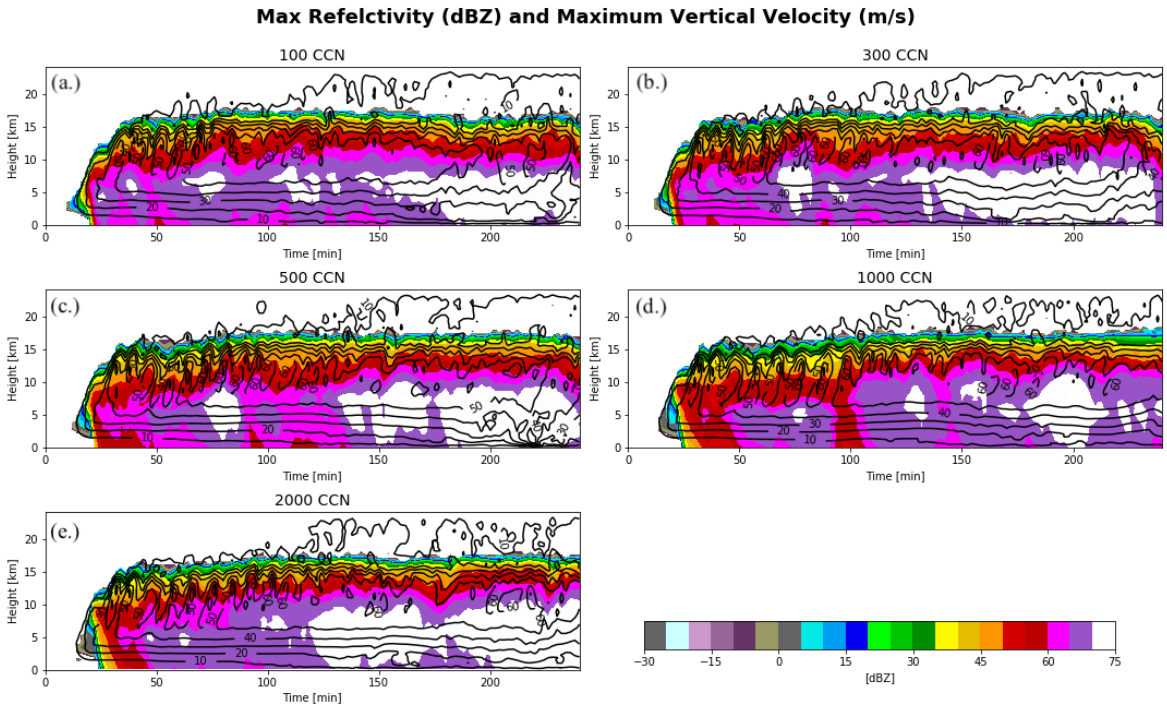

Figure 3.2: Same as Fig. 3.1, but for 2M set of simulations

Lasher-Trapp et al. (2018) found when increasing the CCN in simulations, warm rain processes were slowed and the graupel mass contributing to surface rainfall decreased, which is similar to what is occurring in this case (Fig. 3.3 & 3.4).Hydrometeor concentration and mass were both analyzed. While hydrometeor concentration describes the total amount of each particle type, hydrometeor mass gives insight on the warm and cold rain processes occuring resulting in certain hydrometeor types to grow more or faster then others. The simulations with higher CCN had more mixed-phase hydrometeor processes, with these cold rain processes occurring at higher altitudes for majority of the simulation (Fig. 3.5) as evidenced by the presence of frozen hydrometeors. Rain concentrations were found also occured at higher altitudes for higher CCN concentrations, which suggests that warm rain processes were displaced to higher altitudes. As expected, these rain concentrations consistently occurred at altitudes lower

than, and presumably at temperatures warmer than, the cold rain processes. Jouan and Milbrandt (2019) noted, in their simulations of a squall line, the importance of graupel in rain production and the sensitivity of graupel growth rates on changes to droplet concentrations. They found graupel concentration decreased and hail concentrations increased with increasing CCN, similar to the patterns we are seeing in this case study (Fig. 3.3 & 3.4).

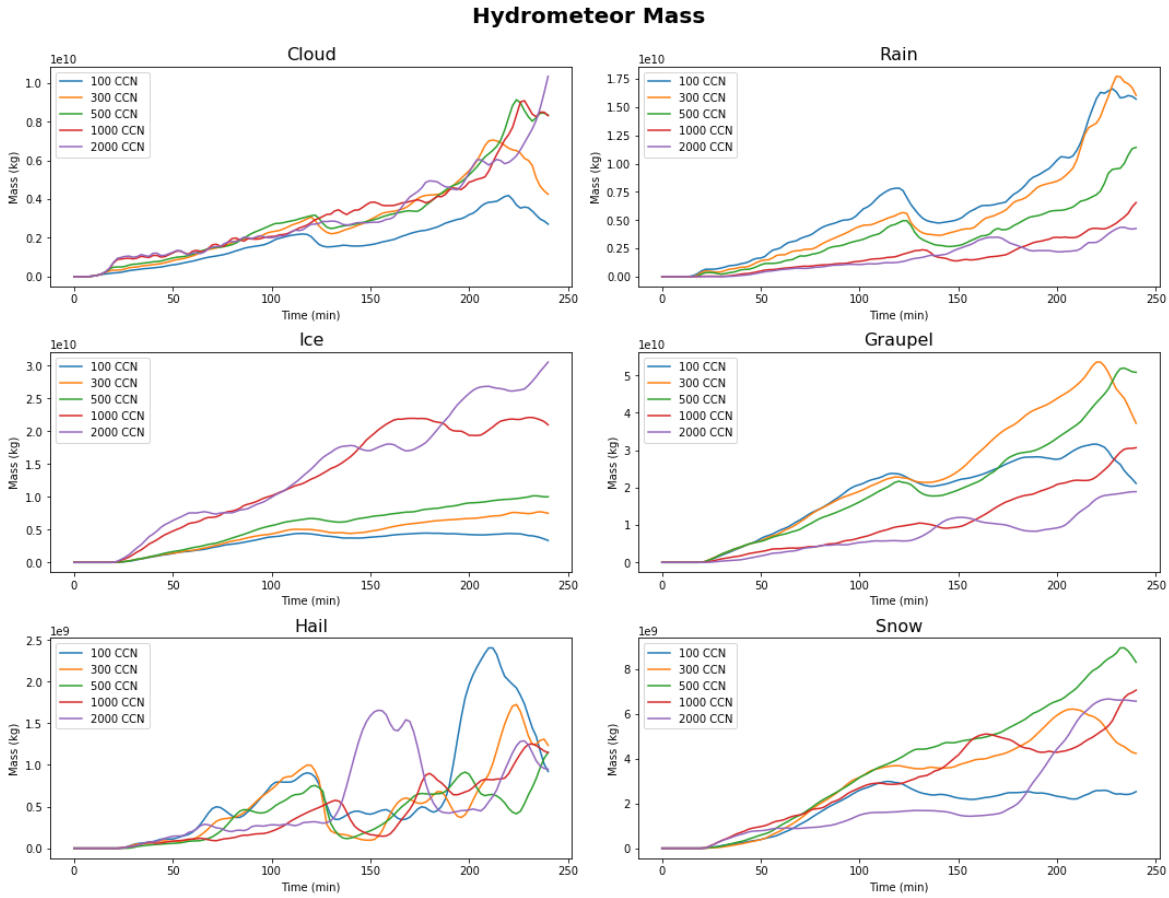

Figure 3.3: Integrated hydrometeor mass (kg) with time for the Geary, OK case over entire domain (control simulations)

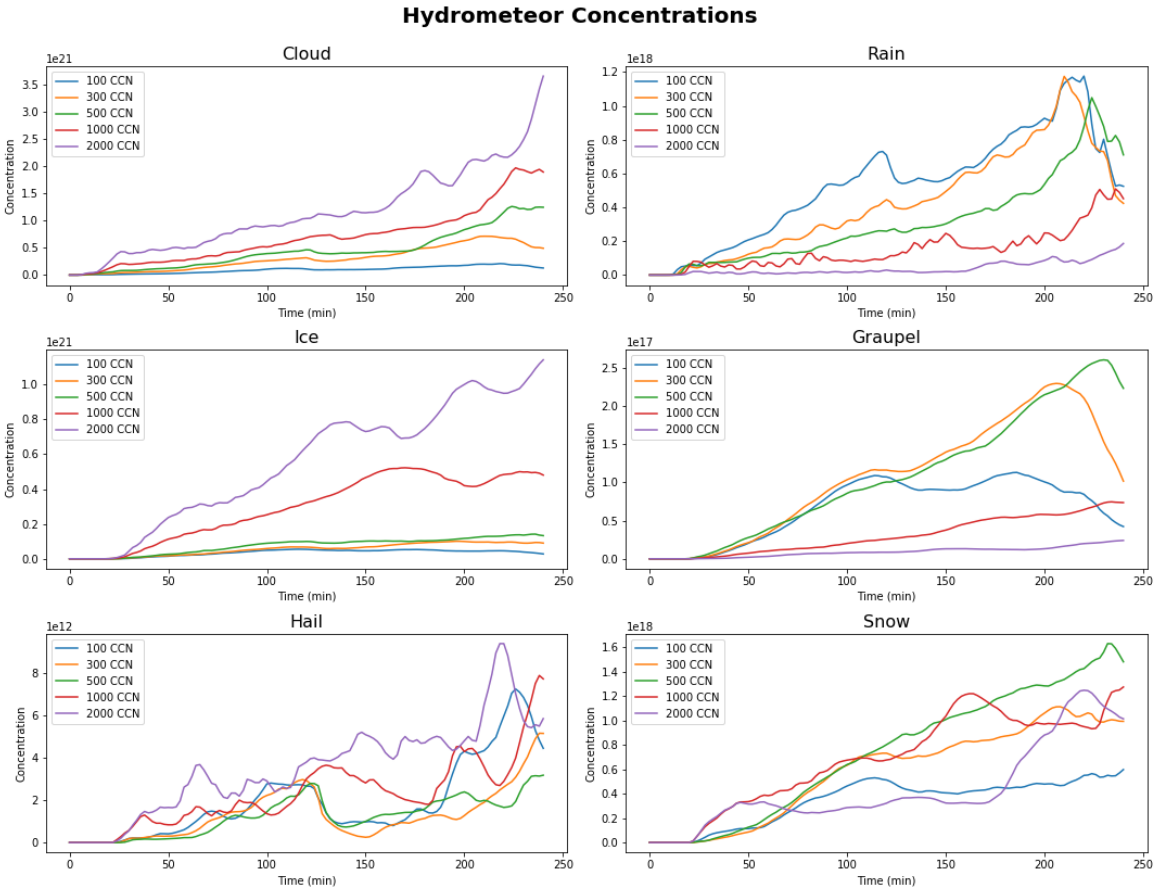

Figure 3.4: Integrated hydrometeor concentrations (count) with time for the Geary, OK case over entire domain (control simulations)

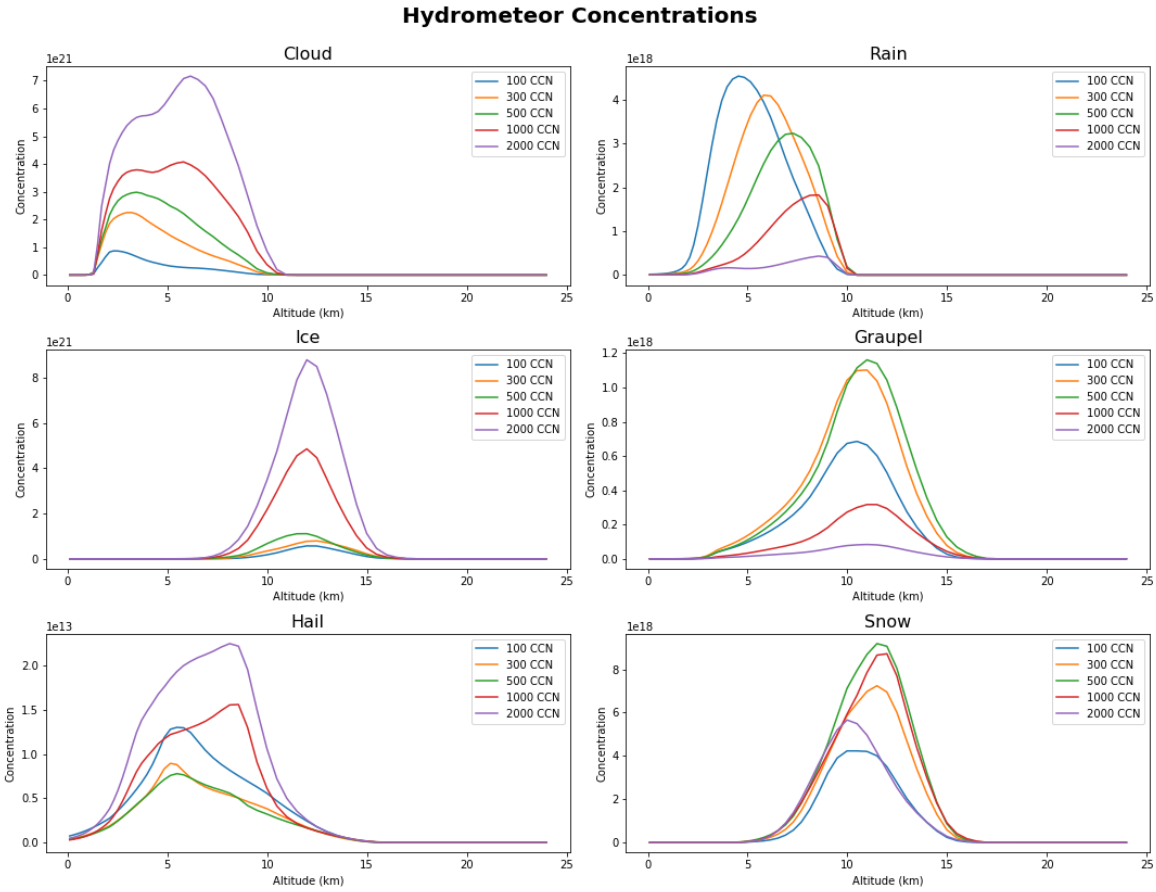

Figure 3.5: Integrated hydrometeor concentrations (count) with height for the Geary, OK case over entire domain (control simulations)

Other differences in evolution were also noted. A storm split occurred early in the simulation, and like the initial onset of precipitation, this split was further delayed at higher CCN (Fig. 3.6). For the 100 CCN cm^{-3} case, the storm split occurred at T=40 minutes, at T=42 minutes for 300 CCN cm^{-3} , T=44 minutes for 500 CCN cm^{-3} , T=50 minutes for 1000 CCN cm^{-3} , and T= 52 minutes for 2000 CCN cm^{-3} (Table 3.1). This is roughly a 12-minute delay between the lowest and highest concentrations. This delay is likely a result of the hindered warm rain processes previously explained (Fig. 3.3). As the storm continued to evolve, differences in the horizontal spatial extent

of the storm appeared. The storm became more spatially compacted at higher CCN concentrations, with differences in the size of the left-mover displaying this quite well. In the 2000 CCN cm^{-3} case, the left-mover was significantly smaller and shorter lived then in the lower CCN simulations. This will be further examined later in this section.

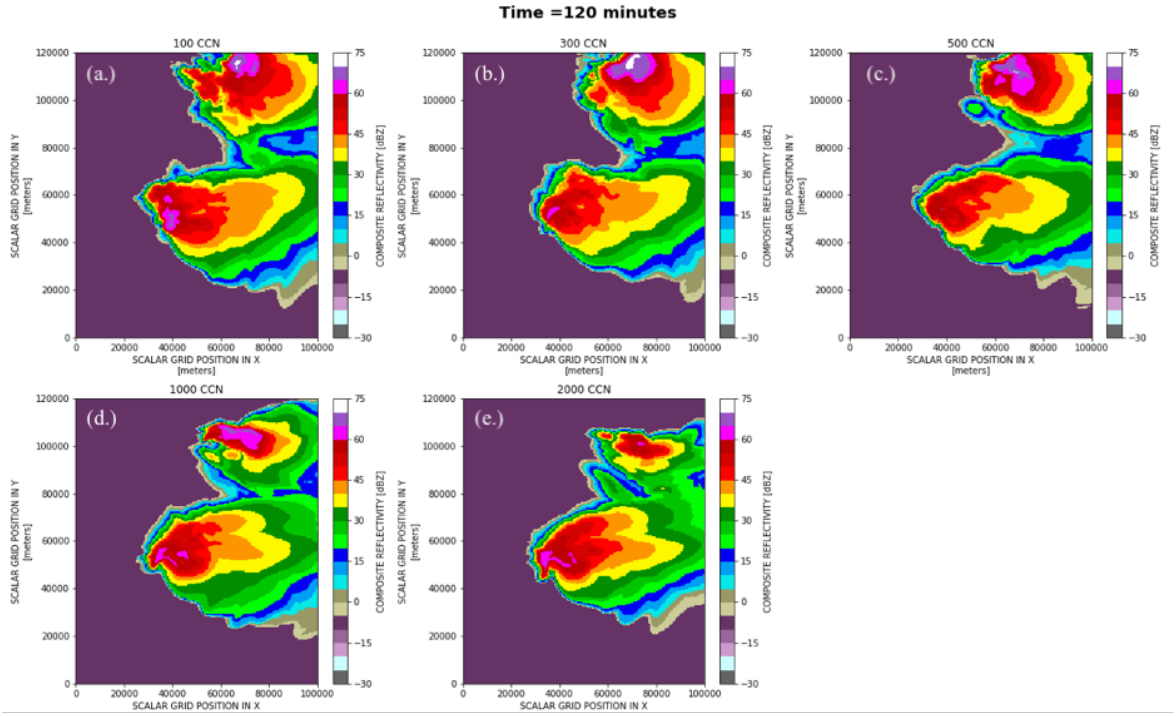

Figure 3.6: Aerial view of composite reflectivity (dBZ) of the Geary, OK storm (control simulations) at time T=120 minutes

The intensity of the storm can be analyzed using updraft volume and speed (Fig. 3.7). From reflectivity alone, it is hard to compare intensities as the storm appears to be cycling at different time intervals across the five concentrations (as seen in Fig. 3.1). Maximum vertical velocity may also be a poor indicator of updraft strength for this case study, as the maximum vertical velocity is rather consistent across all five concentrations (Fig. 3.7c). This similarity suggests that a strong supercell will still be a

strong supercell despite the CCN concentration. Differences between the CCN concentration simulations arise when observing the amount of volume the updraft occupies, with a larger updraft volume signaling a stronger storm. Updraft volume at both >5 and >10 m s^{-1} were generally larger in the simulations with lower concentrations (Fig. 3.7a,b). This first becomes evident right around the time of the storm split where the three lowest concentrations have a distinctly larger volume than the two highest CCN concentration simulations. Between the storm split and up until around T=150 minutes, the updraft volume remains consistent between the five concentrations. At this point only the right mover remains in the full model domain (previously described in chapter 2) and any vertical motion from the left-moving cell is not included in this calculation. In the last 90 minutes of the simulation (T=150 onwards), differences in the updraft volume begin to arise again where the three lowest CCN concentrations have the largest updraft volume, with 300 CCN cm^{-3} having the overall largest volume. In the last 20 minutes of the simulation, contamination from secondary convection complicates the calculations of updraft volume.

Although a perfectly linear pattern is not observed in our study, these results suggest that an increase in CCN concentration results in smaller updraft volumes in an HP supercell. This contradicts the findings by Mansell and Ziegler (2013); however the simulated storm in that study was a low-shear ordinary thunderstorm with a shorter lifetime. Differences in our simulation took much longer to appear than in the study by Mansell and Ziegler (2013). Fan et al. (2009) found suppression of convective strength by aerosols in cases where strong windshear is present; however under weak wind shear, the opposite was found. The suppression of convection by aerosol loading was found to result from higher evaporation and sublimation rates in the updraft region resulting in significantly lower net latent heat release at increased CCN in strong windshear environments (Fan et al., 2009).

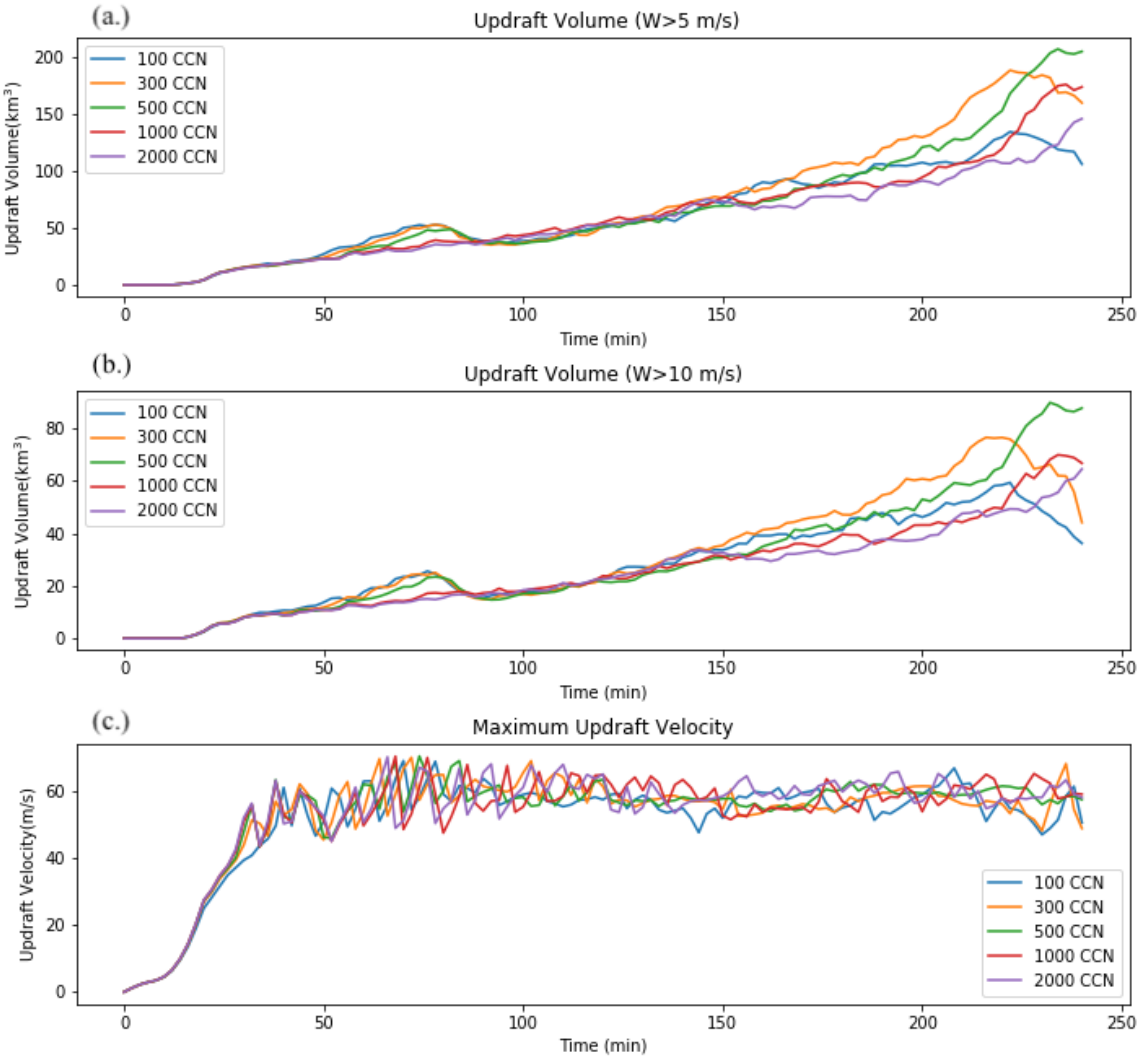

Figure 3.7: a.) Plot of updraft volume for all grid points with vertical motion (w) greater than 5 m s^{-1} with time for Geary, OK case study (control simulations). b.) Same as in a. but for updrafts greater than 10 m s^{-1}. c.) Maximum vertical velocity with time

Cold pool formation provides good insight into the observed storm evolution. The baroclinicity between the cold pool and surrounding environment promotes lift and

encourages secondary convection. The stronger the potential temperature difference along the edge of the cold pool, the stronger the lift associated with it. At higher CCN concentrations, the depth (potential temperature perturbation) and spatial extent were smaller (Fig. 3.8). At T=120 minutes (same as in Fig. 3.6), the cold pool deficit at 100 CCN cm^{-3} reached 7 ^{o}C, while the 2000 CCN cm^{-3} case only had a deficit of 1 ^{o}C. By the end of the simulation (T=240 minutes; not shown), the cold pool produced potential temperature deficits of up 15 ^{o}C in the 100 CCN cm^{-3} simulation. In the 2000 CCN cm^{-3} simulation, the potential temperature difference along the cold pool only reached 5 ^{o}C by the end of the simulation.

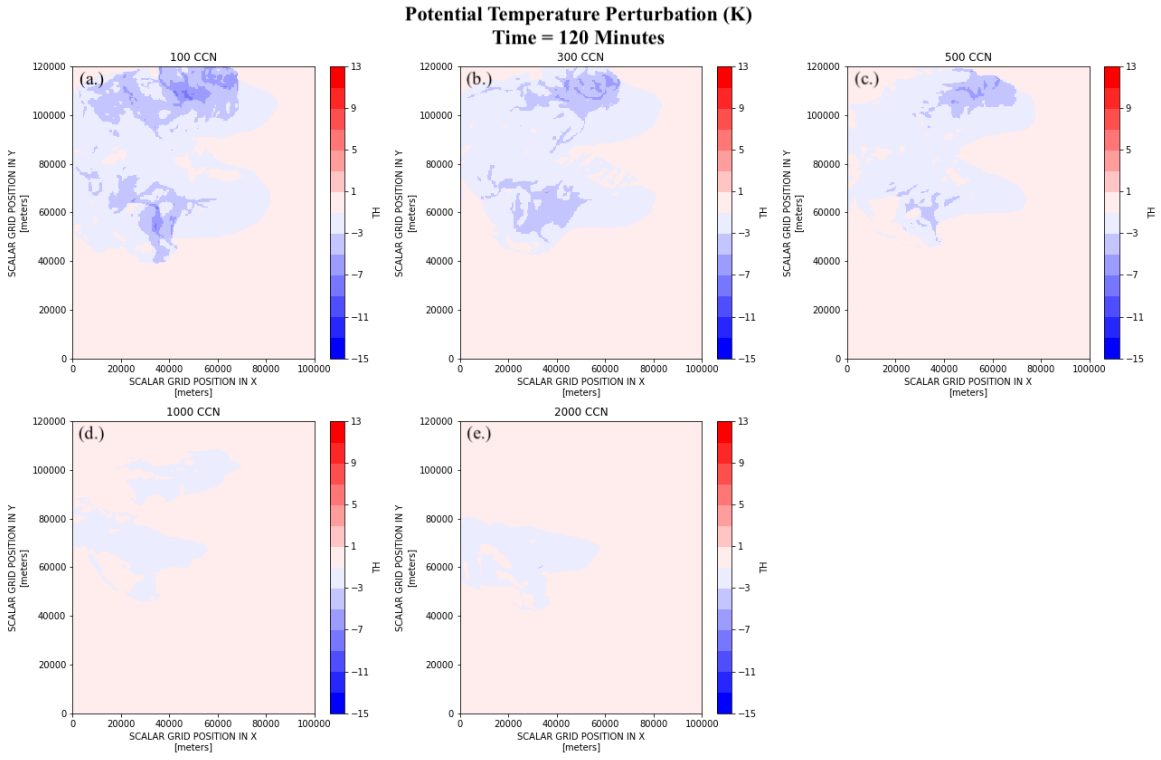

Figure 3.8: Surface potential temperature perturbation (K) at T=120 minutes for Geary, OK case (control simulations) for 5 CCN concentrations

Storer et al. (2010); Lerach and Cotton (2012), and Khain et al. (2011) found a similar pattern; where more polluted simulations had warmer cold pools. The difference in rainfall amounts (Fig. 3.9) and size of the hydrometeors between the different CCN concentrations influences evaporative cooling near the surface. The higher CCN cases, where we have seen less liquid precipitation and more cloud ice, also produced smaller and warmer cold pools as a result of reduced evaporative processes at the surface. The supercell simulations of Storer et al. (2010) also included a storm split, and in changing the CCN concentration they found a large difference in secondary convection triggered by the cold pool of the left-moving storm. In their study, the low CCN case had colder cold pools and produced more secondary convection, similar to our model results. This sets up a positive feedback loop, as smaller and weaker cold pools provide less forcing for secondary convection, a reduction in convective coverage and intensity, and ultimately less precipitation and so on.

At T=120 minutes the weaker cold pools (Fig. 3.8) correspond to the weaker updraft volumes (Fig. 3.7a,b) and smaller storms (Fig. 3.6). At this time, the 2000 CCN cm^{-3} case had no cold pool formation in the vicinity of the left mover, which had reflectivities (Fig. 3.6e) that were significantly weaker than the other four concentrations. The timing of cold pool formation (not shown) was also found to be delayed at higher CCN concentrations, resulting from the delay in initial formation and growth of precipitation.

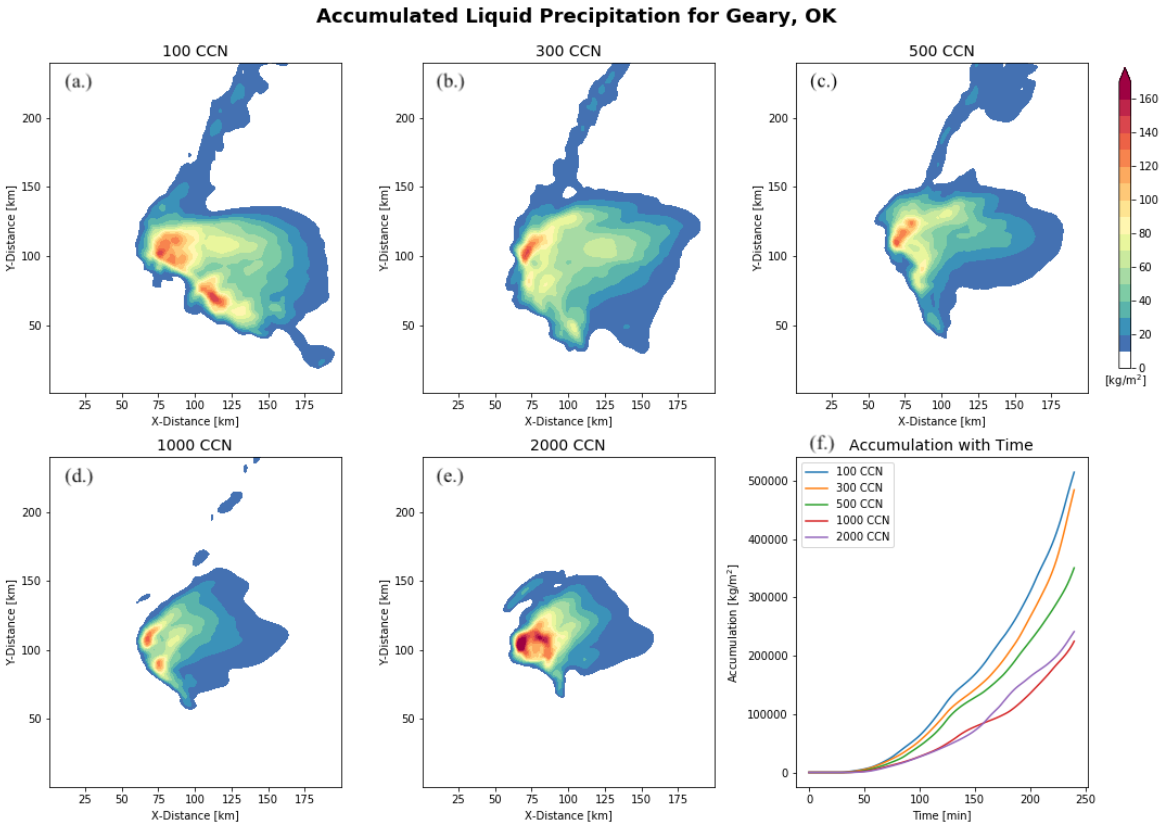

Figure 3.9: Total surface accumulated liquid precipitaion (kg m^{-2}) for Geary, OK (control simulations) for 5 CCN concentrations. Accumulations are over the entire domain and model run time

3.2 Electric Structure

The electric structure was investigated by altering the NI charging schemes or the microphysics schemes. To obtain an overview of the average charge structure of the storm throughout its lifetime, average charge density, electric potential, and flash rates with height were analyzed over the entirety of the simulation for each of the five CCN concentrations. Average flash area will also be analyzed in this section. These averages

were taken over each model level and only for the right-moving storm. We note that this average approach only shows the total charge imbalance by height and time.

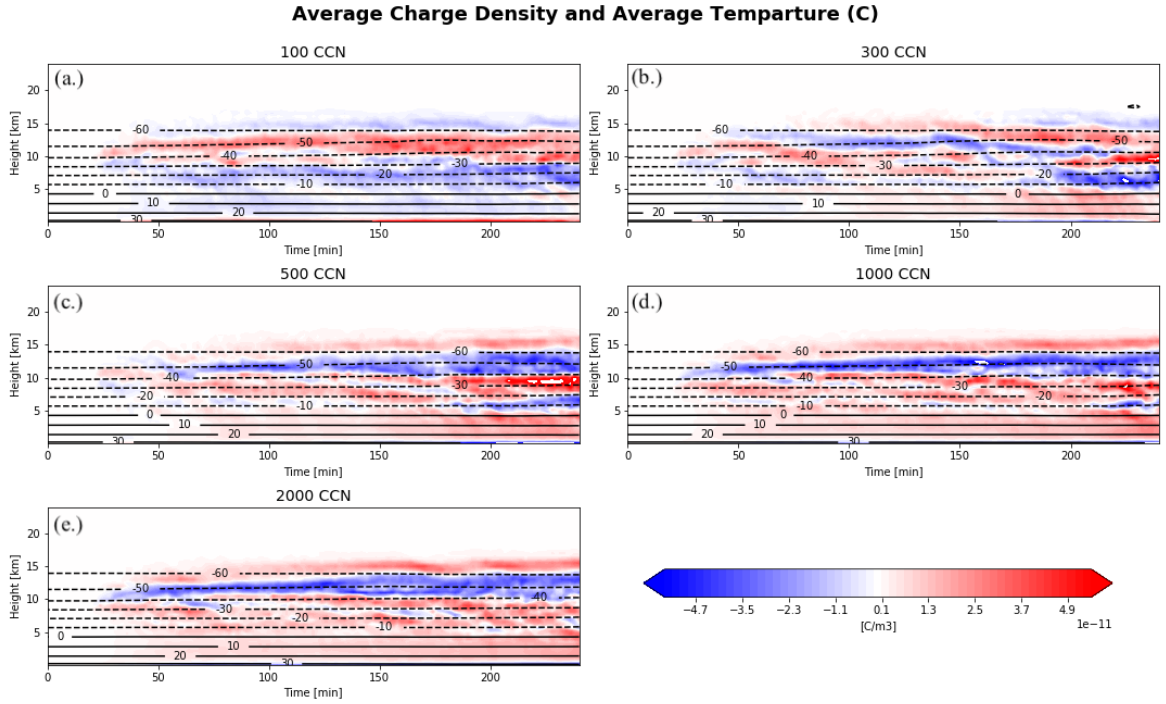

Figure 3.10: Time-height plot of average charge density of the right-mover (fill), average domain temperature (black contours; ^{o}C) for Geary, OK (control simulations)

First, we will analyze the results of our control simulations (3M SP98 NI scheme, Fig. 3.10). The 100 CCN cm^{-3} simulation had a normal (positive) dipole with a negative charge region from the surface to around 5 km, a positive charge region between 5 and 14km, and an upper negative screening layer extending from 14 km to 16 km. The 300 CCN cm^{-3} simulation initially produced a normal (positive) dipole with a similar structure as the 100 CCN simulation for the first 90 minutes of the simulation, but later displayed a more complex structure. Around 90 minutes into the simulation it produced a net charge structure with five vertically stacked layers: a positive charge region dominated from the surface to 5 km, with a shallow layer of negative charge

above, followed by region of positive charge between 7 and 12 km, followed by a weak negative region between 12 km and 15 km, and topped off by a shallow positive layer. As the simulation progresses, the polarity and charge structure of the storm alternated between normal and inverted polarity, with additional charge layers developing with time. The 500, 1000, and 2000 CCN cm^{-3} simulations had similar charge structures to each other. For majority of the simulation, these three simulations exhibited an inverted dipole structure on average, with positive charge regions from the surface to roughly 10 km, a negative region between 10 and 14 km with a pronounced positive screening layer 14 km to 17 km. As the storm evolved the negative charge layer expands from a depth of roughly 2 km to 5 km in all three cases. Starting around T=200 minutes, a lower negative layer suggestive of an inverted tripole structure began to build around 5 and 6 km and lasts through the end of the simulation for the 500 and 1000 CCN cm^{-3} cases, with the 2000 CCN cm^{-3} case showing this negative layer weakly appeared in the last few minutes of the simulation.

Along with differences in the location of these charge layers, the magnitude of charge within these layers also changes, with the magnitude of average charge being higher at higher CCN concentrations. This could be due to overall higher charge densities or to a more uniform vertical distribution of net charge in the storm. The 2M test produced charge layers at the same altitudes as the control simulations for each of the 5 concentrations, but with slightly weaker magnitudes (Fig. 3.11). The pattern of higher charge magnitudes associated with higher CCN concentrations also occurs. Sun et al. (2021) and Zhao et al. (2015) found similar results in which charge density was stronger in polluted air than in clean air as a result of more ice particles participating in the electrification process. By its nature, electric potential gives a smoother outline of these charge layers and provides insight as to where lightning would propagate (Fig. 3.12). The evolution of electric potential is very similar to that of the charge density,

with 100 CCN cm^{-3} case producing a normal dipole structure and having opposite polarity to that of the higher CCN cases, and the 300 CCN cm^{-3} case demonstrating an alternation between normal and inverted polarity.

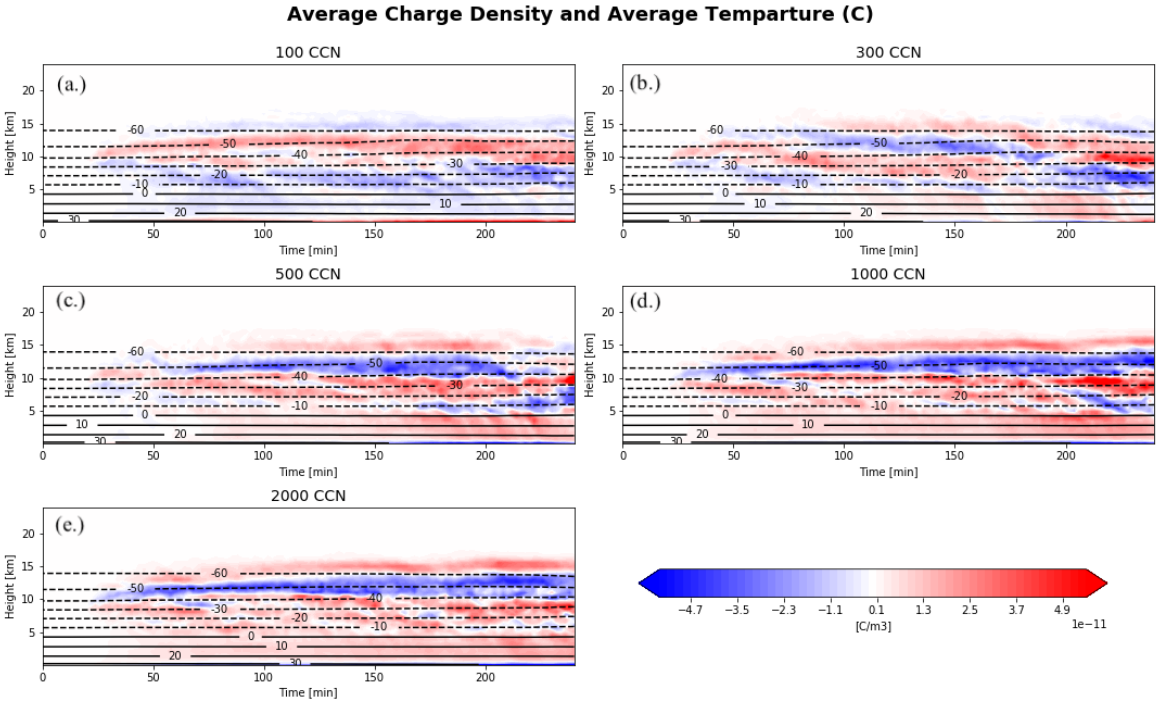

Figure 3.11: Same as in Fig. 3.10, but for 2M set of simulations

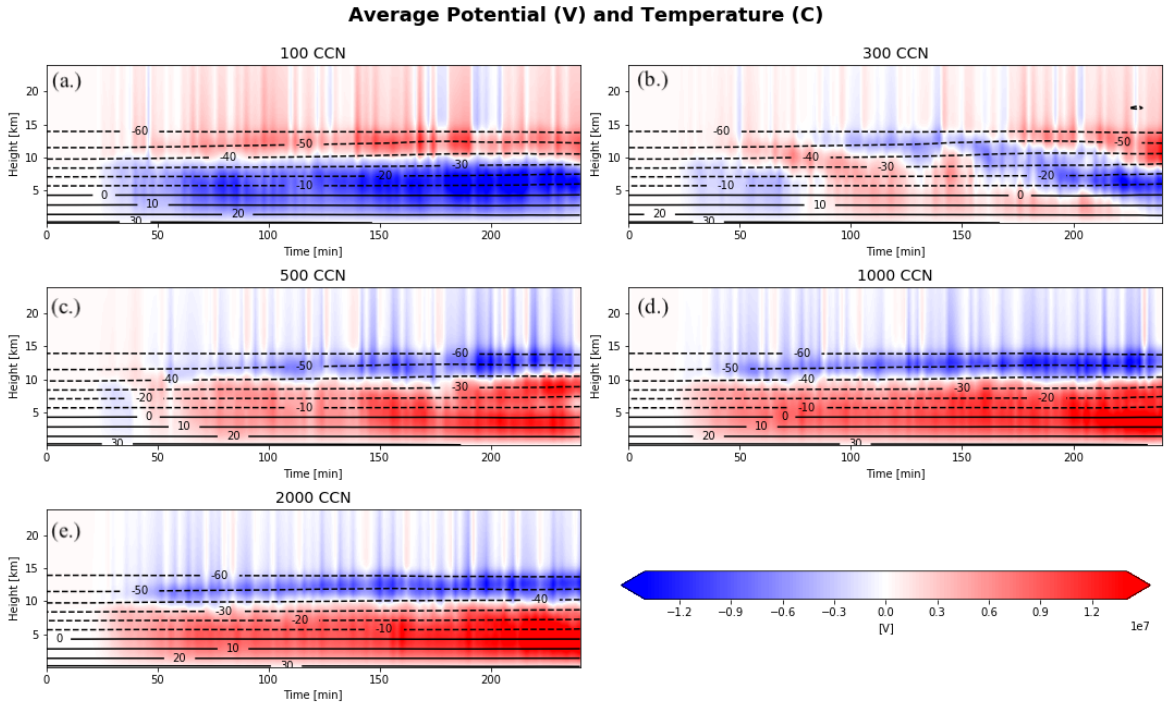

Figure 3.12: Time-height plot of average electric potential (V) of the right-mover (fill) and average domain temperature (black contours; ^{o}C) for Geary, OK (control simulations)

The flash rates associated with the Geary, OK storm were relatively high in the simulations, as shown by the time series of total rates (Fig. 3.13a) and flash initiations point densities (Fig.3.14). At higher CCN concentrations flash rates were higher (Fig. 3.13a). Flash rates in the 100 CCN cm^{-3} case were around 15-30 flashes per minute through the entirety of the simulation, for 300 and 500 CCN cm^{-3} cases the flash rates started around 15-30 per minute and reached around 50 flashes per minute by the end of the simulation. In the 1000 CCN cm^{-3} case, flash rates started at 30 to 50 flashes per minute and averaged around 100 flashes per minute by the end of the simulation. In the 2000 CCN cm^{-3} case flash rates were around 50 flashes per minute for majority of the period and reached over 150 flashes per minute in the last

60 minutes. These results are similar to many other studies (e.g., Mansell and Ziegler, 2013; Altaratz et al., 2010; Pawar et al., 2017; Ren et al., 2018; Kochtubajda et al., 2011), in which higher lightning rates were produced at higher aerosol concentrations below a threshold concentration; however in our simulations of this case we see a somewhat more monotonic relationship throughout majority of the simulation time. In all five simulations, flash rates increased significantly in the last twenty minutes as secondary convection began. As mentioned in the dynamics section, secondary convection was significant in the last twenty minutes of the simulation. This secondary convection results in closely spaced updrafts and downdrafts, increased turbulence, increased interactions between particles and an increase in the occurrence of flashes. This increase in flash rates may also be a product of having higher charge separation rates, where the electric field builds up quickly before charge can advect very far.

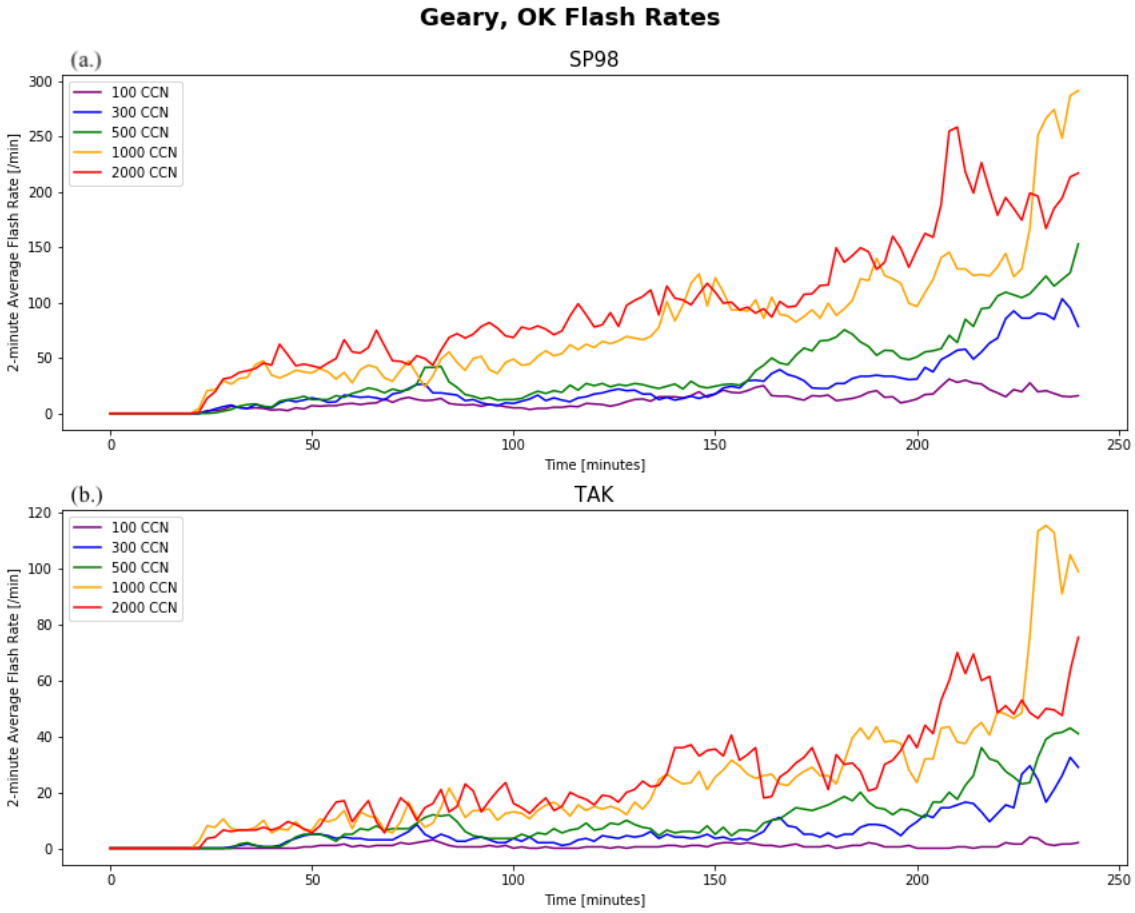

Figure 3.13: a.) Time series of average 1-minute flash rates per 2-minute period for Geary, OK (control set) b.) Same as (a.) but for TAK NI scheme

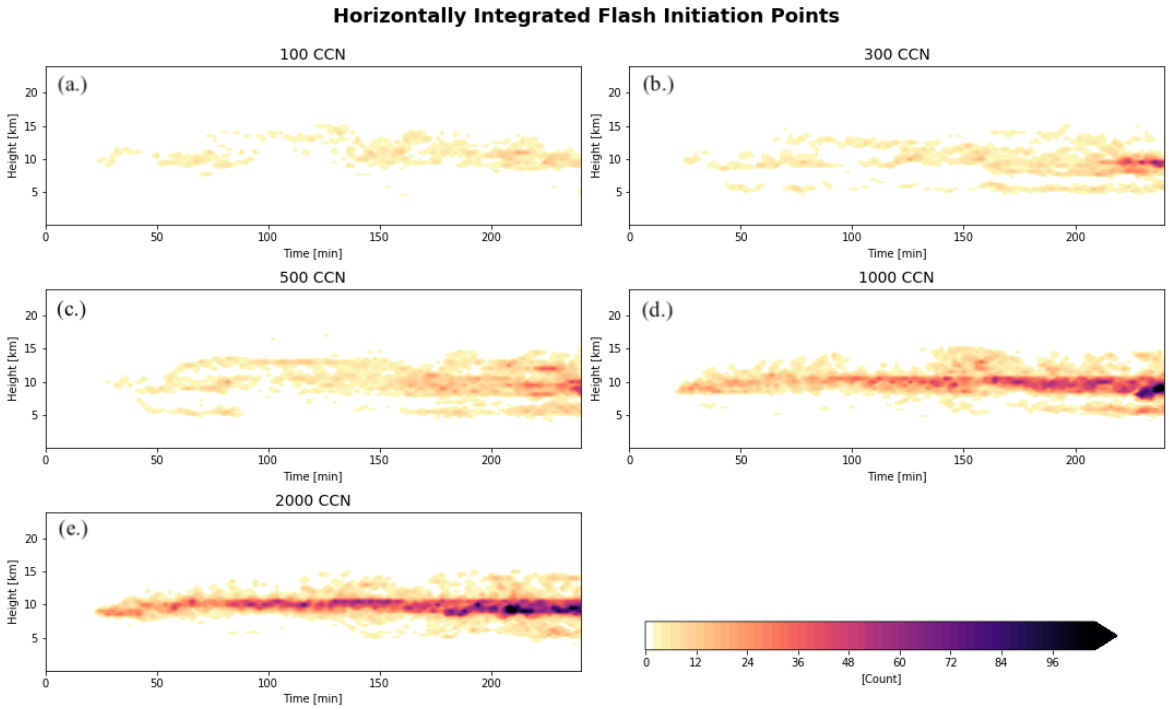

Figure 3.14: Time-height plot of horizontally integrated flash initiation points for Geary, OK (control simulations). Total flash initiation points at one time is the same as the flash rate.

The altitude of these initiations differed amongst the 5 simulations (Fig.3.14 & 3.15). These flash initiation points at low CCN concentrations were spread out over various altitudes, with flash initiations disbursed between 8 and 15 km for the 100 CCN cm^{-3} case. In the 300 CCN cm^{-3} case, three distinct layers of initiations points become evident at 5 km, 10 km, and 12 km. These layers are still evident in the 1000 and 2000 CCN cm^{-3} simulations; however the highest flash rates are occurring in the middle layer around 10 km. At higher CCN concentrations these flash initiations appear to be more concentrated at a singular altitude. Initial flashes began around 25 minutes into the simulation in each of the 5 concentrations (Table 3.1), and no delay was observed

like in Sun et al. (2021). The 2M scheme produced a very similar pattern in terms of timing, location, and flash rate of these initiation points (not shown).

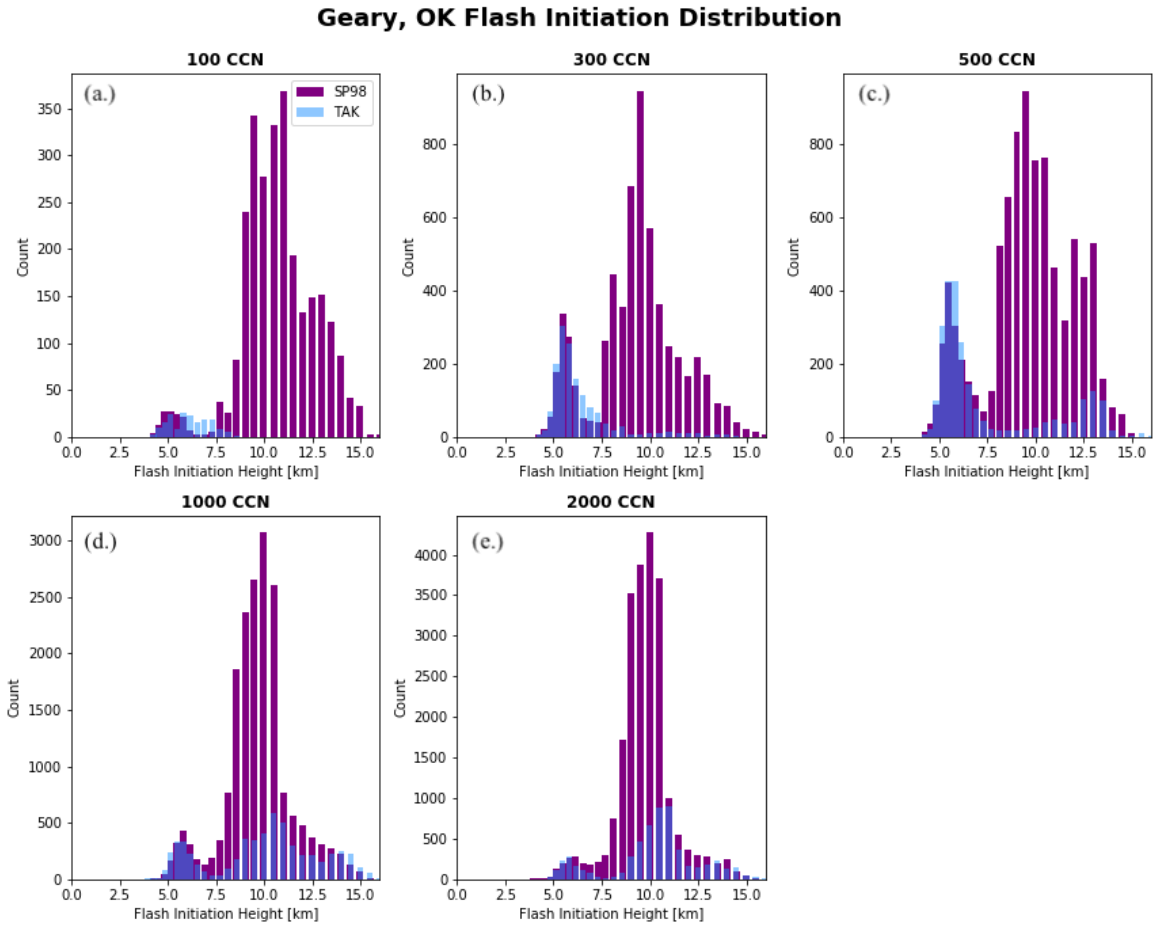

Figure 3.15: Distributions of flash count with altitude for all five CCN concentrations. Simulations using SP98 in purple, simulations using TAK NI scheme in blue.

This analysis was also conducted using the TAK NI scheme. There is uncertainty about which charging scheme best represents the environmental NI charging and this is further complicated by model predictions of variables like rime accretion rate or effective water content. Compared to SP98, the Takahashi scheme is not as sensitive to impact speed and is more likely to produce normal tripole charge structures. In

the 3M TAK set of simulations, the net charge density layers are quite different and stronger in magnitude than those produced with SP98 (Fig. 3.16). This could be a result of more uniform charge layers or higher charge densities. In the 100 CCN cm^{-3} simulation, a "bottom-heavy" normal tripole structure is observed with positive charge regions between the surface and 6 km, a negative region between 6 and 12 km, and a weak positive layer from 12 and 15 km. This is opposite polarity to the polarity that was seen in most of the SP98 simulation. Instead of seeing different polarities in the higher concentrations, additional negative charge layers are seen above 15 km and near the surface. At higher CCN concentrations, the lower positive layer was weaker and shallower as a negative charge region appeared to build near the surface. This layer is dominated by surface corona discharge in response to the electric field. It is hypothesized that the development of the lower positive charge is delayed by at higher CCN by the delayed appearance of graupel in the 0 to -15^{o}C layer within the updraft. The lower positive charge layer is very weak and almost completely non-existent in the 2000 CCN cm^{-3} case, which was noted in Mansell and Ziegler (2013) as the point at which Hallett-Mossop ice splintering becomes less effective because there are fewer large droplets. Electric potential again showed a similar pattern to the charge density (Fig. 3.17); however now an inverted dipole structure is seen instead of a normal tripole structure in the 100 CCN cm^{-3} case. Electric potential shows the higher CCN concentrations having opposite polarity to the 100 CCN case. These results line up more with the results of Zhao et al. (2015) and Mitzeva et al. (2006) who found that in polluted cases aerosol loading leads to increased cloud water content, resulting in a more negative charging and a new negative charge region developing above the main positive charge center. Zhao et al. (2015) used the same adjusted SP98 NI scheme as used in this study (refer to Chapter 2), while Mitzeva et al. (2006) used an NI charging scheme based on the laboratory data of Brooks et al. (1997).

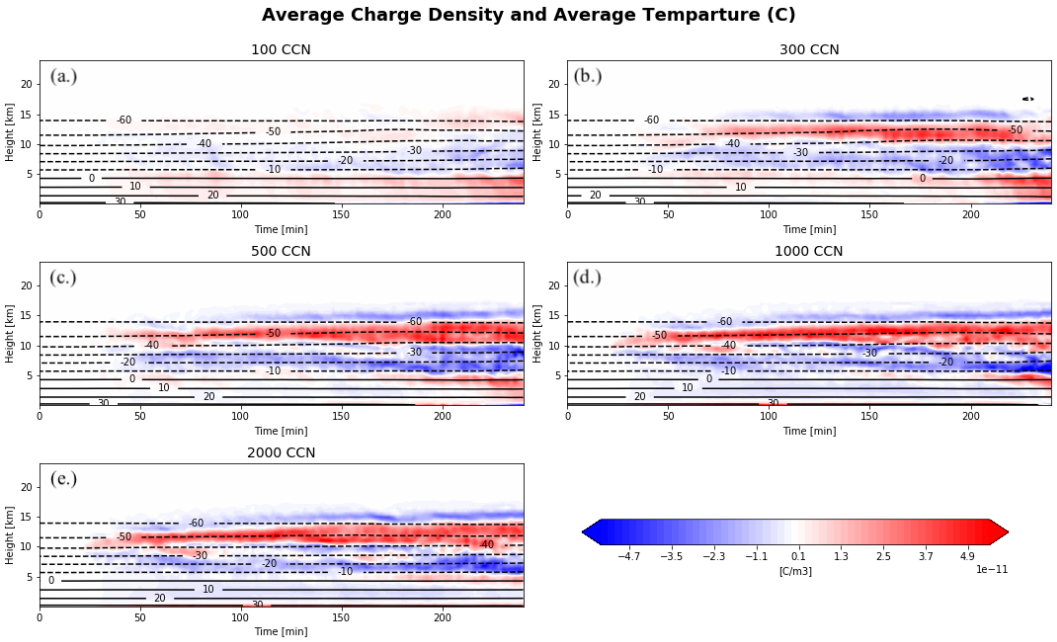

Figure 3.16: Same as in Fig.3.10, but for TAK set of simulations

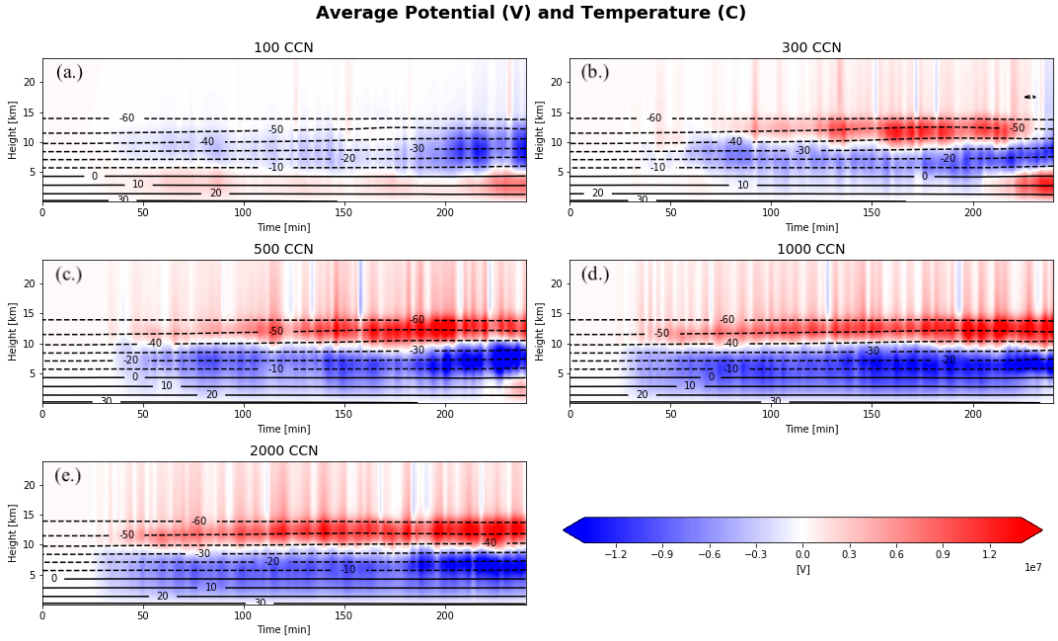

Figure 3.17: Same as in Fig. 3.12, but for TAK set of simulations

The flash rates using the TAK NI scheme were significantly lower than when using the SP98 scheme (Fig. 3.13b & 3.18). Flash rates were less than 5 flashes per minute in the 100 CCN cm^{-3} simulation, around 15 flashes per minute for 300 CCN cm^{-3}, around 20 flashes per minute for 500 CCN cm^{-3}, and up to 40 flashes per minute for 1000 and 2000 CCN cm^{-3}. Although the magnitude of flash rate differed from those of the SP98 set, the pattern of higher flash rates at higher CCN was maintained with this scheme. The three distinct layers of flash initiations are still produced with the TAK scheme, with the middle layer at 10 km producing higher flash rates than the other layers with higher CCN (Fig. 3.15).

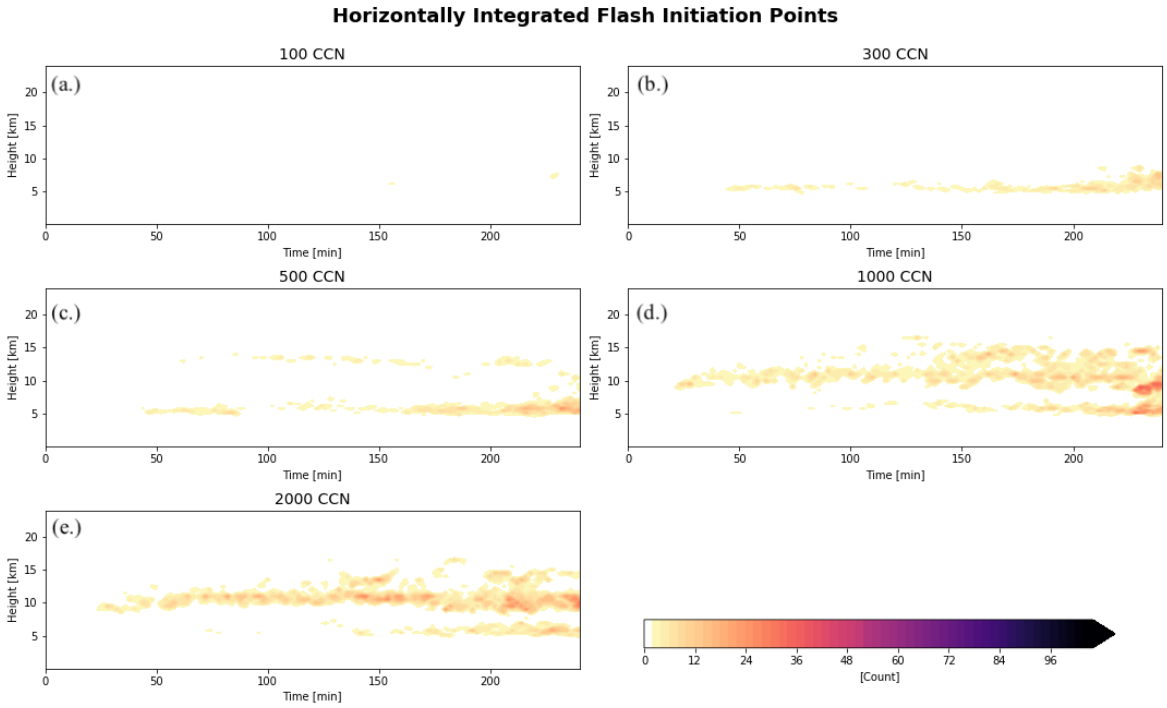

Figure 3.18: Same as in Fig. 3.14, but for TAK set of simulations

With the average charge density layers being larger in magnitude with the TAK NI charging scheme than with the SP98 scheme, one might have expected that the flash rates would have also been higher. By looking at a cross-section of the storm at a single

time (Fig. 3.19 & 3.20) more information about the charge structure can be obtained than from the domain average. At time T=200 minutes, after the left mover exited the domain, the net charge structure was more complicated than what is seen in the time-height average. These cross sections also illustrate sloping charge layers outside the updraft region and toward the forward flank and anvil. The stronger upward velocities lift charge layers to higher altitudes in the updraft column, from which the charged particles advect horizontally and fall to lower altitudes. The SP98 NI charge scheme produces many small pockets of adjacent positive and negative charge, especially above the updraft core. With the horizontal averaging these small pockets of charge get averaged and cancelled out resulting in weaker magnitudes. The TAK NI scheme has more continuous charge layers in comparison, which when averaged horizontally result in higher charge density magnitudes.

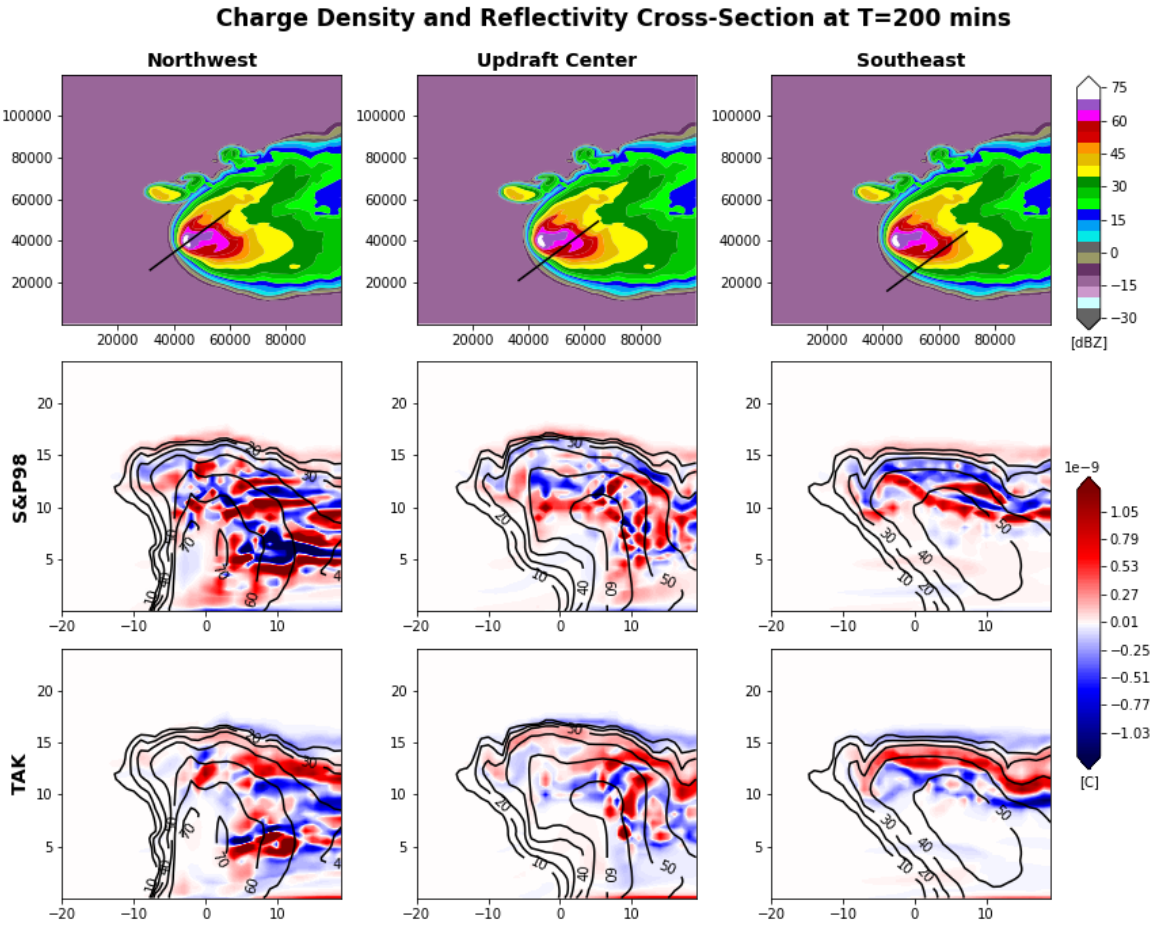

Figure 3.19: Top Row: Aerial view of composite reflectivity with parallel cross sections marked in black at T=200 minutes for Geary, OK. Middle Row: Parallel cross sections of charge density in coulombs (C) using 3M SP98 500 CCN simulation from southwest to northeast Bottom Row: Same as middle row using 3M TAK 500 CCN simulation. X and Z axis in kilometers

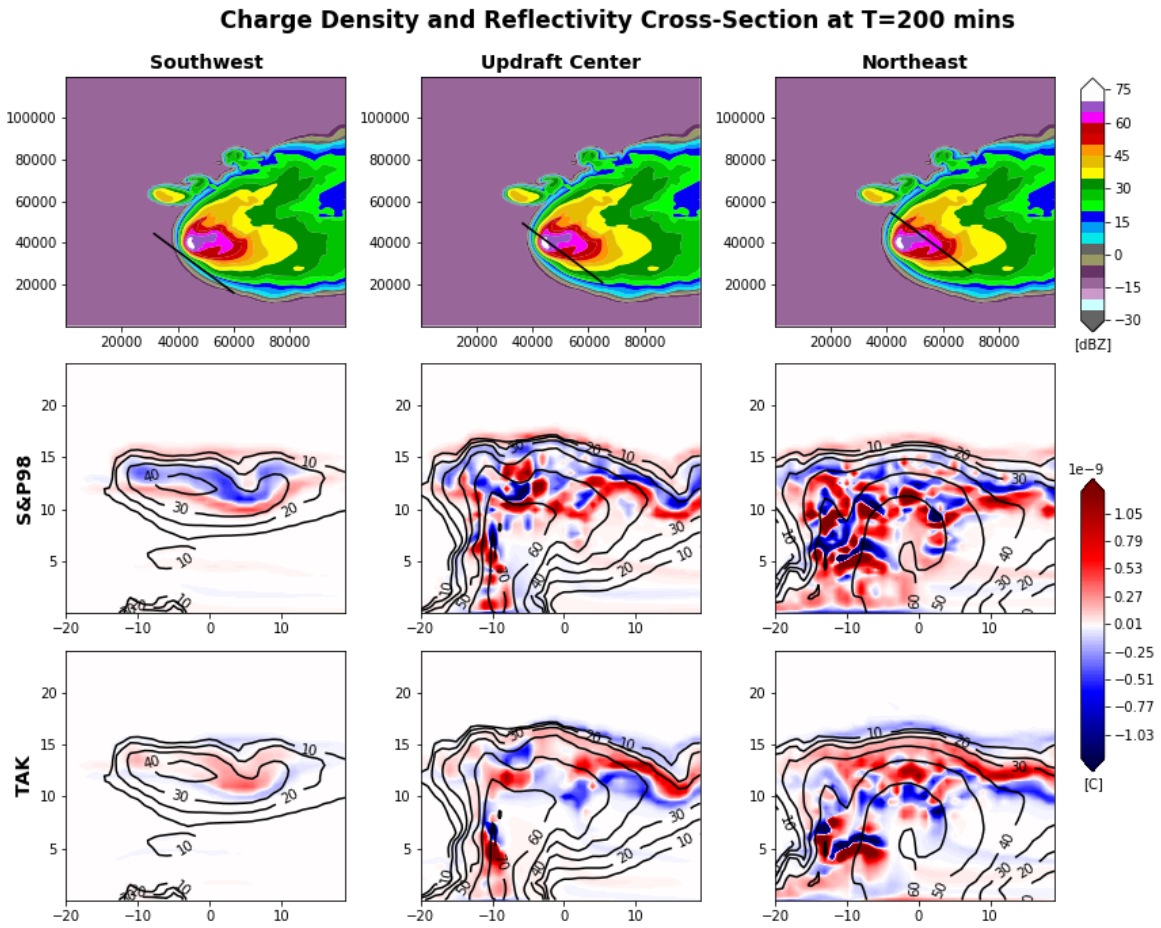

Figure 3.20: Same as in Fig. 3.19, but cross sections done perpendicularly and plotted from northwest to southeast

Electric potential is also plotted along these cross-sections (Fig. 3.21 & 3.22). Electric potential gives a clearer picture of where lightning would initiate and propagate, especially when the charge has complex small-scale structure as it does here. The polarity of the electric potential under the SP98 simulation is opposite to that of the TAK simulation. The rear flank shows more complexity in the electric potential in the SP98 simulation then in the TAK simulation

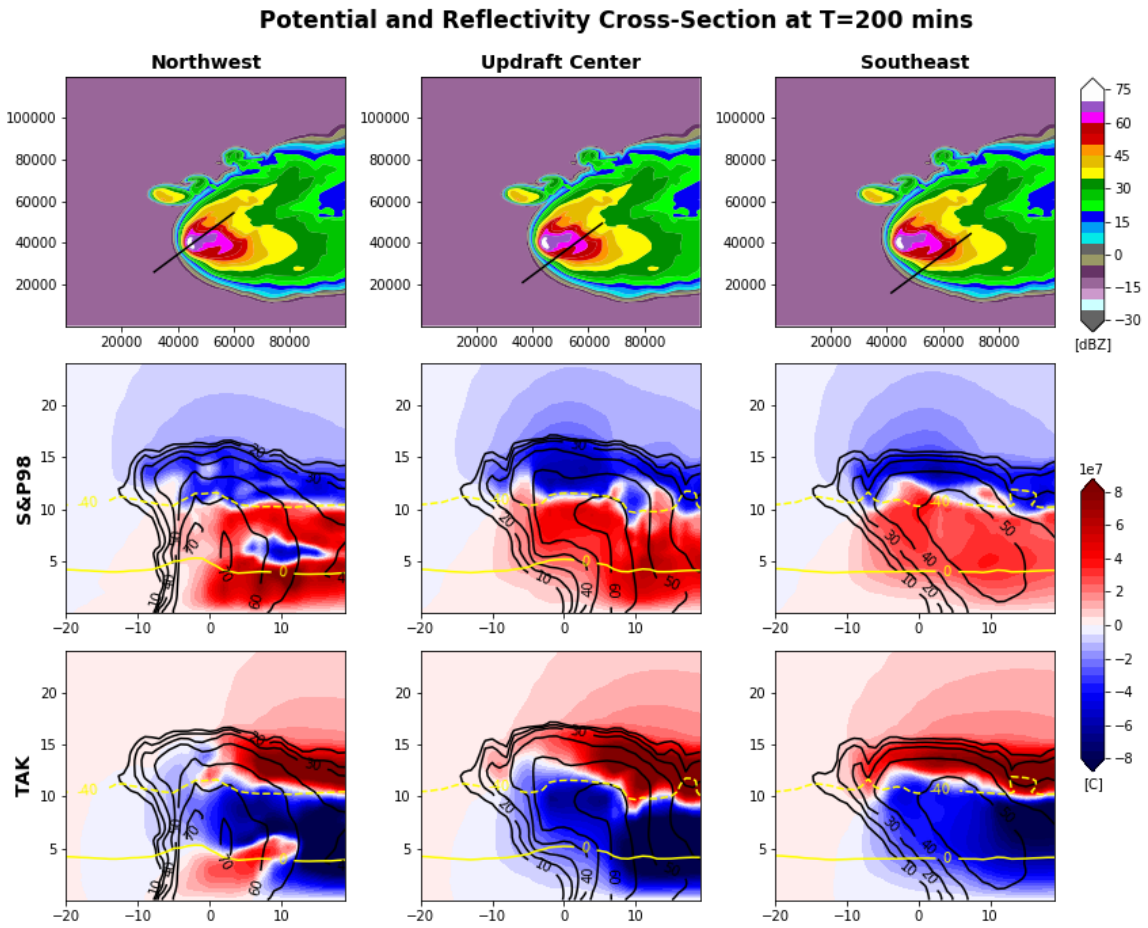

Figure 3.21: Top Row: Aerial view of composite reflectivity with parallel cross sections marked in black at T=200 minutes for Geary, OK. Middle Row: Parallel cross sections of electric potential using 3M SP98 500 CCN simulation from southwest to northeast, with reflectivity overlaid in black contours and ambient temperature in yellow contours (dashed is -40^{o}C and solid is 0^{o}C). Bottom Row: Same as middle row using 3M TAK 500 CCN simulation

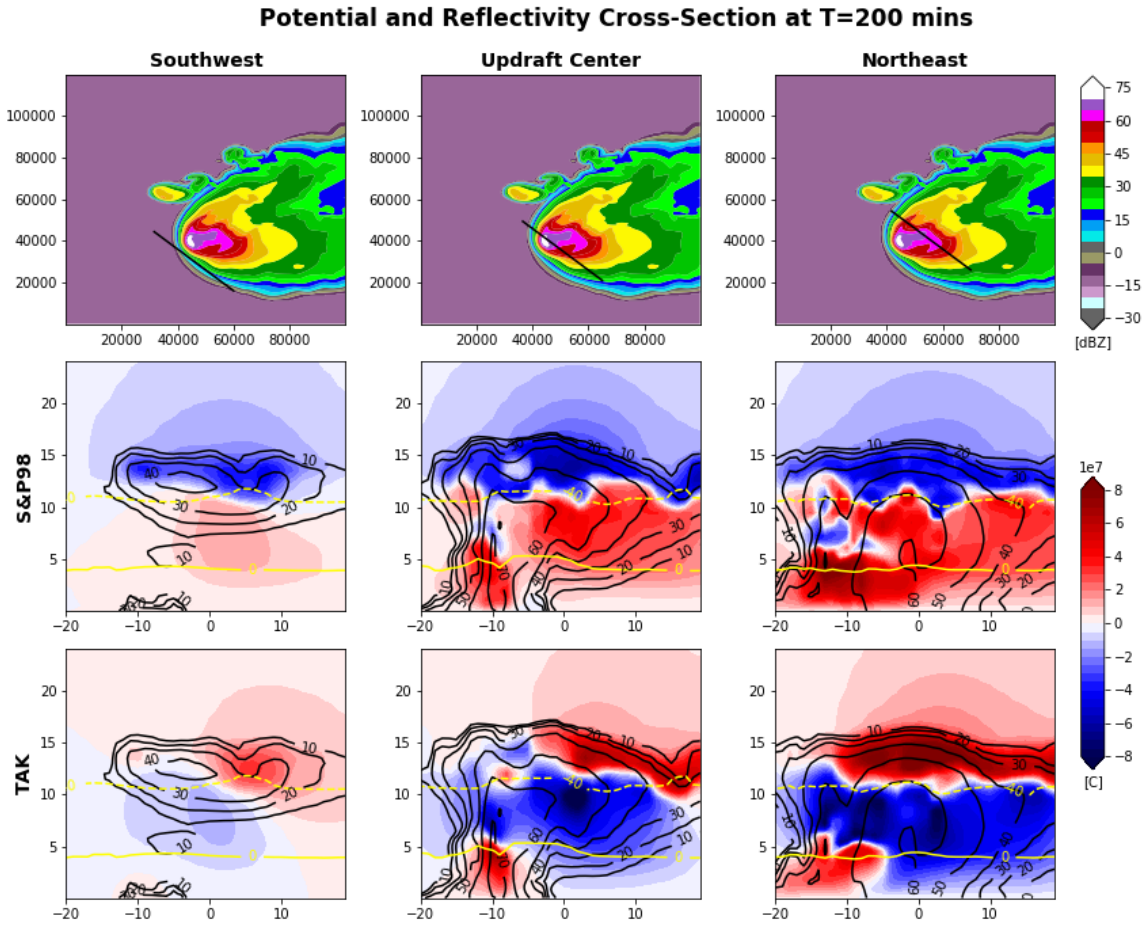

Figure 3.22: Same as in Fig. 3.21, but cross sections done perpendicularly and plotted from northwest to southeast

Differences were also seen in average flash area across the five CCN concentrations. The control set of simulations produced smaller average flash areas at higher CCN concentrations (Fig. 3.23). The median flash area at 100 CCN cm^{-3} was around 150 km^2 and was 100 km^2 for the 4 higher CCN concentrations. Recall, the highest flash rates were at the highest CCN concentrations for both the SP98 and TAK NI charge scheme. This suggests that, in the control simulations at least, as flash rates increase with CCN concentrations, the average flash areas decrease, as might be expected by

the typical inverse relationship between flash rates and areas (e.g., Bruning and Macgorman, 2013). However, the TAK charging scheme produced contrary results. At higher CCN the TAK simulations produced larger average flash areas. The median flash area was around 50 km^2 at 100 and 300 CCN cm^{-3}, and around 100 km^2 for the three higher CCN concentrations. This would suggest that at higher CCN, the TAK simulations are producing fewer yet larger flashes. In either NI charge scheme, the distribution in the flash area was narrower at higher CCN concentrations. We hypothesize that this difference between the two NI charging schemes is a response of the charging to the changing microphysical conditions and the horizontal homogeneity over which that occurs. The TAK NI charge scheme is perhaps more sensitive to the cloud water content, which is higher at higher CCN concentrations.

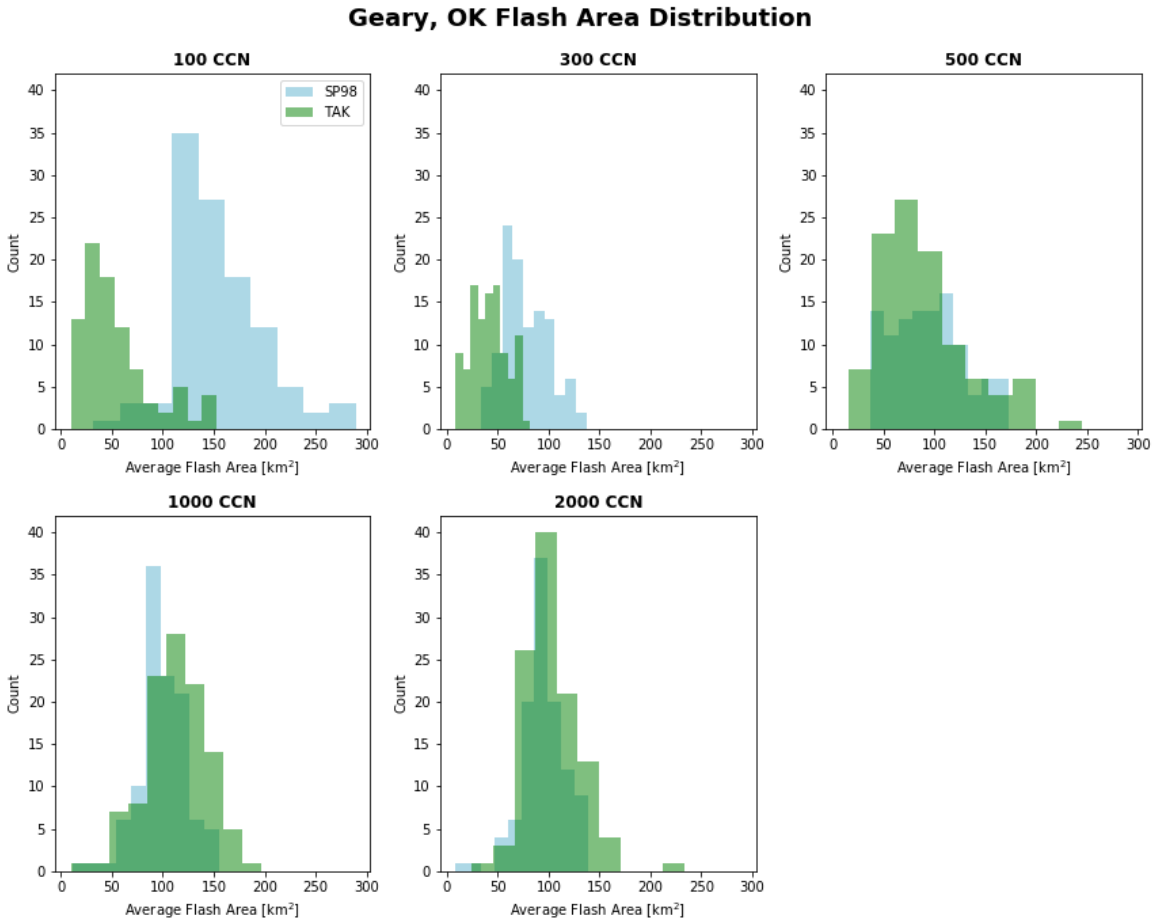

Figure 3.23: Distribution of average flash area (km^2) for the Geary, OK (3M simulations). SP98 NI charging scheme plotted in blue, TAK NI charging scheme in green

Chapter 4

Kimball, NE Case Study

4.1 Dynamic Structure

Similar responses to CCN concentrations were produced in the LP Kimball NE simulations as in the HP Geary, OK supercell. The simulations with different CCN also produced differences in timing, spatial extent, cold pool formation, and updraft strength in the LP case study. The dynamic structure of this supercell was also analyzed using the 2- and 3-moment microphysics as a sensitivity test. Similar to the Geary, OK supercell, only the simulations with the SP98 scheme will be analyzed in this section.

Kimball, NE Supercell Evolution					
	100 CCN	300 CCN	500 CCN	1000 CCN	2000 CCN
Initial Precipitation	15 minutes	17 minutes	20 minutes	20 minutes	22 minutes
Initial Flash	26 minutes	26 minutes	24 minutes	24 minutes	24 minutes

Table 4.1: Table of important times in the evolution of Kimball, NE simulations (control set)

The initial onset of precipitation was delayed at higher CCN concentrations (Fig.4.1, Table 4.1). Using the control set, the 100 CCN cm^{-3} simulation shows precipitation

starting around T=15 minutes into the simulation, at T=17 minutes for 300 CCN cm^{-3}, T=20 minutes for 500 and 1000 CCN cm^{-3}, and T= 22 minutes for 2000 CCN cm^{-3}. Like the Geary case, slight differences in timing were noted between the 2M and 3M simulations, but the overall pattern of delayed precipitation at higher CCN concentrations remained the same (Fig.4.2). This further supports the finding by Twomey (1977); Albrecht (1989), and Gunn and Phillips (1957). The altitude of the initial precipitation also increased with increasing CCN, with the 100 CCN cm^{-3} simulation producing the initial precipitation at altitudes around 3 km, while the 1000 and 2000 CCN cm^{-3} simulations have the initial precipitation around heights of 5 to 6 km, illustrating the delay of the warm rain process and transition to more dominant cold rain processes contributing to precipitation.

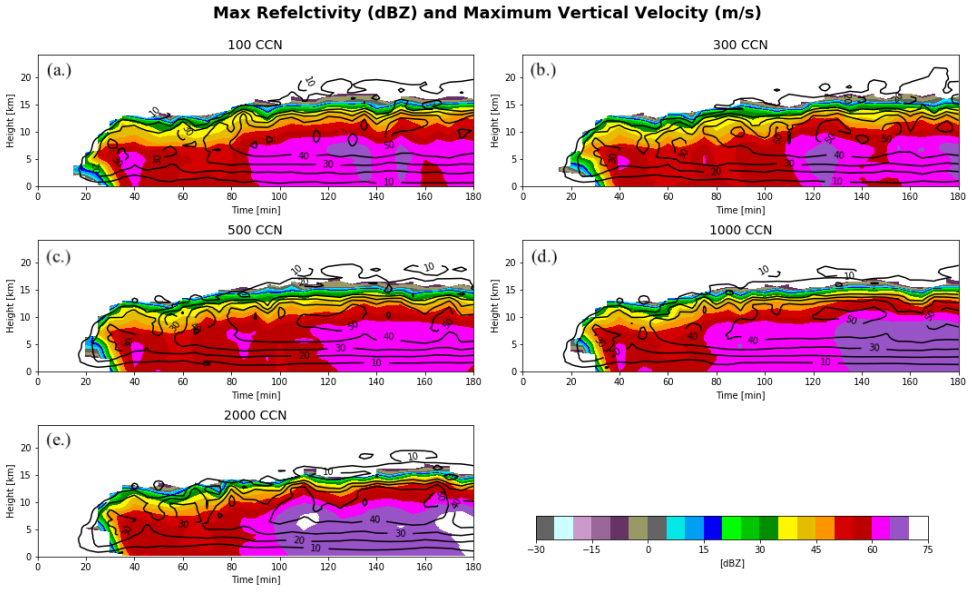

Figure 4.1: Time-height plot of maximum (reflectivity (color fill; dBZ) and maximum vertical velocity (black contours; m/s) for Kimball, NE case simulations (control simulations) just for the right-moving cell

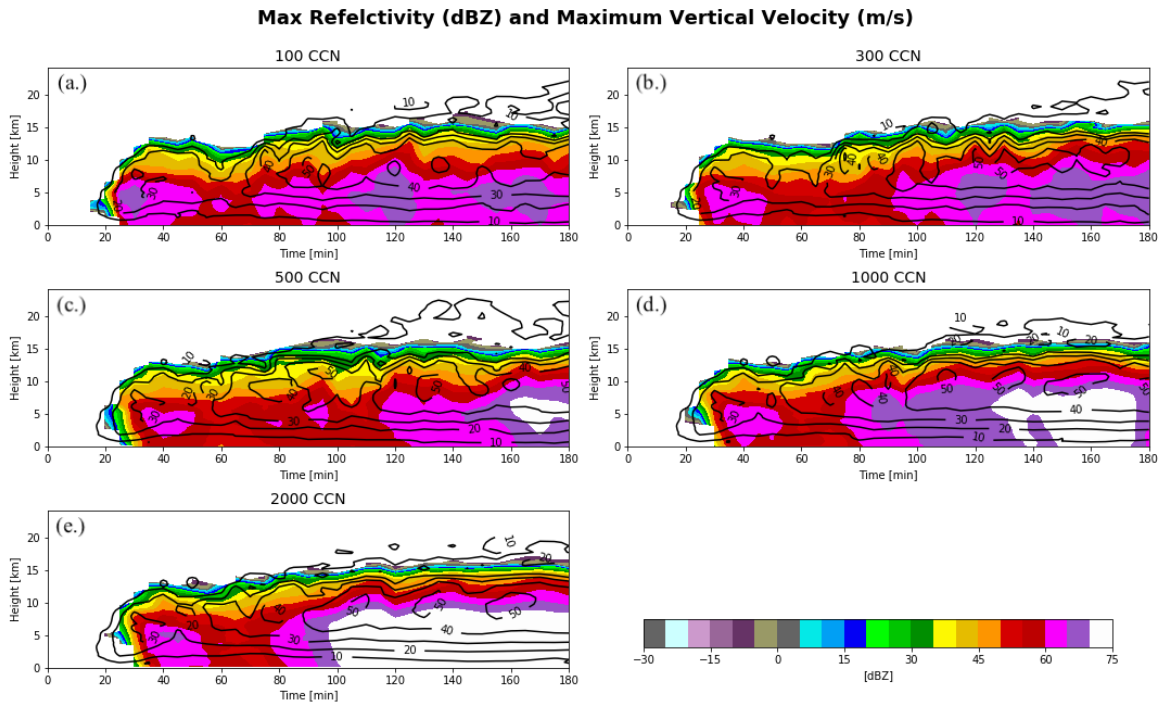

Figure 4.2: Same as Fig. 4.1, but with 2M

Like the Geary case, hail and cloud ice concentrations were higher, while graupel concentrations and mass were lower at higher CCN concentrations (Fig. 4.3 & 4.4). At higher CCN concentraions, these warm and cold rain processes occcured at higher altitudesproducing an increase in presence of frozen hydrometeors (Fig. 4.5).

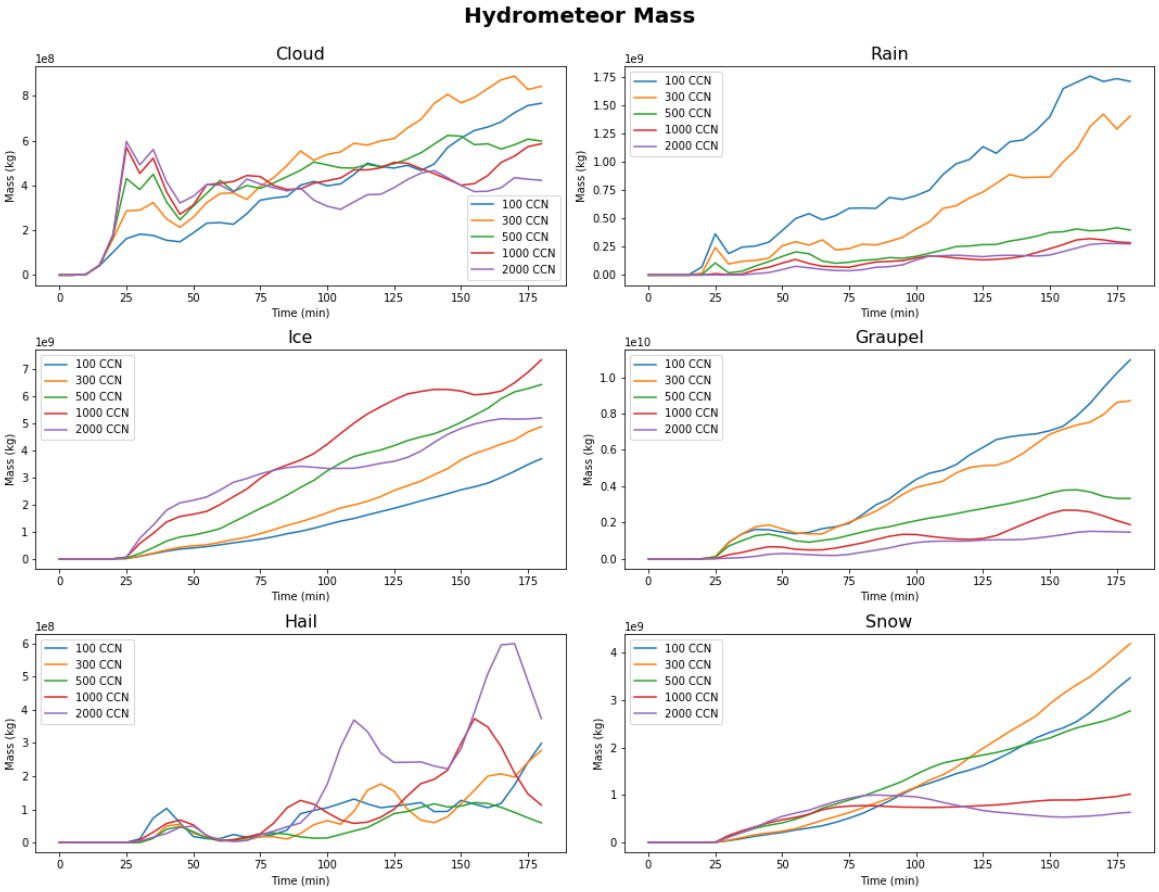

Figure 4.3: Integrated hydrometeor mass (kg) with time for the Kimball, NE case over entire domain (control simulations)

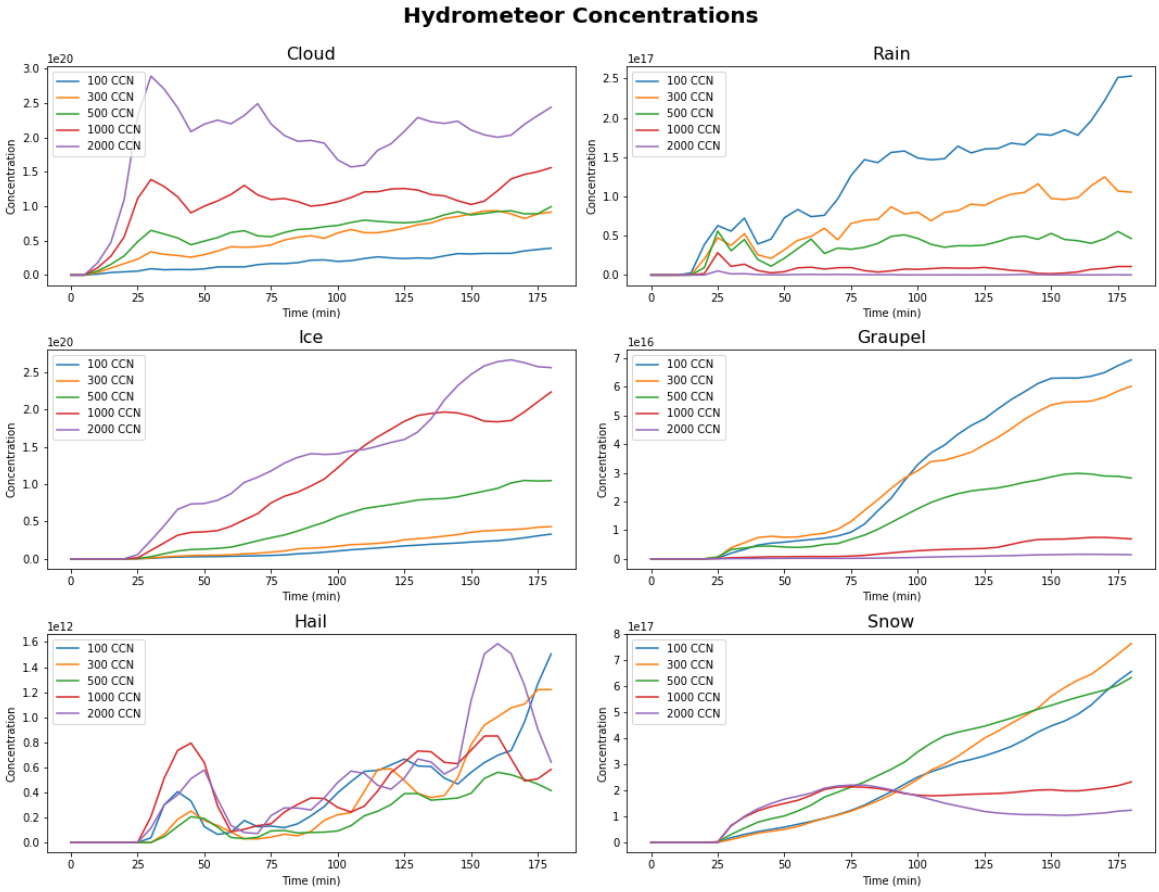

Figure 4.4: Integrated hydrometeor concentrations (count) with time for the Kimball, NE case over entire domain (control simulations)

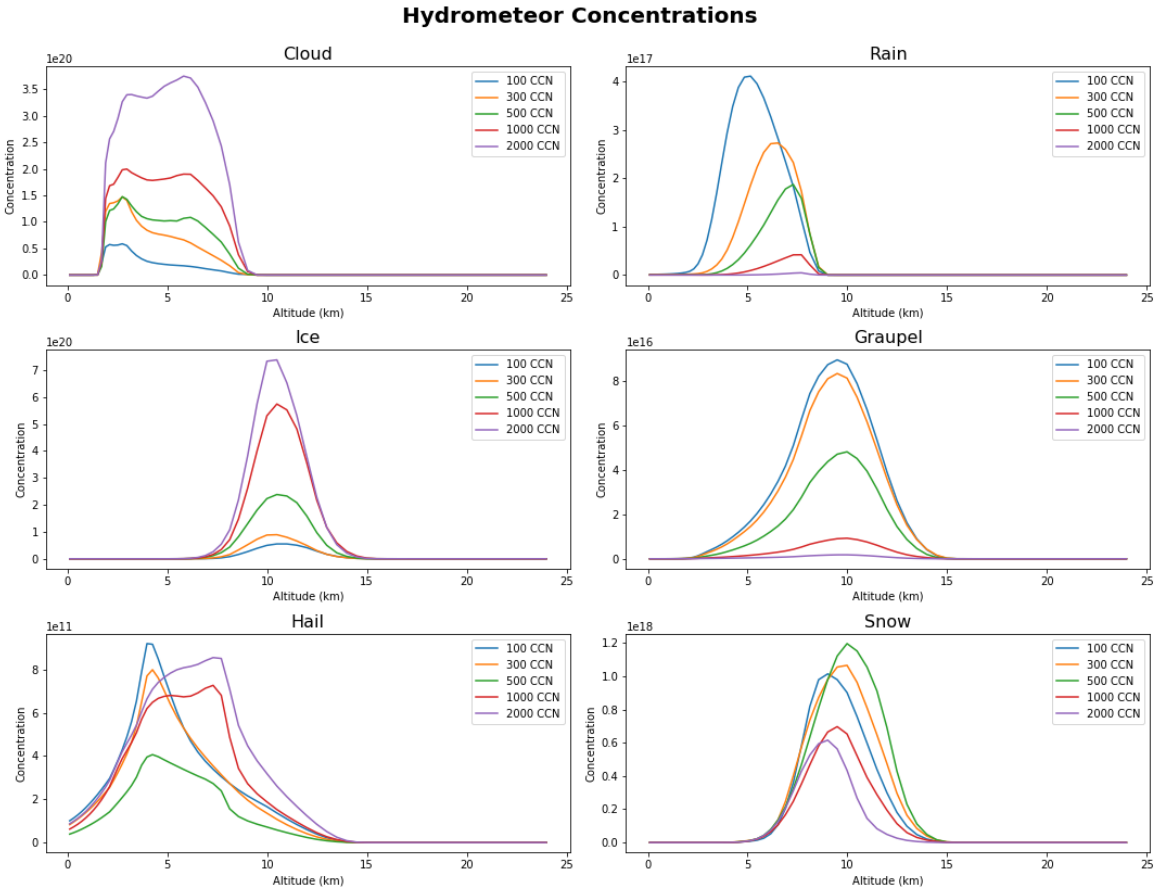

Figure 4.5: Integrated hydrometeor concentrations (count) with height for the Kimball, NE case over entire domain (control simulations)

The evolution of this supercell also displayed differences amongst the different CCN concentrations. The overall horizontal spatial extent of the storm decreased with increasing CCN (Fig. 4.6). The control set produced a small storm split in the 100 CCN cm^{-3} at the beginning of the simulation, that was not observed in the higher concentration simulations. This split was more prominent in the 2M scheme but was also only observed in the lowest CCN concentration simulation (not shown). Towards the end of the 3M simulations, secondary convection arose just east of the main updraft in the low CCN cases, but this did not appear in the higher CCN concentrations, with the

2000 CCN case maintaining one single updraft throughout the simulation.At higher CCN concentrations, the reflectivities appeared to be consistently higher. The highest reflectivities were produced in the 2000 CCN case at around 70 dBZ in the last twenty minutes of the storm (Fig. 4.1). This is seen in the time-height plot in Figure 19 and is even more apparent in the 2M set of simulations where reflectivities were typically higher than the control set of simulations (Fig. 4.2). This may be the result of hail growth in one continuous updraft, while the lower concentrations had cycling through various updraft centers.

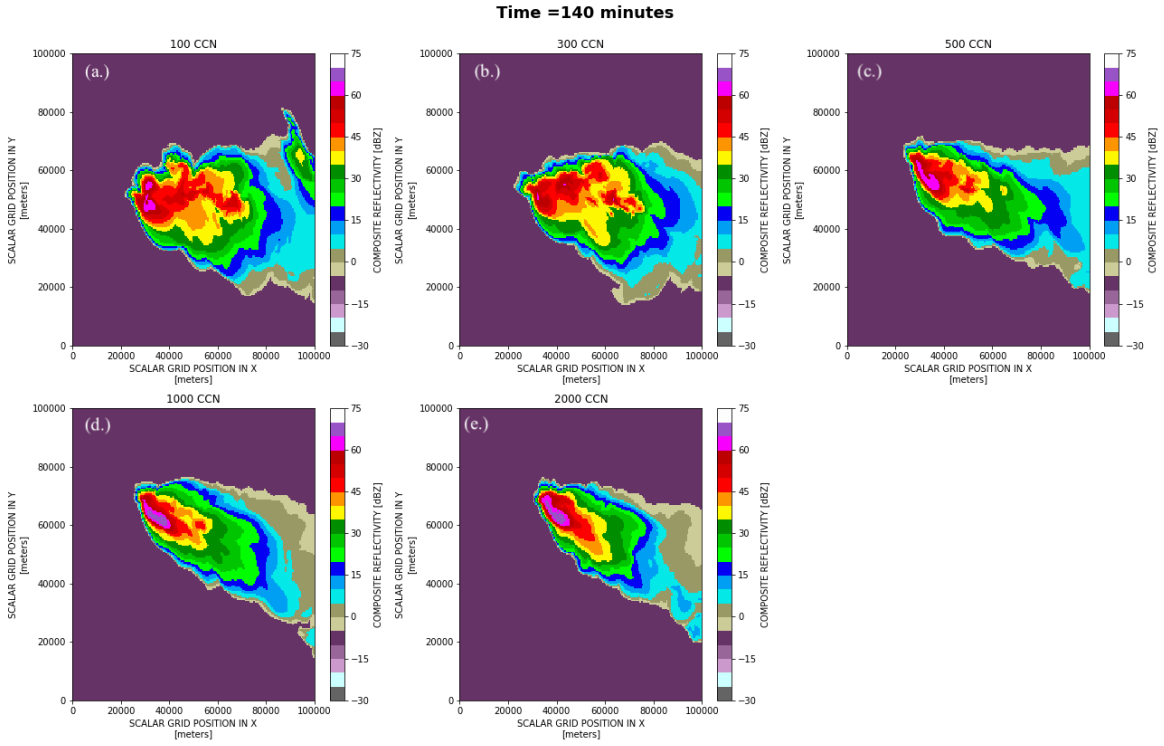

Figure 4.6: Aerial view of composite reflectivity (dBZ) of the Kimball, NE storm (control simulations) at time T=140 minutes

Throughout the storm's evolution, maximum updraft speed remained relatively similar amongst the five CCN concentrations; although the updraft velocity of the

2000 CCN cm^{-3} case was often lower than the others (Fig. 4.7c). Updraft volumes (>5 m s^{-1}; 10 m s^{-1}) for the five concentrations remained almost identical for the first 50 minutes of the simulation but diverged at later times (Fig. 4.7a,b). With an almost monotonic pattern, the updraft volumes were lower at higher CCN at later times. The 5 m s^{-1} updraft volumes (Fig. 4.7a) for the control set reached higher than 40 km^3 for the 100 CCN cm^{-3} case, but remained below 20 km^3 for the 2000 CCN cm^{-3} case. This matches the findings of our Geary, OK analysis and supports Fan et al. (2009), in which aerosol loading in high windshear environments was found to weaken convection and updrafts.

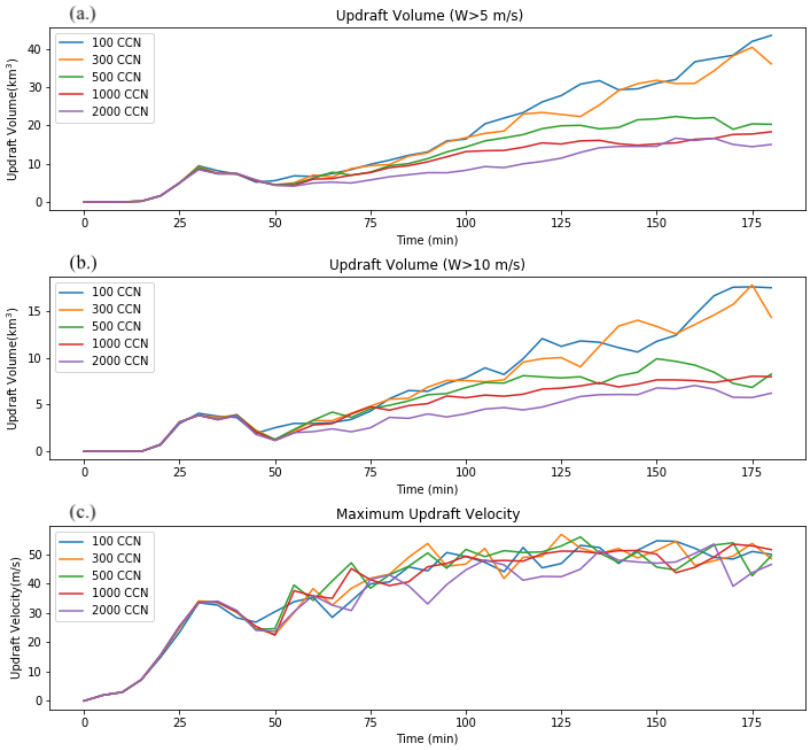

Figure 4.7: a.) Plot of updraft volume for all grid points with vertical motion greater than 5 m s^{-1} with time for Kimball, NE case study (control simulations). b.) Same as in a. but for updrafts greater than 10 m s^{-1}. c.) Maximum vertical velocity with time

The formation of cold pools for this case study showed similar patterns to the Geary, OK supercell, although not as intense in coverage or magnitude. At higher CCN concentrations, potential temperature perturbations were weaker and had smaller spatial coverage (Fig. 4.8). With cold pools being more spatially extensive and having a larger potential temperature perturbation in the very low CCN concentrations, more lift and secondary convection along these potential temperature boundaries would be expected, as seen in the compositive reflectivities (Fig. 4.6). By the end of the simulation (T=180 minutes), the 100 CCN cm^{-3} case had a potential temperature perturbation as strong as -10 ^{o}C, while the 2000 CCN cm^{-3} case had a perturbation of only -5 ^{o}C. Similar to the Geary supercell, the timing of the initial cold pool formation was also delayed and the accumulated surface precipitation was lower at higher CCN concentration (Fig. 4.9), further supporting the findings of Storer et al. (2010); Lerach and Cotton (2012), and Khain et al. (2011).

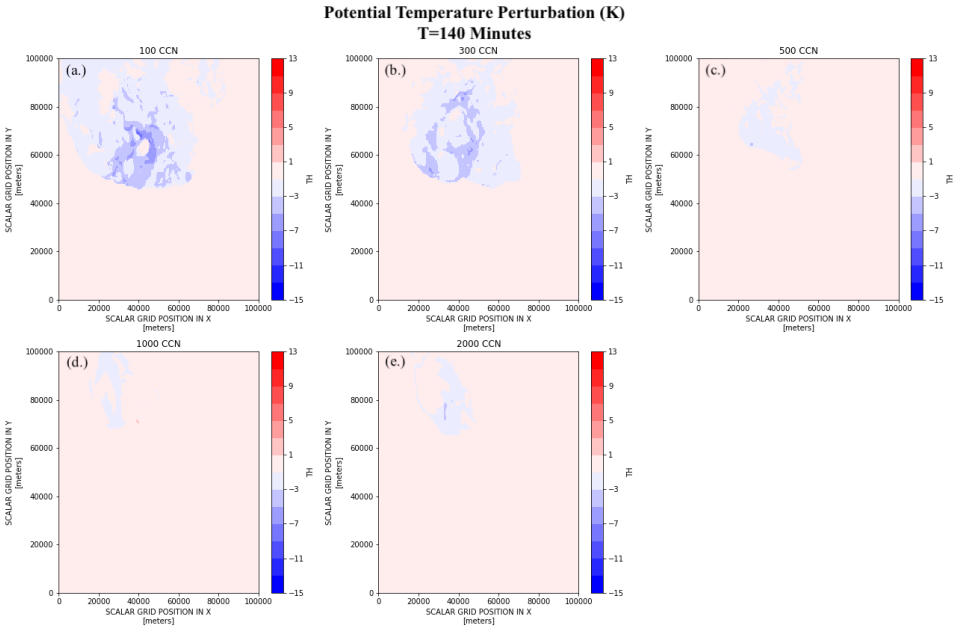

Figure 4.8: Surface potential temperature perturbation (K) at T=140 minutes for Kimball, NE case (control simulations) for 5 CCN concentrations

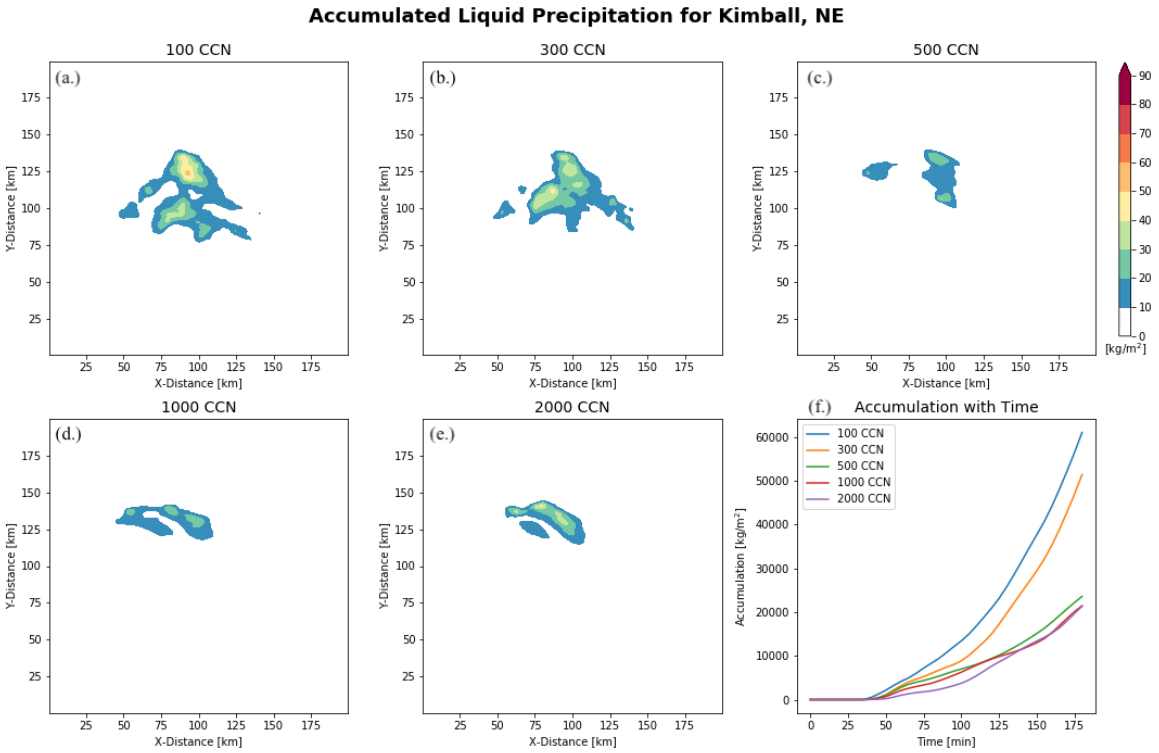

Figure 4.9: Total surface accumulated liquid precipitaion (kg m^{-2}) for Kimball, NE (control simulations) for 5 CCN concentrations. Accumulations are over the entire domain and model run time

4.2 Electric Structure

Similar to the Geary case study, the electric structure of this supercell was examined with two different non-inductive charging schemes as well as the 2- and 3-moment microphysics schemes. To obtain an overview of the average charge structure of the storm throughout its lifetime, average charge density with height was analyzed over the entirety of the simulation for the entire domain for each of the five CCN concentrations. We'll first analyze the electric structure using the SP98 NI charge scheme (our control), and later compare the results to simulations using the TAK charging scheme.

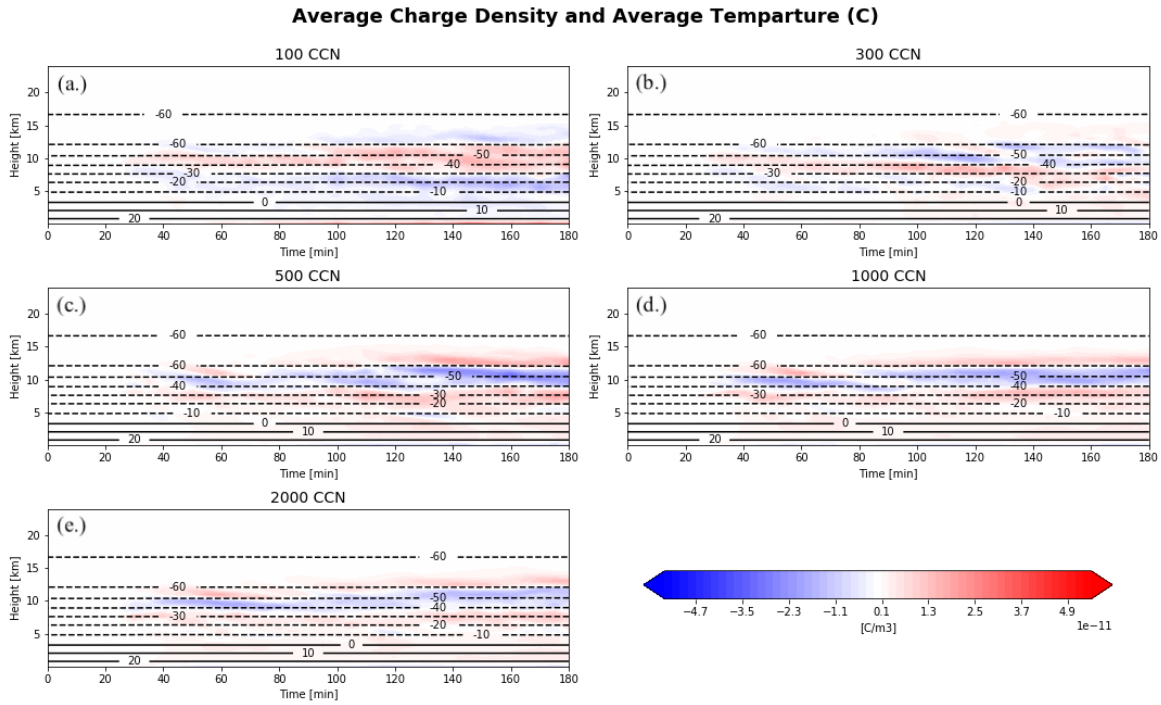

Figure 4.10: Time-height plot of average charge density (fill) and average domain temperature (black contours; ^{o}C) for Kimball, NE (control simulations)

The control simulations in the Kimball, NE case (Fig. 4.10) produced results similar to those of the control simulations of the Geary, OK case. The overall magnitude of charge density in this storm was much lower than that of the Geary case (Fig. 3.10). At 100 CCN cm^{-3}, the supercell maintains a positive dipole structure throughout the simulation, with a negative charge layer from the surface to 7 km, a positive charge layer between 7 and 11 km, and topped by a negative screening layer, near 13 km. As the storm evolved the middle positive charge layer expanded in depth, filling 7 and 12 km by the end of the simulation, with the upper negative layer now extending from 12 km to 15 km. The 300 CCN cm^{-3} simulation starts off with a positive (normal) dipole structure similar to the structure of the 100 CCN simulation for the first 100 minutes of the simulation. Beyond 100 minutes, this positive charge layer builds from the surface

to 5 km, with a 3 km deep layer of negative charge followed by a layer of positive charge between 8 and 10 km, followed by a negative layer between 10 km and 12 km, and topped off by a weak positive layer. As the simulation progresses, the polarity and charge structure of the storm alternates between what might be considered normal and inverted polarity, as averaged layers appear to slowly descend and are later topped by a positive screening layer. The 500 CCN cm^{-3} case starts off with an inverted tripole structure for the first 40 minutes of the simulation, but quickly builds an additional upper positive layer above 11 km and a lower positive charge layer from the surface up to 7 km. The lower negative layer dissipates, while the upper negative layer expands in depth and strengthens in magnitude as the storm evolves. The 1000 and 2000 CCN cm^{-3} simulations had similar charge structures. For the majority of the period these two simulations exhibited a negative dipole structure, with a positive charge layer from the surface to roughly 10 km, a negative region between 10 and 13 km, and a positive region, likely a screening layer, from 13 to 17 km. As the storm evolves the negative charge region expands from a depth of roughly 2 to a depth of 5 km, in both cases. Along with differences in the altitude of these charge layers, the magnitude of net charge within these layers also changes, with the magnitude of charge maximized in the 300 CCN cm^{-3} case. The 2M set of simulations shows charge layers in the same locations for all 5 concentrations, but with slightly stronger magnitudes (Fig. 4.11); however weaker magnitudes were seen in the 2M Geary case. Electric potential for the control set of simulations produced similar results (Fig. 4.12) with a positive dipole structure at 100 CCN cm^{-3} , with opposite polarity at higher CCN concentrations, and alternating polarity in the 300 CCN cm^{-3} case.

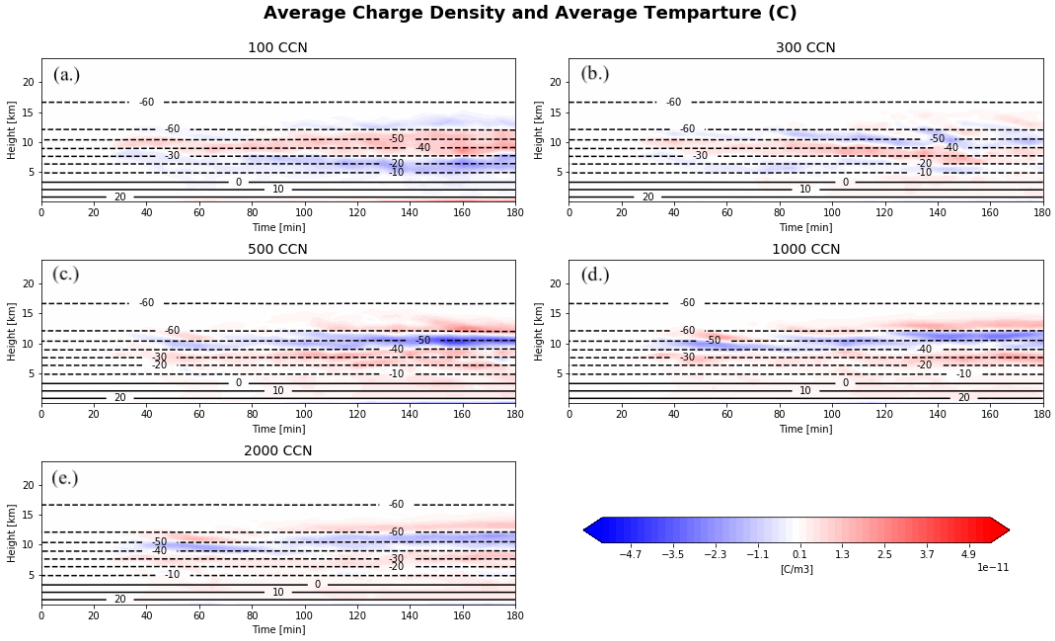

Figure 4.11: Same as in Fig. 4.10, but for 2M set of simulations

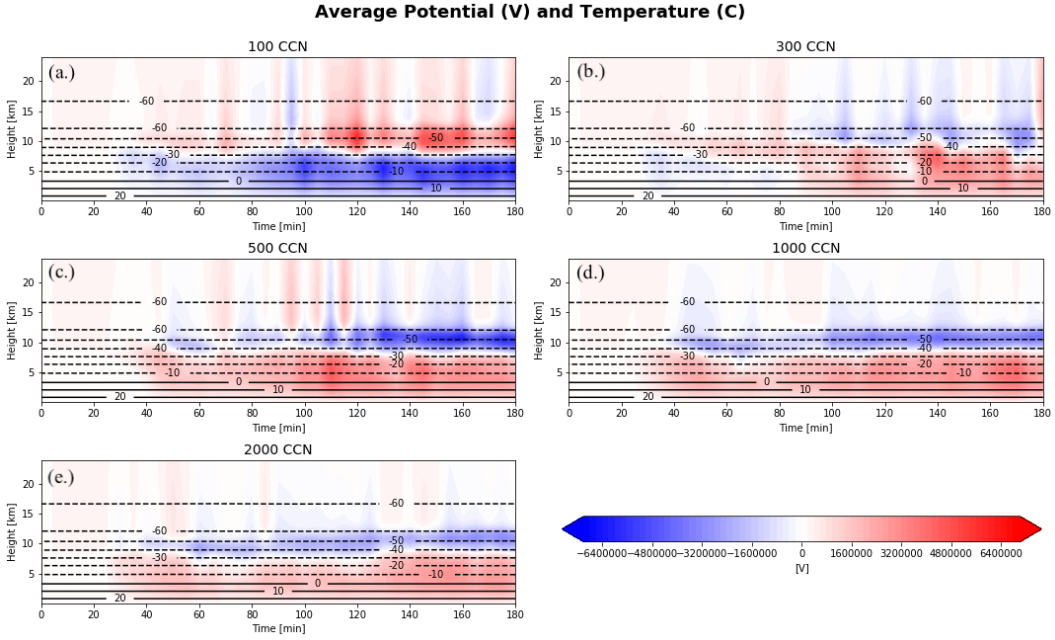

Figure 4.12: Time-height plot of average electric potential (V; fill), average domain temperature (black contours; ^{o}C) for Kimball, NE (control simulations)

In comparison to the Geary case study, the flash rates for this supercell were much lower. The higher CCN concentration simulations produced the highest flash rates (Fig. 4.13a & 4.14). In the control run, flash rates for the 100 CCN cm^{-3} case were around 5 to 10 flashes per minute, while 300 CCN cm^{-3} produced flash rates around 15 to 20 per minute, 500 CCN cm^{-3} up to 20 flashes per minute, and the two highest concentrations up around 30 to 40 flashes per minute. This further supports the findings of Mansell and Ziegler (2013); Altaratz et al. (2010); Pawar et al. (2017); Ren et al. (2018); Kochtubajda et al. (2011).

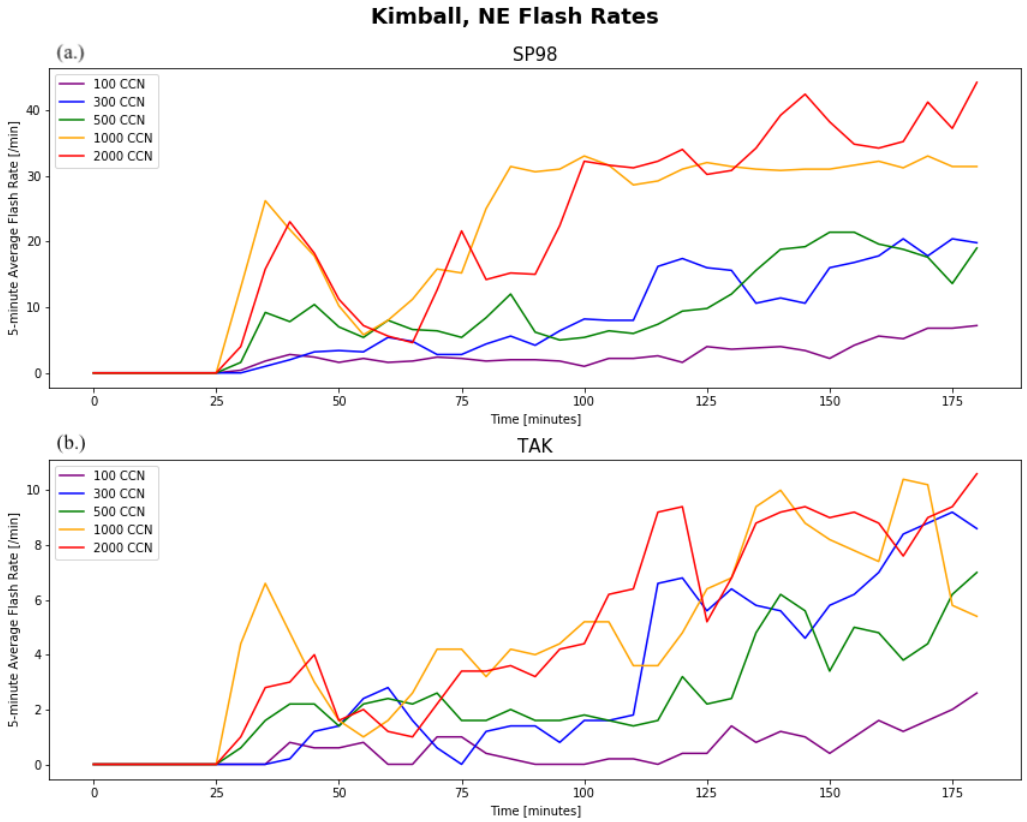

Figure 4.13: a.) Time series of integrated 5-minute averaged flash rate for Kimball, NE (control set) b.) Same as (a.) but for TAK NI scheme

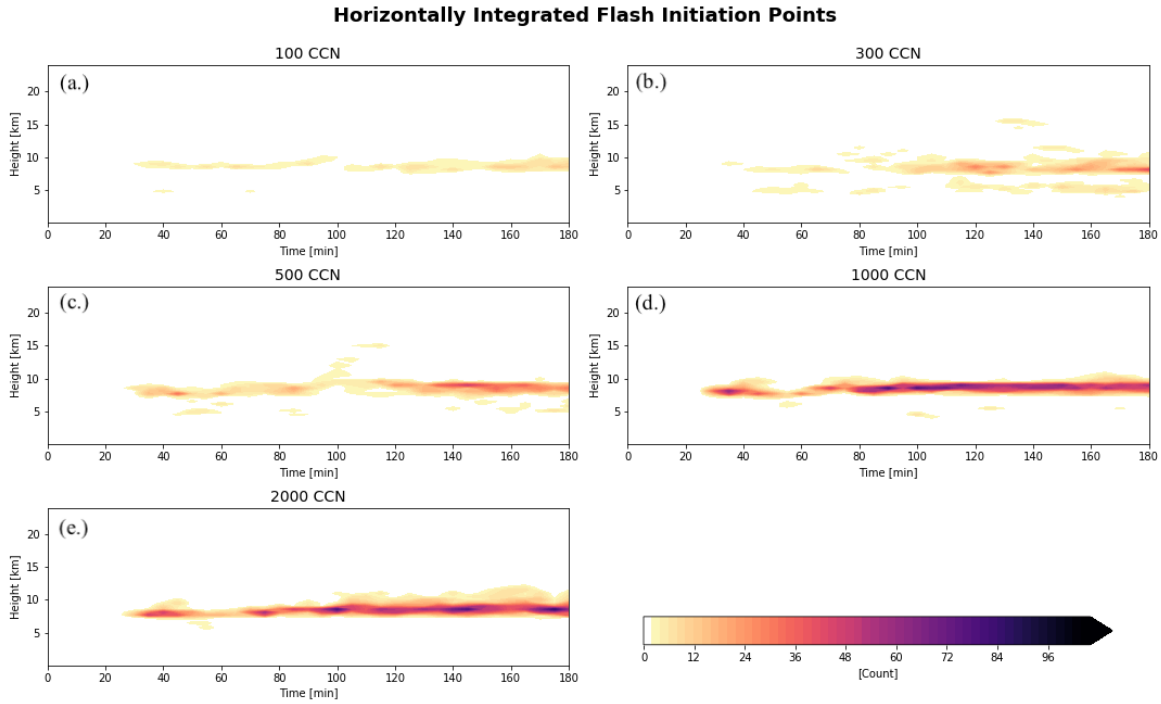

Figure 4.14: Time-height plot of horizontally integrated flash initiation points for Kimball, NE (control simulations). Total flash initiation points at one time is the same as the flash rate.

Unlike the Geary simulations, the majority of flashes were initiated around one single altitude (Fig. 4.14 & 4.15), except for the 300 CCN cm^{-3} case in which flashes initiated in roughly four different layers. Again in the Kimball case, the initial flashes beganaround the same time (T=25 minutes; Table 4.1) for all CCN concentrations. The 2M case showed the same pattern but had overall higher flash rates across all five concentrations (not shown).

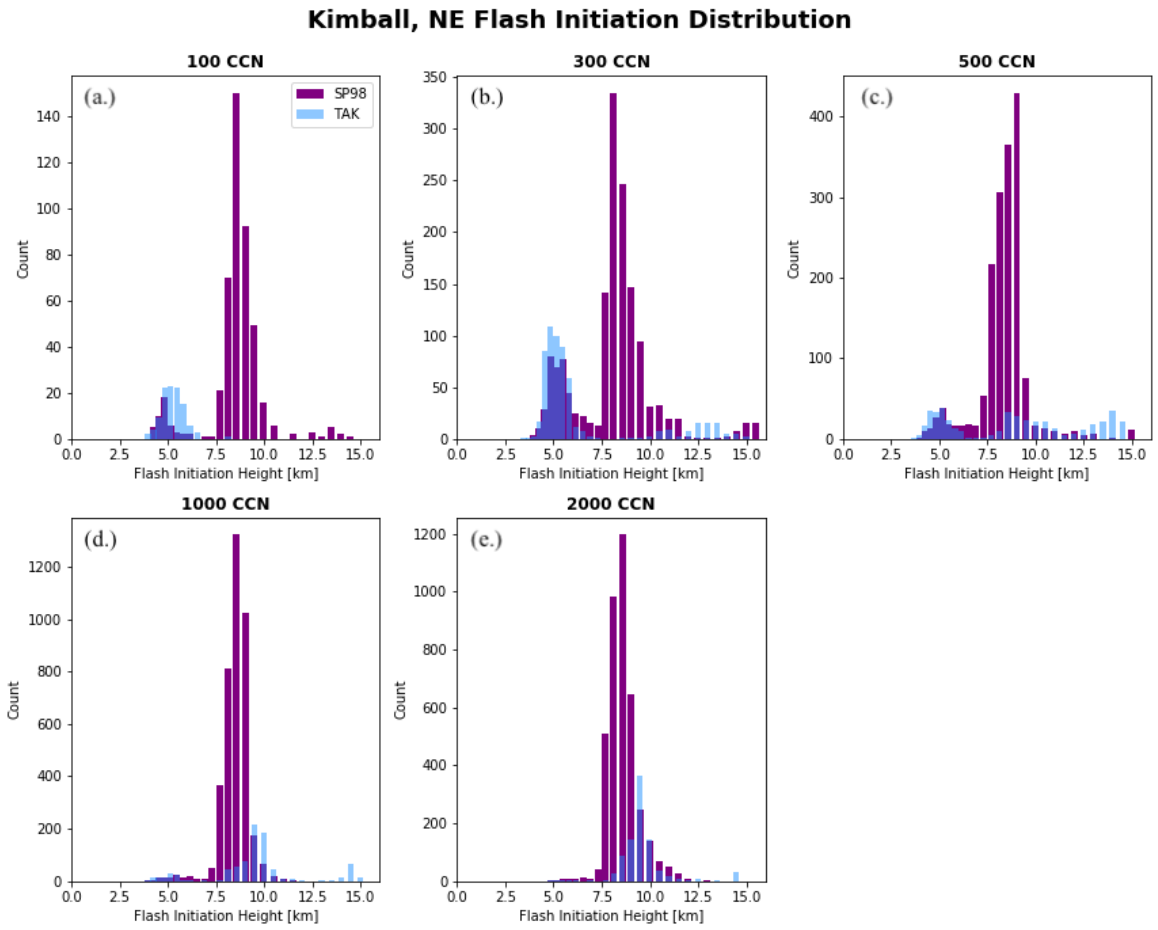

Figure 4.15: Distributions of flash count with altitude for each CCN concentrations. Simulations using SP98 (control) in purple, simulations using TAK NI scheme in blue.

As a comparison, the electrical structure of the Kimball, NE supercell was also analyzed using the TAK NI charging scheme (Fig. 4.16). The 3M TAK simulations produced quite different charge density layers but with roughly the same magnitude of charge as SP98. Similar to the TAK simulations in the Geary case study, no full polarity flip was observed between the lowest and higher CCN simulations. In the 100 CCN cm^{-3} run, an inverted dipole structure is observed, with a positive charge region between the surface and 5 km, a negative region in between 5 and 10 km, topped off by

a positive screening layer. The polarity is opposite to what was seen in most of the SP98 simulations. Like the Geary case, additional negative charge regions are produced by this NI charging scheme below 15 km for the 4 higher CCN concentrations. At higher CCN concentrations, the lower positive region is weaker and shallower as a negative charge region appears at the surface. By the 2000 CCN cm^{-3} case, the lower positive charge region is very weak and almost completely dissipated. The overall average charge structure is more prominent in the time-height plots of electric potential (Fig. 4.17), but rather similar to that of the average charge density.

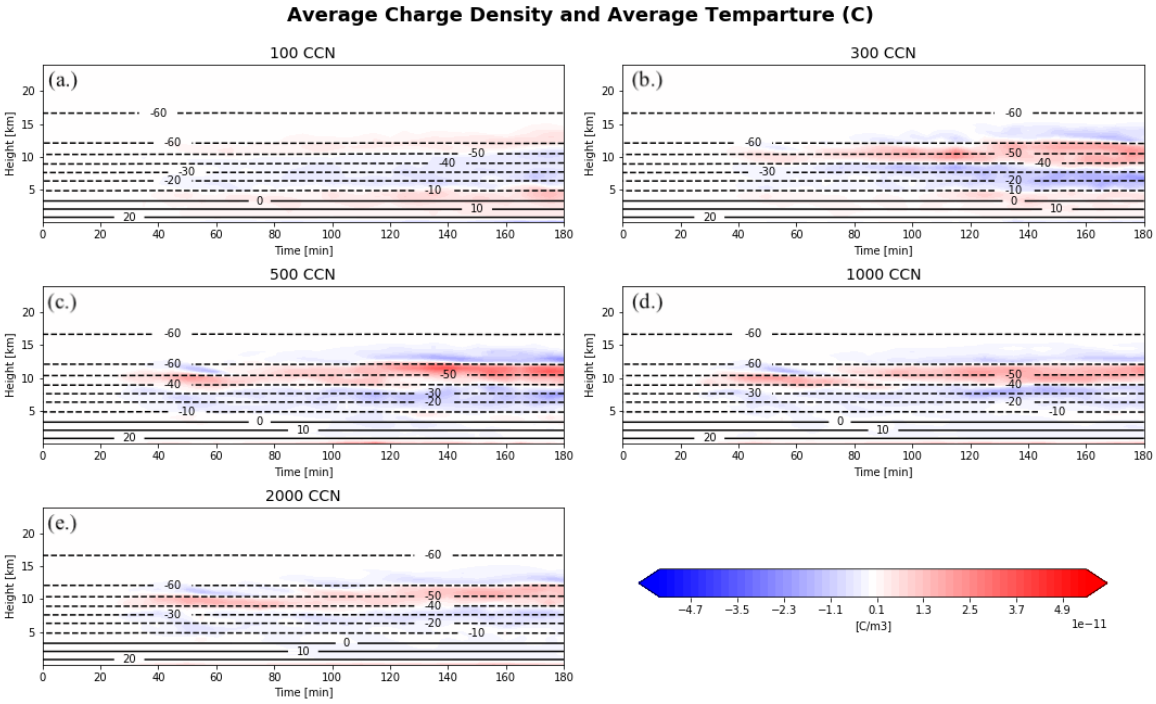

Figure 4.16: Same as in Fig.4.10, but for TAK set of simulations

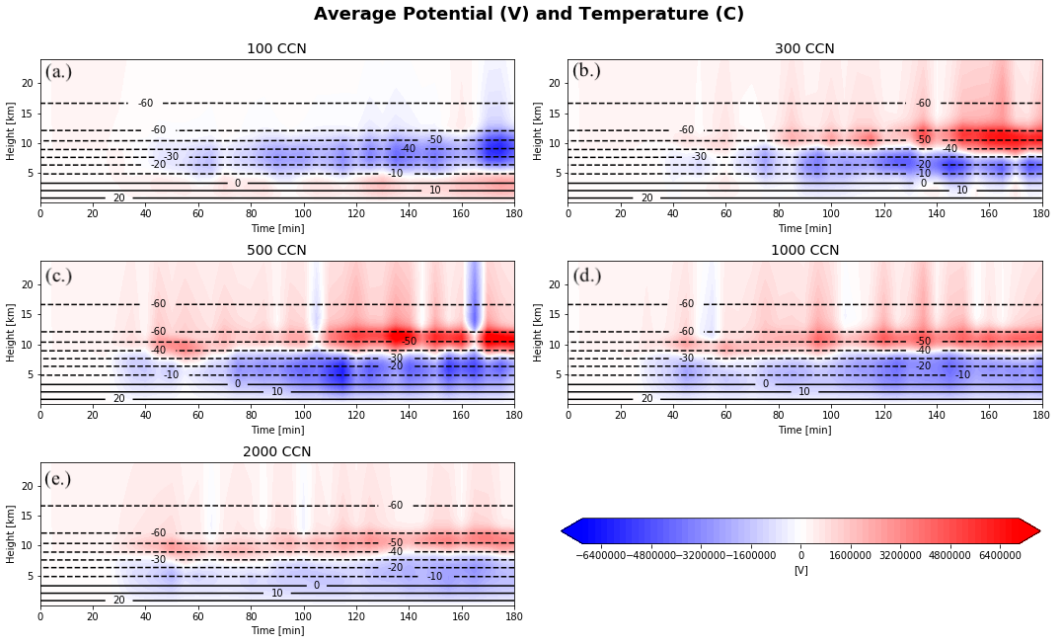

Figure 4.17: Same as in Fig. 4.12, but for TAK set of simulations

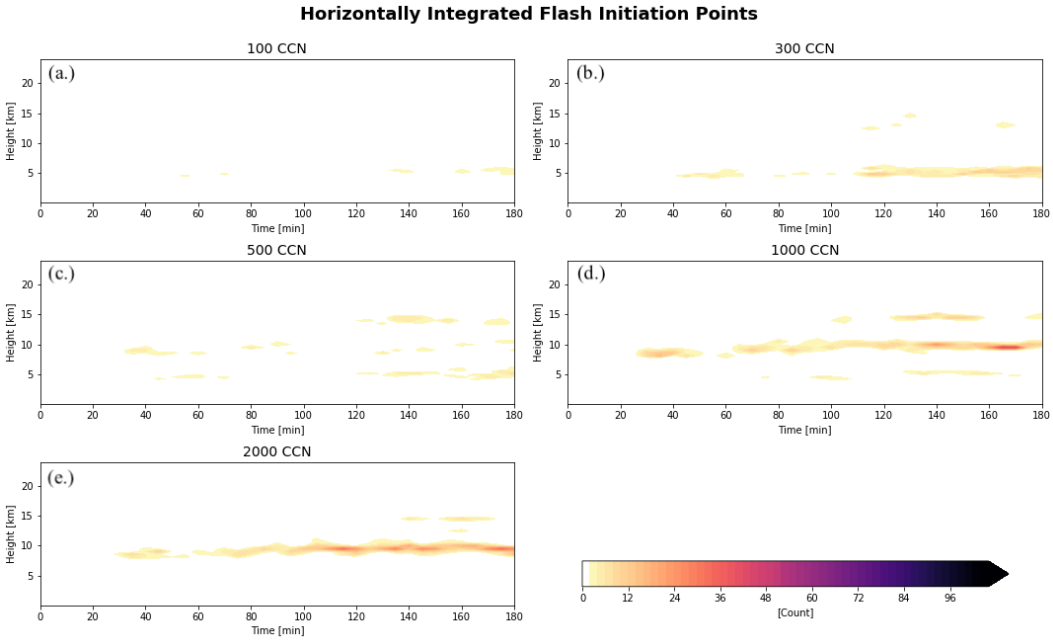

Figure 4.18: Same as in Fig. 4.14, but for TAK set of simulations

Flash rates were again lower with the TAK charging scheme (Fig. 4.13b & 4.18) than with the SP98. For 100 CCN cm^{-3} flash rates were less than 2 per minute, 300 and 500 CCN cm^{-3} had flash rates around 5 flashes per minute, while 1000 and 2000 CCN cm^{-3} had flash rates as high as 8 to 10 flashes per minute. This again raises the unintuitive relationship between low flash rates with this NI scheme and high average charge density magnitudes. The cross-sections at T= 150 minutes again show that the storm's charge layers are much more complicated than the domain average was showing (Fig. 4.19 & 4.20). The sloping of charge layers as you move away from the updraft center is again prominent in this case study. Similar to the Geary, OK case, the SP98 scheme produces a lot of small pockets of charge, especially above the updraft region, while the TAK scheme has more consistent and continuous layers. It can also be assumed here that the domain averaging over these little pockets in the SP98 scheme resulted in the averaging out of charge, ultimately resulting in weaker domain-averaged charge layers. Cross sections of electric potential (Fig. 4.21 & 4.22) also showed opposite polarities between he SP98 and TAK simulations. The SP98 simulations again showed more complexity in electric potential just east of the updraft.

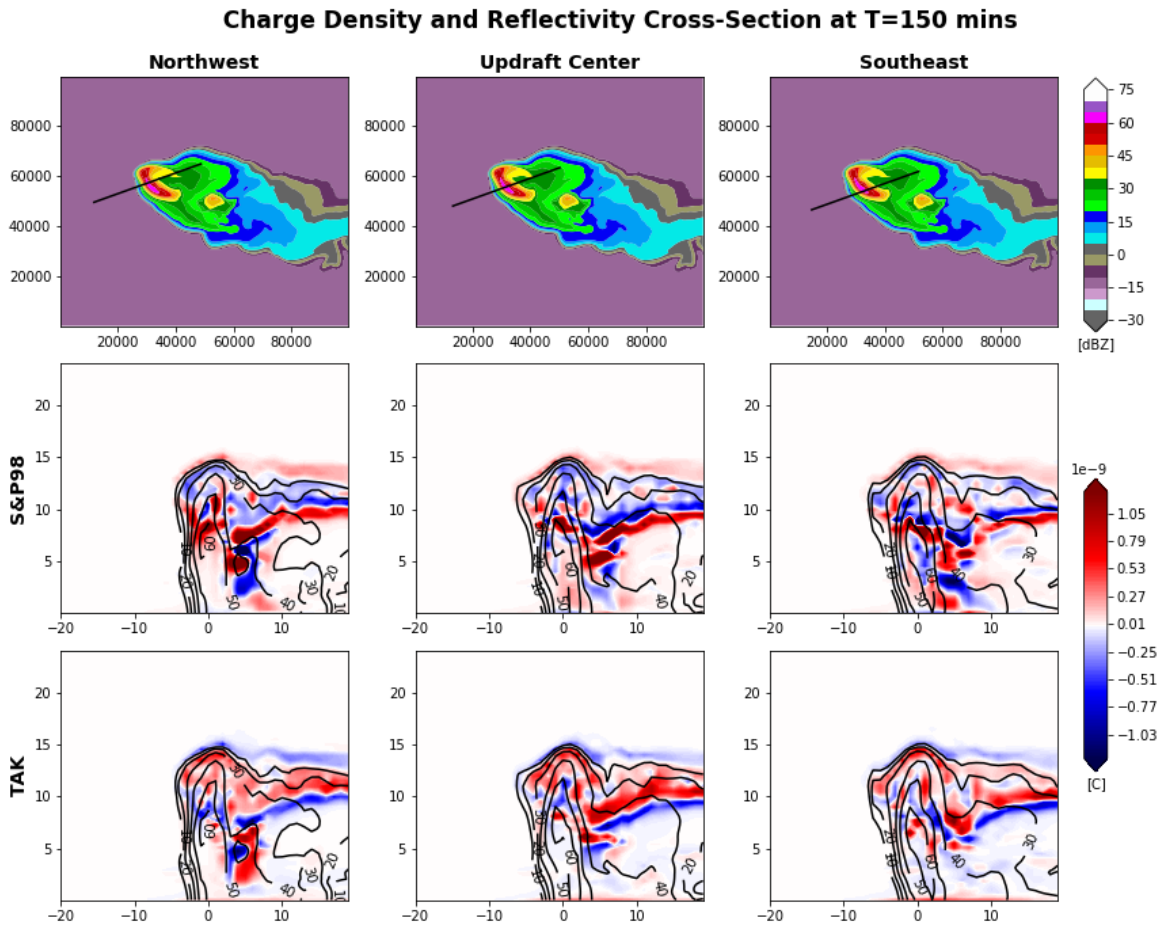

Figure 4.19: Top Row: Aerial view of composite reflectivity with parallel cross sections marked in black at T=150 minutes for Kimball, NE. Middle Row: Parallel cross sections of charge density in coulombs(c) using 3M SP98 500 CCN simulation from southwest to northeast Bottom Row: Same as middle row using 3M TAK 500 CCN simulation

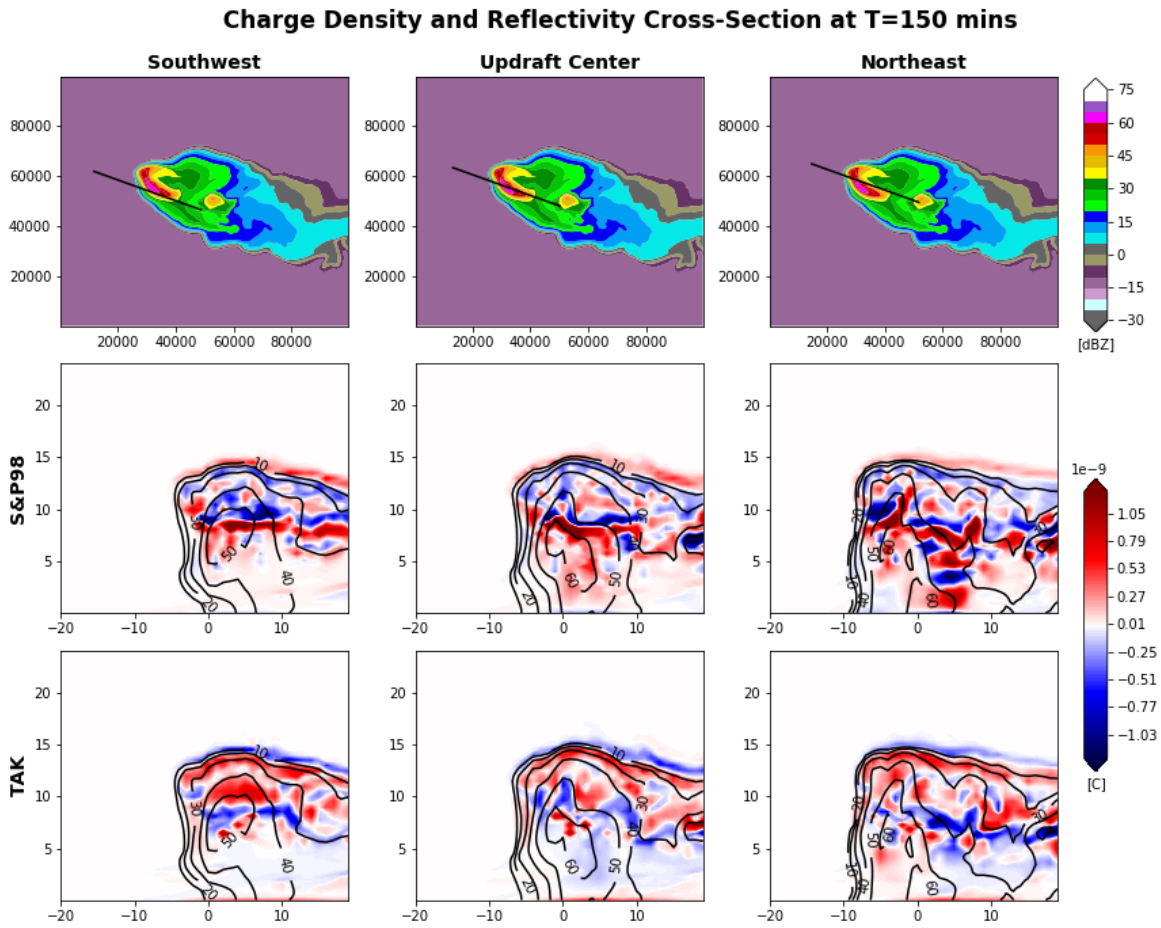

Figure 4.20: Same as in Fig. 4.19, but cross sections done perpendicularly and plotted from northwest to southeast

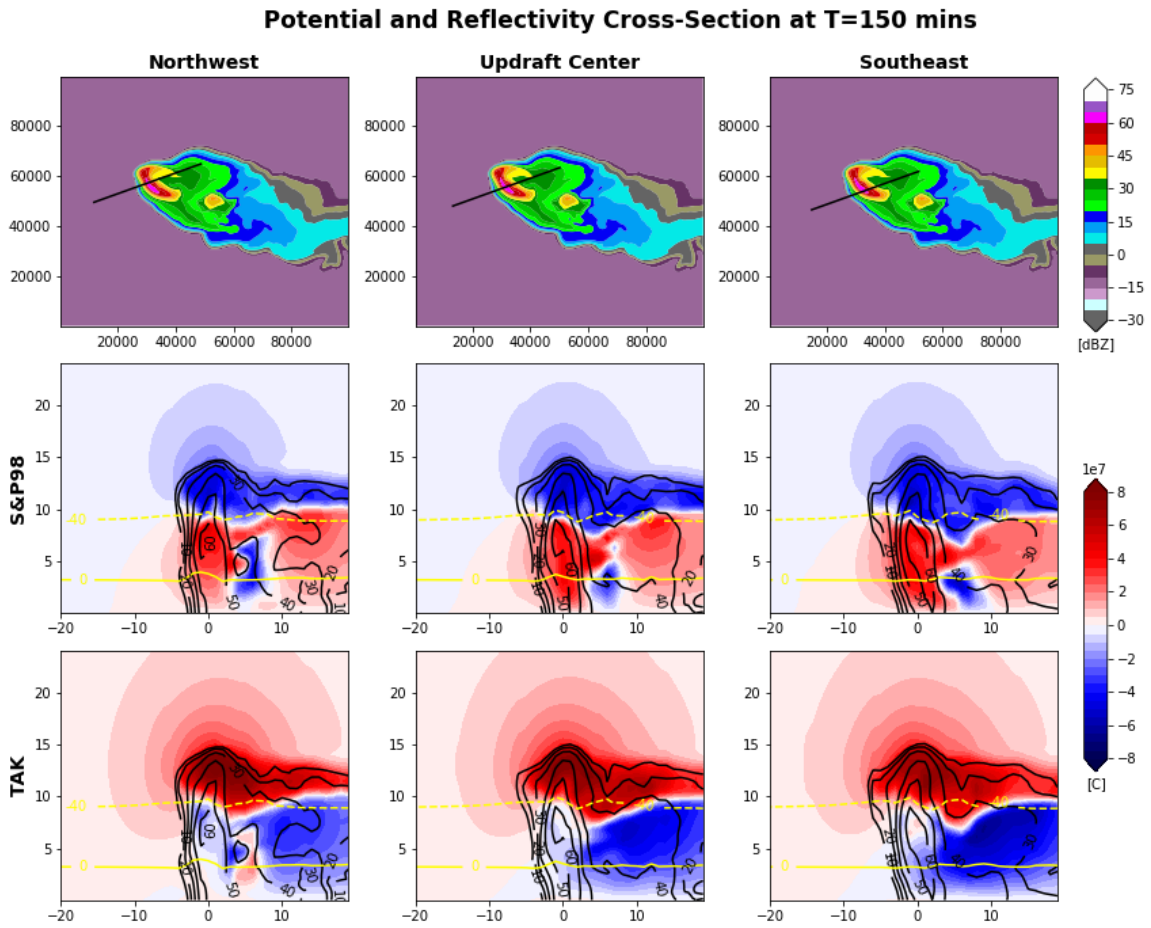

Figure 4.21: Top Row: Aerial view of composite reflectivity with parallel cross sections marked in black at T=150 minutes for Kimball, NE. Middle Row: Parallel cross sections of electric potential using 3M SP98 500 CCN simulation from southwest to northeast, with reflectivity overlaid in black contours and ambient temperature in yellow contours (-40°C represented with a dashed line and 0°C with a solid line). Bottom Row: Same as middle row using 3M TAK 500 CCN simulation

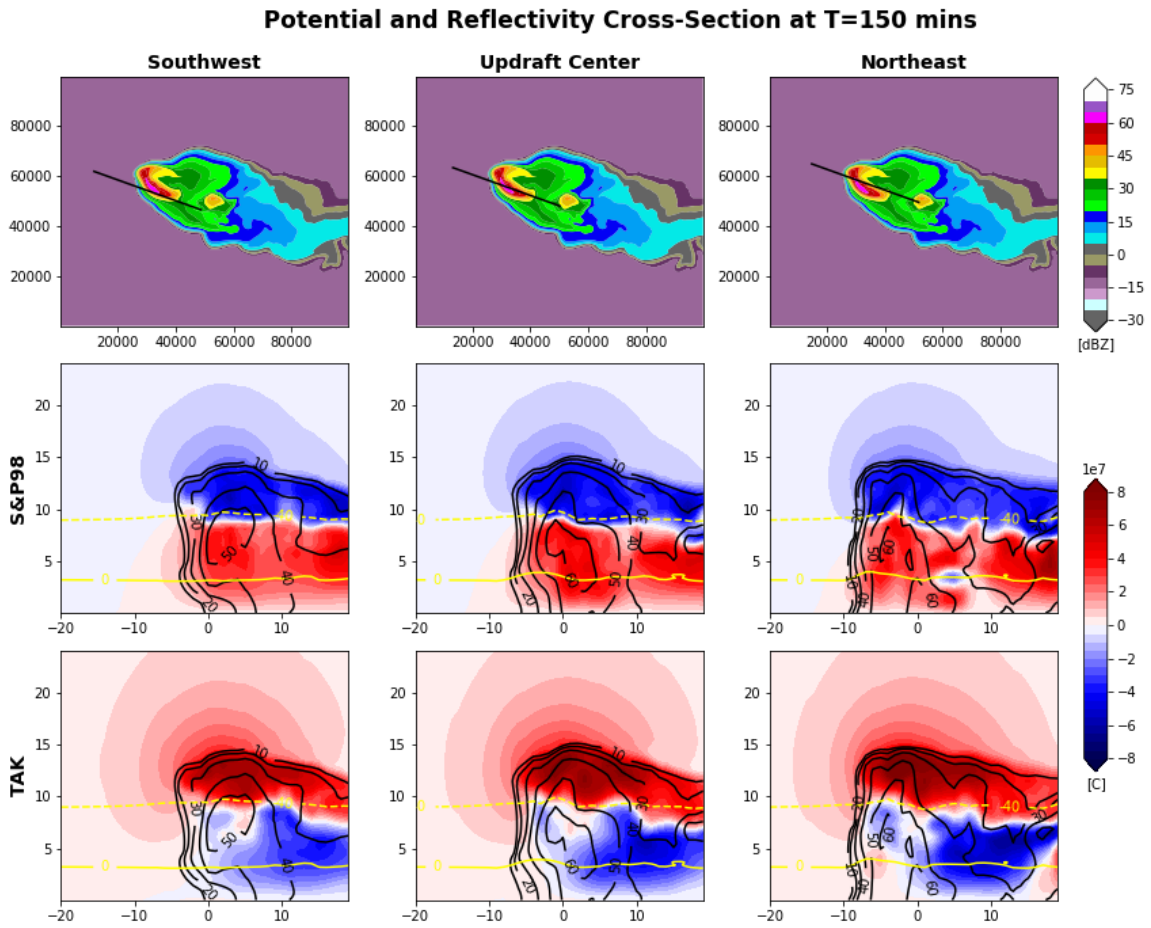

Figure 4.22: Same as in Fig. 4.21, but cross sections done perpendicularly and plotted from northwest to southeast

Similar to the Geary, OK case study, differences also occurred in average flash area across the five CCN concentrations. The control set again produced smaller average flash areas at higher CCN concentrations (Fig. 4.23). The median flash area at 100 and 500 CCN cm^{-3} was around 100 km^2, while median flash area was around 70 km^2 for 300, 1000, and 2000 CCN cm^{-3}. This again follows the typical inverse relationship between flash rates and areas (e.g., Bruning and MacGorman 2013). The TAK simulations produced average flash areas that were relatively consistent across the five

CCN concentrations with a median flash area around 50 km^2. Both NI charge schemes again produced a larger distribution of flash area sizes at lower CCN concentrations, and a very narrow distribution at higher concentrations. Although not as direct, these results would again suggest that the difference produced by changing CCN concentrations between the two NI charging schemes is a response to the changing microphysical conditions and the horizontal homogeneity over which that occurs.

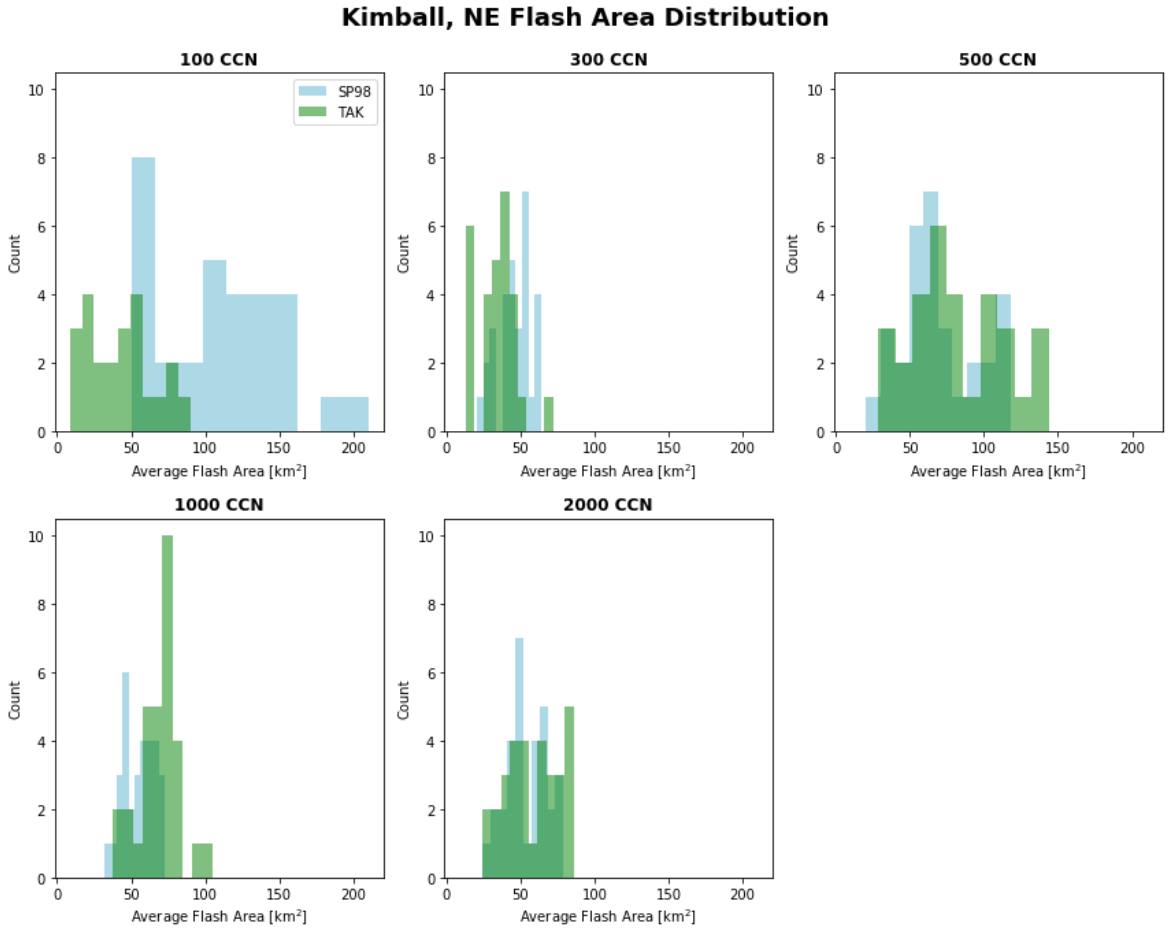

Figure 4.23: Distribution of average flash area (km^2) for the Kimball, NE (3M simulations). SP98 NI charging scheme plotted in blue, TAK NI charging scheme in green

Chapter 5

Comparison to Observations

5.1 Geary, OK

In this section, the control set of simulations from the Geary, OK case will be compared to the SMART radar and OKLMA data, collected in the 2004 TELEX field campaign. All five CCN concentrations exhibited smaller reflectivity values than the radar analyses by roughly 10 dBZ (Fig. 5.1 & 5.2). As found by Calhoun et al. (2014), these lower reflectivities were mostly in the region of the southern overhang and within the back shear anvil and forward flank hail core. The model reflectivity assumes a simple Rayleigh scattering that does not take any effects of resonance or liquid coating, which may account for this difference. For this analysis, simulations at time T=150 minutes were compared to observations at 0016 UTC 30 May, T=160 to 0027 UTC, and T=170 to 0036 UTC. These observations and model times were chosen as the evolution of the hook echo and updraft were similar at these time intervals; however it should be noted that one shouldn't necessarily expect a one-to-one match given the long-lived nature of this supercell.

5.1.1 Dynamic Structure and Evolution

At 0016 UTC (T=150 minutes in the simulations), the 2000 CCN cm^{-3} simulation appears to match the observations best in the low-levels (1.1km AGL; Fig. 5.1). The

overall size and extent of the storm is similar to radar observations, with a weak hook echo present. Reflectivity values also matched best to observations in the 2000 CCN simulation. A bounded weak echo region was observed at this time, which is roughly produced in the 500 and 2000 CCN cm^{-3} simulations, but not in the other three CCN concentrations. Observations at this time also show a weak rear-flank downdraft, which is present in all five simulations, but the spatial extent of the downdraft matches best at the higher CCN simulations. Updraft sizes and locations are most similar to the observations in the 300 and 500 CCN cm^{-3} simulations, located mainly along the inflow notch.

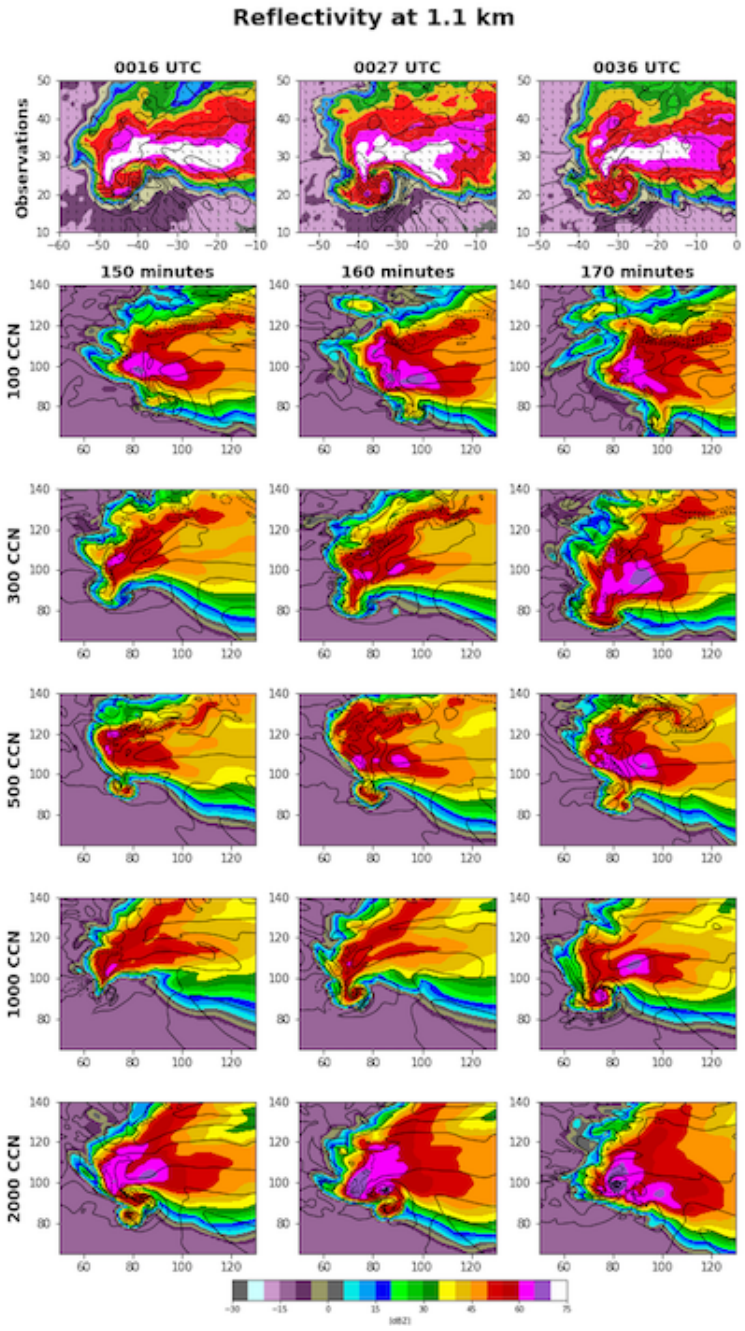

Figure 5.1: Top Row: Aerial view of reflectivity at 1.1km AGL shaded every 10 dBZ and vertical velocity contoured in black every 5 m/s for 0016, 0027, and 0036 UTC 30 May 2004 from SMART radar observations. Rows 2-6: Same as Row 1, but for simulations at 150, 160, and 170 minutes for 100, 300, 500, 1000, and 2000 CCN, respectively. X and Y axis in kilometers (km) from domain/radar center

At this time, reflectivities in the mid-levels (4.6 km AGL, Fig. 5.2) are weaker than closer to the surface; however all five simulations produced reflectivities roughly 10 dBZ weaker then observed. The shape and extent of these reflectivities best matched the 300, 500, and 1000 CCN cm^{-3} cases, with a weak hook and broad bounded weak echo region. Observations at this level, show a split maximum updraft in this bounded weak echo region, while the simulations all produced one broad updraft. Cross-sections at 45^o from southwest to northeast were taken through the rear-flank, updraft, and anvil regions. At 0016, a large region of high reflectivity is present in the rear flank and above the updraft (Fig. 5.3). The cross sections through the model simulations all seemed rather reasonable compared to observations, with the exception of the 300 CCN cm^{-3} case in terms of shape and extent. At the surface below the updraft is a secondary region of relatively higher reflectivities. This lower reflectivity region is only seen in the 2000 CCN cm^{-3} case. A split updraft maximum is also observed in the observations at this time, with magnitudes of 60 and 30 ms^{-1}, but only a single updraft was produced by the model at this time. All five concentrations preformed rather well simulating the updraft magnitude and size.

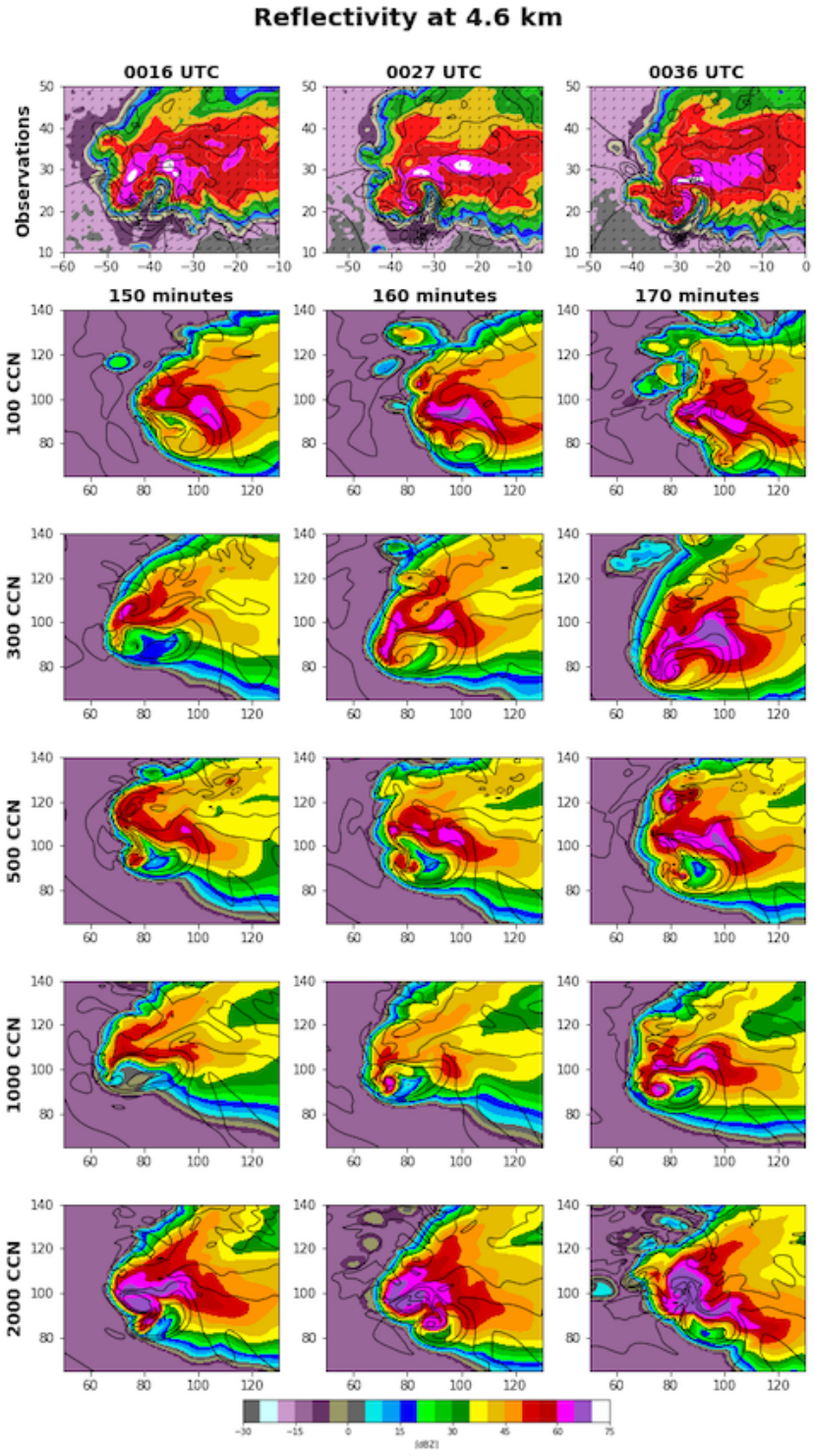

Figure 5.2: Same as Fig.5.1 but for 4.5km AGL

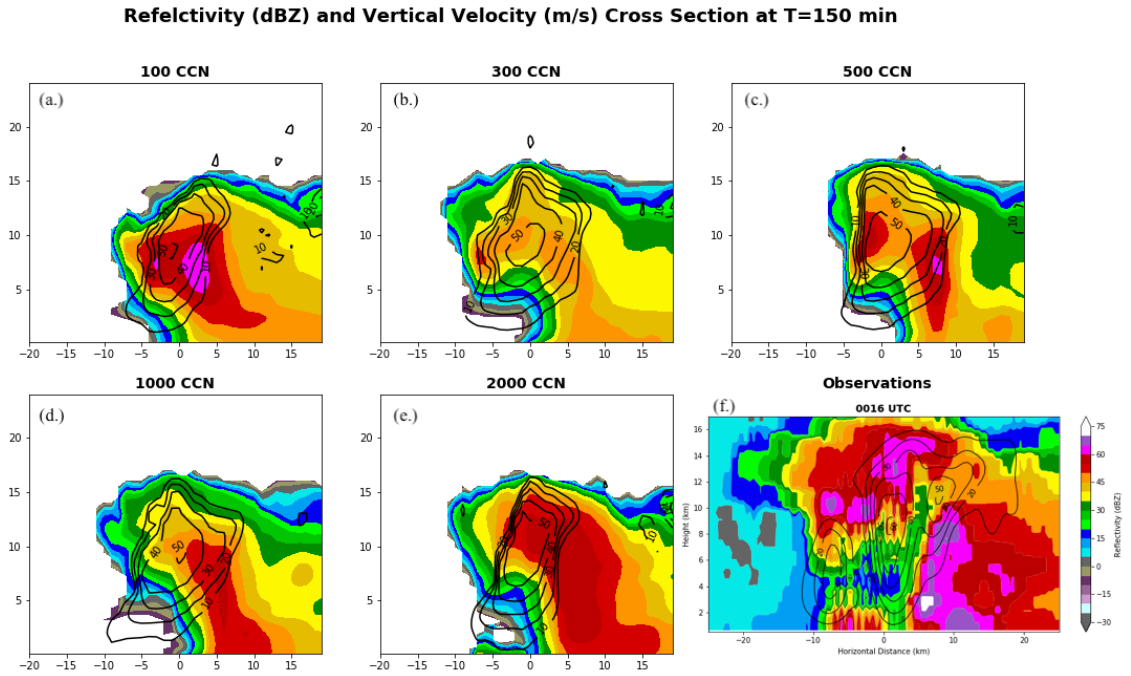

Figure 5.3: a-e.) Cross sections taken at 45^o of reflectivity shaded every 10 dBZ and vertical velocity contoured every 10 m/s for simulations at 150 minutes with 100, 300, 500, 1000, and 2000 CCN, respectively. f.) Cross-section of observed radar reflectivity every 10 dBZ and vertical vetical velocity contoured in black for 0016 UTC 30 May 2004.

At 0027 UTC (T=160 minutes in the simulations), the 1000 CCN case matches best with the observations in the low levels (Fig. 5.1). At this time the observed storm has maintained its hook and has begun to form a rear-flank gust front. The rear flank downdraft has strengthened and is now located just west of the inflow notch. The updraft is focused along the southeast edge of the hook echo, and a bounded weak echo region is still very present. The hook, gust front, and updraft region best line up with the 1000 CCN cm^{-3} case at this time. The hook and gust front are also weakly present in the 300 and 500 CCN cm^{-3} cases, but the location and shape of updraft and

downdraft regions are less comparable to observations. In the mid-levels (Fig. 5.2), the hook has become more evident, and the updraft region has become focused just east of the inflow notch. This again, best lined up with the 1000 CNN cm^{-3} simulation. Precipitation along the rear-flank gust front is building in the observations at this level; however this is not yet present in any of the simulations. Reflectivity cross sections (Fig. 5.4) are quite similar to the previous time, but with weaker reflectivities in the rear-flank in the low to mid-levels. The observed secondary updraft has weakened and only a single updraft is present with a larger magnitude of 70 ms^{-1}. The updraft again is generally well simulated; however roughly 10 m s^{-1} weaker than observed. Reflectivities in the anvil region have begun to sink closer to the surface following the weakening of the secondary updraft. This best aligns with the reflectivity pattern in the two higher CCN simulations.

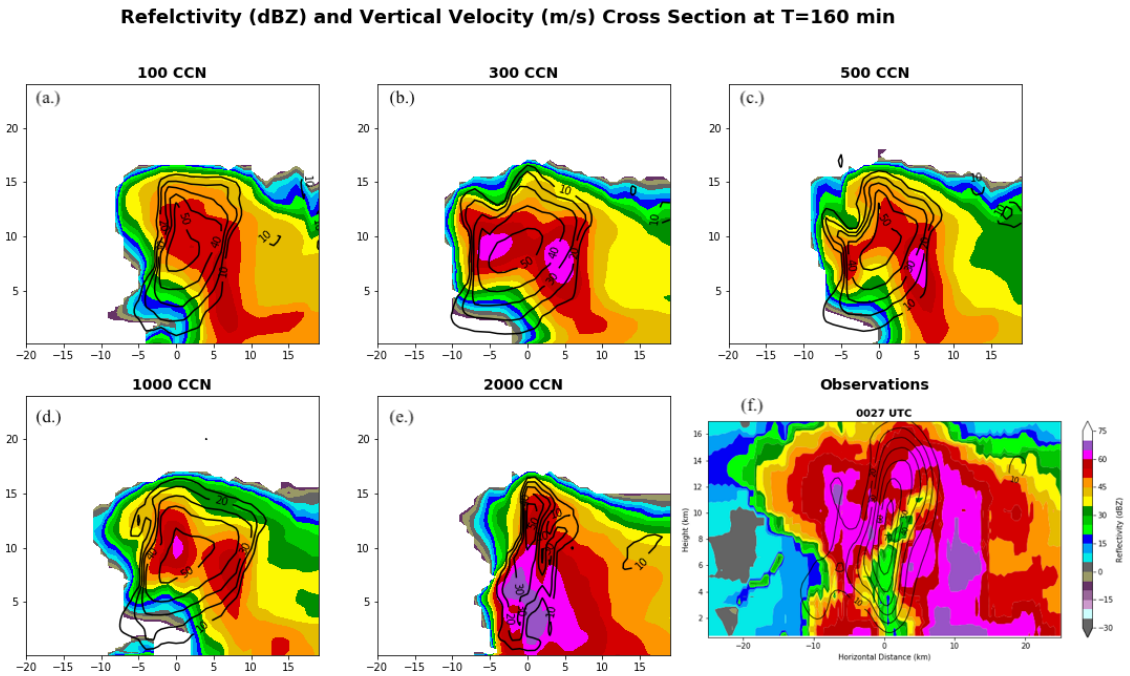

Figure 5.4: Same as Fig.5.3, but for model time T=160 minutes and observation time 0027 UTC

At 0036 UTC (T=170 minutes in the simulations), the observed storm still maintains its hook structure and a rear-flank gust front at low levels (Fig. 5.1). The downdraft remains west of the bounded weak echo region, and the updraft has weakened and broadened but remains just southeast of the hook echo. This aligns best with the 1000 CCN cm^{-3} simulation, which shows the hook, rear flank gust front, updraft and downdraft all in the same regions as observed. In the mid-levels (Fig. 5.2), the hook is still present, but not as defined, with an updraft region just southeast of the inflow notch. Precipitation from the rear flank gust front is also quite prominent now at this time in the mid-levels; however none of the simulations produced this feature at the time of comparison. The 1000 CCN cm^{-3} case again best aligns with observations at this time as it shows a clear hook and an updraft in the observed region. Cross sections (Fig. 5.5), show reflectivities weakening in the rear-flank downdraft at mid-levels, but now completely bound the updraft. This is captured well in the 1000 CCN simulation, although slightly delayed in timing. The updraft has continued to weaken now with a magnitude of only 40 m s^{-1}. All five simulations model this updraft core well but produce updrafts 10 m s^{-1} stronger then observed.

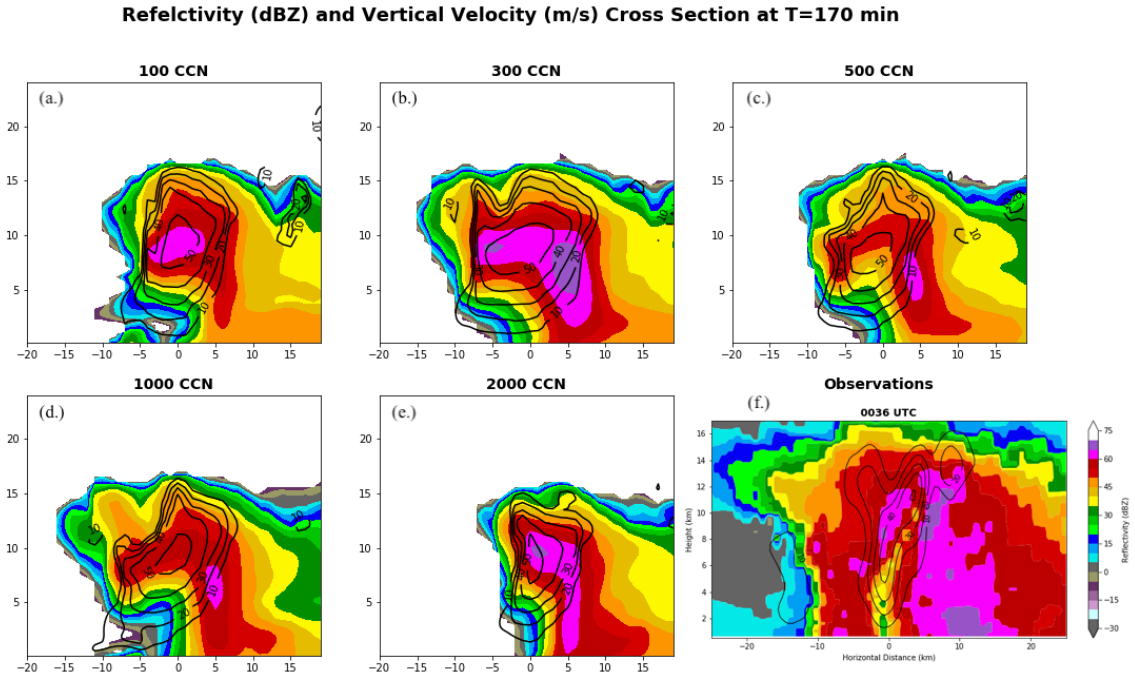

Figure 5.5: Same as Fig.5.3, but for model time T=170 minutes and observation time 0036 UTC

5.1.2 Electric Structure and Evolution

The electric structure of the storm can be inferred from the characteristics of the VHF sources observed by the OKLMA. Following standard expectations of a bidirectional flash (Kasemir, 1960; Mazur and Ruhnke, 1993; Rison et al., 2016; MacGorman et al., 1981; Coleman et al., 2003) and expected differences in negative and positive breakdown, we can infer the polarity of the charge structure of the storm from the characteristics of the VHF sources. At 0016 UTC (Fig. 5.6f), the rear flank shows mostly sources suggesting positive charge, but with a small pocket of negative charge around 12 km in altitude. Another pocket of negative charge exists above the updraft at an altitude of 10 km; however a lot of unassigned VHF sources are also located above the updraft suggesting a rather complex charge structure. The anvil region

shows mostly positive charge with a thin layer of unassigned sources around 12 km. Looking at the cross sections of electric potential, the structure in the higher CCN cases most resembled that of the VHF observations.

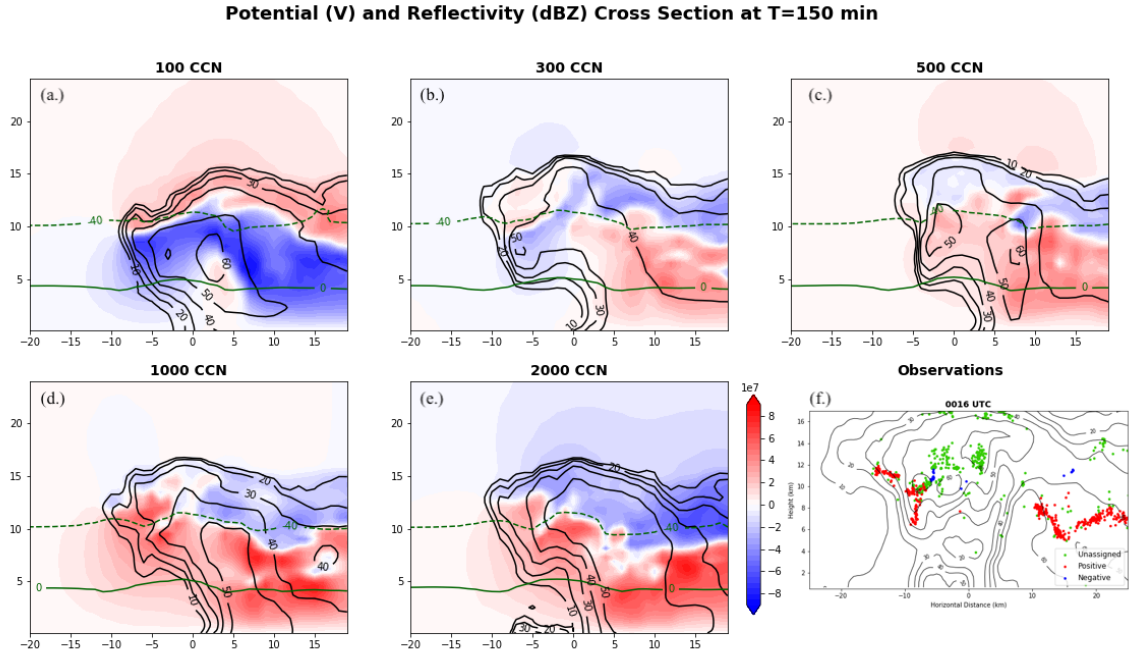

Figure 5.6: a-e.) Cross sections taken at 45^o of simulated electric potential (V), reflectivity contoured in black every 10 dB, and ambient temperature (^{o}C) contoured in green for simulations at 150 minutes with 100, 300, 500, 1000, and 2000 CCN, respectively. f.) Cross-section of observed radar reflectivity every 10 dBZ contoured in black and potential assigned VHF sources as red, green, and blue markers (positive, negative, unassigned, respectively) for 0016 UTC.

At 0027 UTC (Fig. 5.7f), VHF sources along the cross-section suggest a positive charge region below 10 km in the rear flank, with small pockets of negative charge around an altitude of 12 km. In the updraft region, sources suggest mostly positive charge below 10 km, with a lot of unassigned sources above 12 km. The anvil/forward flank sources suggest a layer of positive charge around 9 km and a small layer of

negative charge around 10 km. A pocket of unassigned sources around 12 km, suggests the charge structure in this region is relatively complicated. This observed structure resembles the simulated structure of all but the lowest CCN concentration, which produces a charge structure opposite in polarity to that produced by the higher four concentrations.

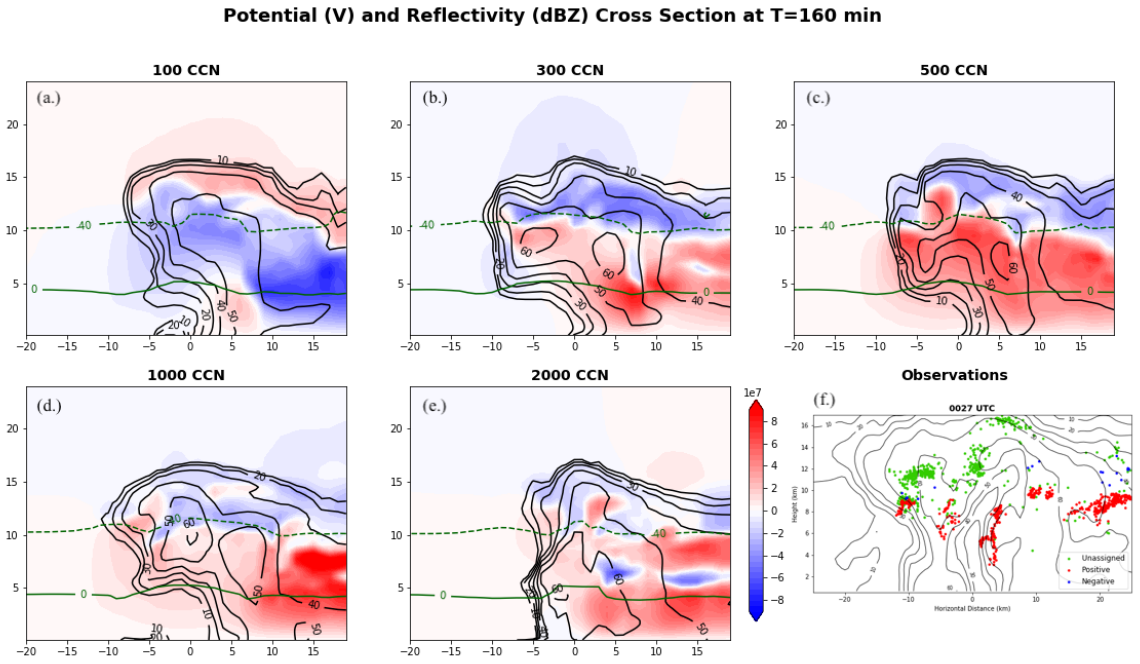

Figure 5.7: Same as Fig.5.6, but for model time T=160 minutes and observation time 0027 UTC

At 0036 UTC (Fig. 5.8f), VHF sources along the cross-section suggest the rear flank has positive charge clustered between 6 and 10 km, and negative charge clustered above 10 km. Above the updraft a cluster of negative charge is observed around 10 km, and a region of unassigned VHF sources exists above that. Moving toward the anvil the inferred structure becomes more complicated with a positive charge layer around 6 km, negative charge layer around 9 km, and positive charge around 11 km. The structure in this region is further complicated by the large cluster of unassigned sources. This

source structure best resembles the more complex electric potential structure of the 1000 CCN cm^{-3} simulation.

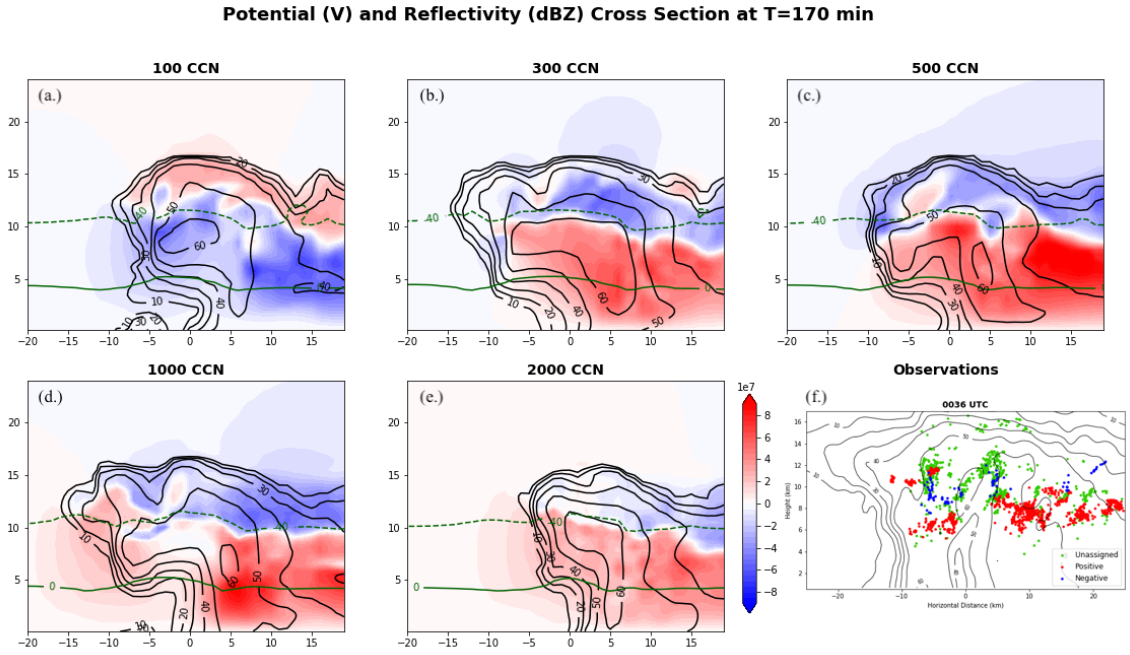

Figure 5.8: Same as Fig.5.6, but for model time T=170 minutes and observation time 0036 UTC

No one simulation perfectly matched the evolution of the dynamic and electric structure of the observed Geary, OK supercell. At 0016 UTC, the middle three CCN concentrations resembled the observed storm, but when it came to the overall evolution of the simulations the 1000 CCN cm^{-3} case best lined up with the observations, especially in the electric evolution. At the time the storm was recorded by the SMART radars, a lot of crop dust and wheat fragments were being ingested into the storm's inflow (personal communication M. Biggerstaff, 2021), suggesting that the environment from which storm evolved had a higher CCN concentration which may have played a role in its evolution. This hypothesis is not inconsistent with the results of these

simulations, but the environmental aerosol concentrations were not directly sampled for this case and that lacks substantial uncertainty.

5.2 Kimball, NE

In this section, the control set simulations of this case study are compared to the analysis of CHILL radar data analyzed in Skamarock et al. (2000) and Dye et al. (2000). Only a dynamic comparison was conducted on this case study. No analysis (or observations useful to this study) of the electrical structure of the Kimball storm were recorded. The only lightning observations for this storm would be from the National Lightning Detection Network (NLDN) and interferometer data. The interferometer recorded two-dimensional data (modern interferometer techniques can do more) and thus is not useful like three-dimensional LMA data for identifying breakdown polarity and charge structure. Defer et al. (2001), has details on lightning observations of this supercell, which noted the polarity of CG flashes throughout the evolution of the storm, but this does not provide much information on the actual three-dimensional charge structure. The evolution of our simulations from multicellular to supercellular were best lined up with simulations at 3000 s, 6000 s, and 9000 s and radar observations at 2312, 0005, 0128 UTC 10-11 July 1996, respectively (Fig. 5.9 & 5.10).

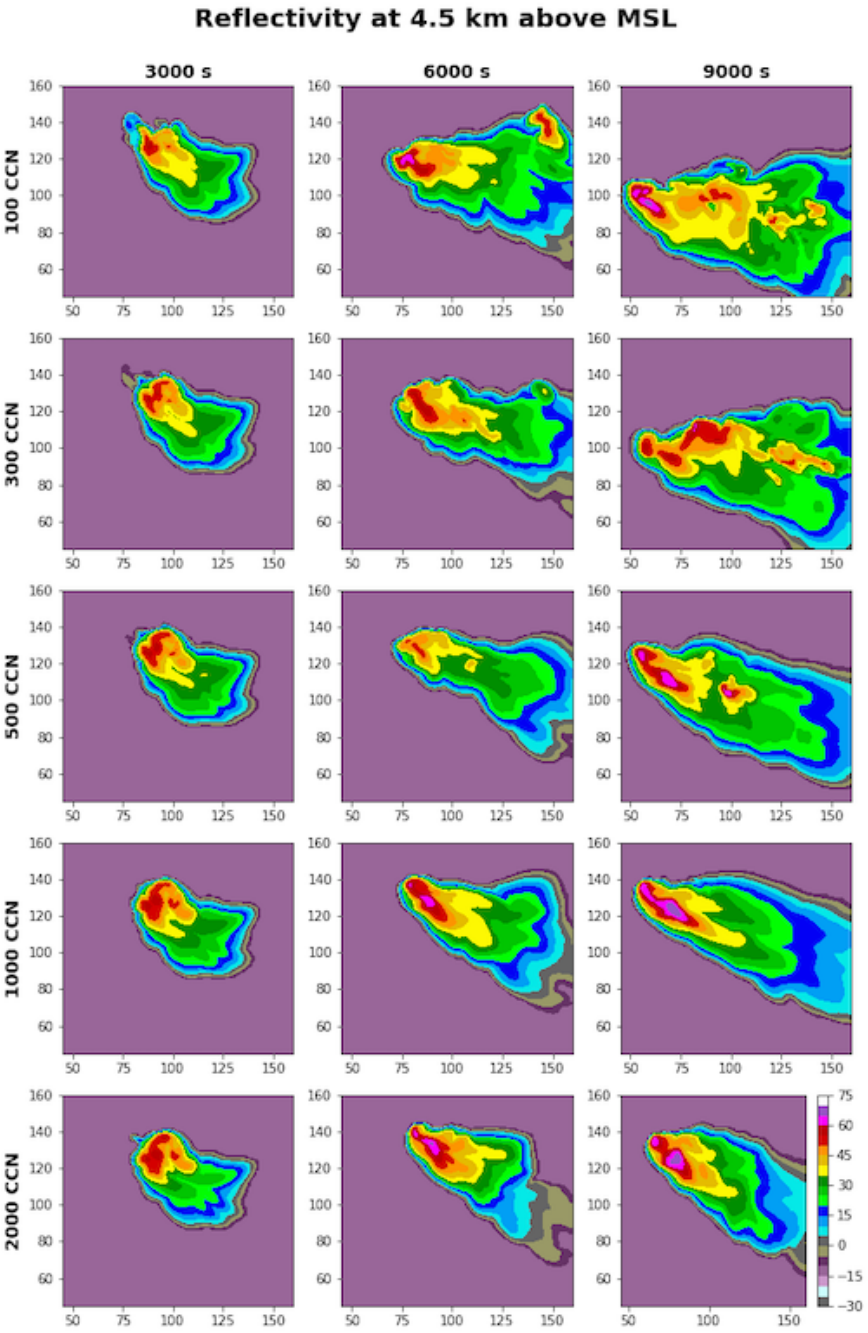

Figure 5.9: Aerial view of reflectivity at 4.5 km MSL (3 km AGL) shaded every 10 dBZ for simulations at 3000 s, 6000 s, and 900 s for Kimball, NE case. Rows 1-5: for simulations at 100, 300, 500, 1000, and 2000 CCN, respectively

5.2.1 Dynamic Structure and Evolution

Observations by the CHILL radar show the storm initially starting off with a multicellular structure at 2312 UTC, with cells taking a northwest to southeast linear pattern (Fig. 5.10b). At 4.5 km MSL (3 km AGL), observed reflectivities were upwards of 55 dBZ with cells remaining relatively compact. Simulations at this time (T=3000 s, or 50 min) all showed a similar multicellular structure with reflectivities all around the same magnitude (Fig. 5.9).

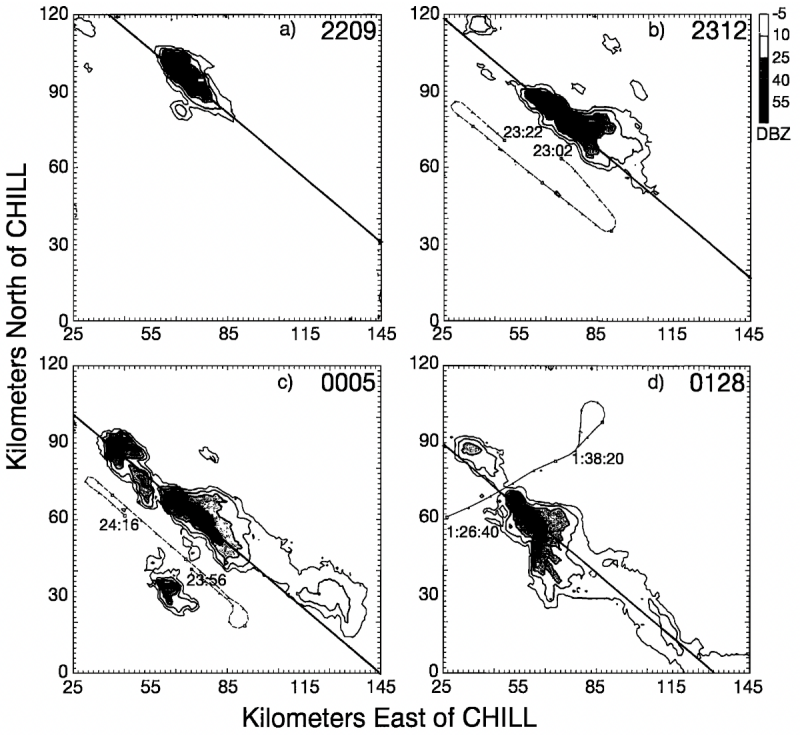

Figure 5.10: Horizontal sections (CAPPIs) from the CSU-CHILL radar for the July 10 storm sowing the reflectivity structure at 4.5 km msl during (a) the early phase, (b and c) the multicellular phase, and (d) the supercellular stage. Tracks of the W3PD are depicted for 20 min segments centered on the time of the CAPPI. Diagonal lines indicate the vertical cross sections shown in Fig.5.13. [Caption and figure adapted from Dye et al. (2000)]

At 10.5 km MSL, observations still show this multi-cellular pattern, but at this level the horizontal extent of these cells are much broader, with reflectivities still around 55 dBZ (Fig. 5.11b). Simulated reflectivities at this time are all still quite similar across the five CCN concentrations (Fig. 5.12). The structure of the simulated storms at 10.5 km all match that of the observations, but reflectivity values are weaker by 20 dBZ. Observed cross-sections at this time show two distinct convective cells (Fig. 5.13b), which is also observed in our simulations (Fig. 5.14(a-e)), with the best matching structure and reflectivities in the three lowest CCN simulations.

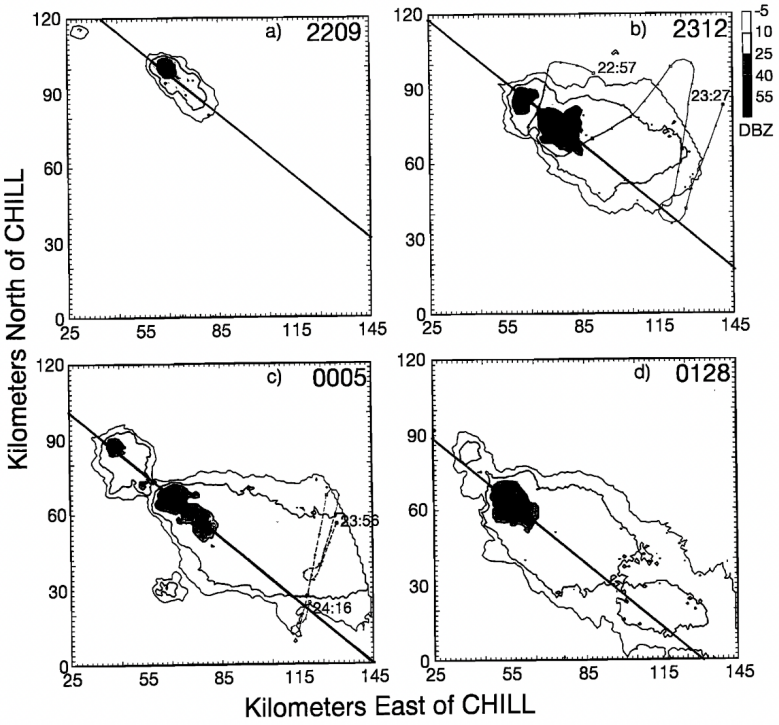

Figure 5.11: Horizontal sections (CAPPIs) from the CSU-CHILL radar for the July 10 storm sowing the reflectivity structure at 10.5 km msl during (a) the early phase, (b and c) the multicellular phase, and (d) the supercellular stage. Tracks of the W3PD are depicted for 20 min segments centered on the time of the CAPPI. Diagonal lines indicate the vertical cross sections shown in Fig.5.13. [Caption and figure adapted from Dye et al. (2000)].

At 0005 UTC (3000s later in the simulation), observations show the cluster of cells have broken apart into 4 cells and one supercell becomes rather distinct from the group (Fig. 5.10c). At 4.5 km, the observed maximum reflectivity of this cell is 55 dBZ. At this time in the simulations (T=6000s or 100 minutes) the different CCN concentrations begin to diverge from one another, with lower CCN concentrations still displaying a semi-multicellular structure and higher CCN displaying a more discreet supercell structure (Fig. 5.9). This seems to be a result of stronger downdrafts and colder outflow triggering secondary convection. At 10.5 km, reflectivity cores appear in the radar analysis, with only two cells having reflectivities over 55 dBZ (Fig. 5.11c). Similar to the lower levels, the simulations at 10.5 km (Fig. 5.12) for lower CCN concentrations display a more multicellular structure while higher CCN display a more discrete supercell structure. The simulated reflectivities of cells at this level were of the same order of magnitude and size as the radar observations, with the exception of the 300 CCN case which was roughly 20 dBZ lower. Observed cross sections at this time (Fig. 5.13c), show two distinct cells with the eastern cell being more horizontally extensive. Comparing this to simulations at this time (Fig. 5.14(f-j)), only the 300, 500, and 1000 CCN cm^{-3} cases display this structure.

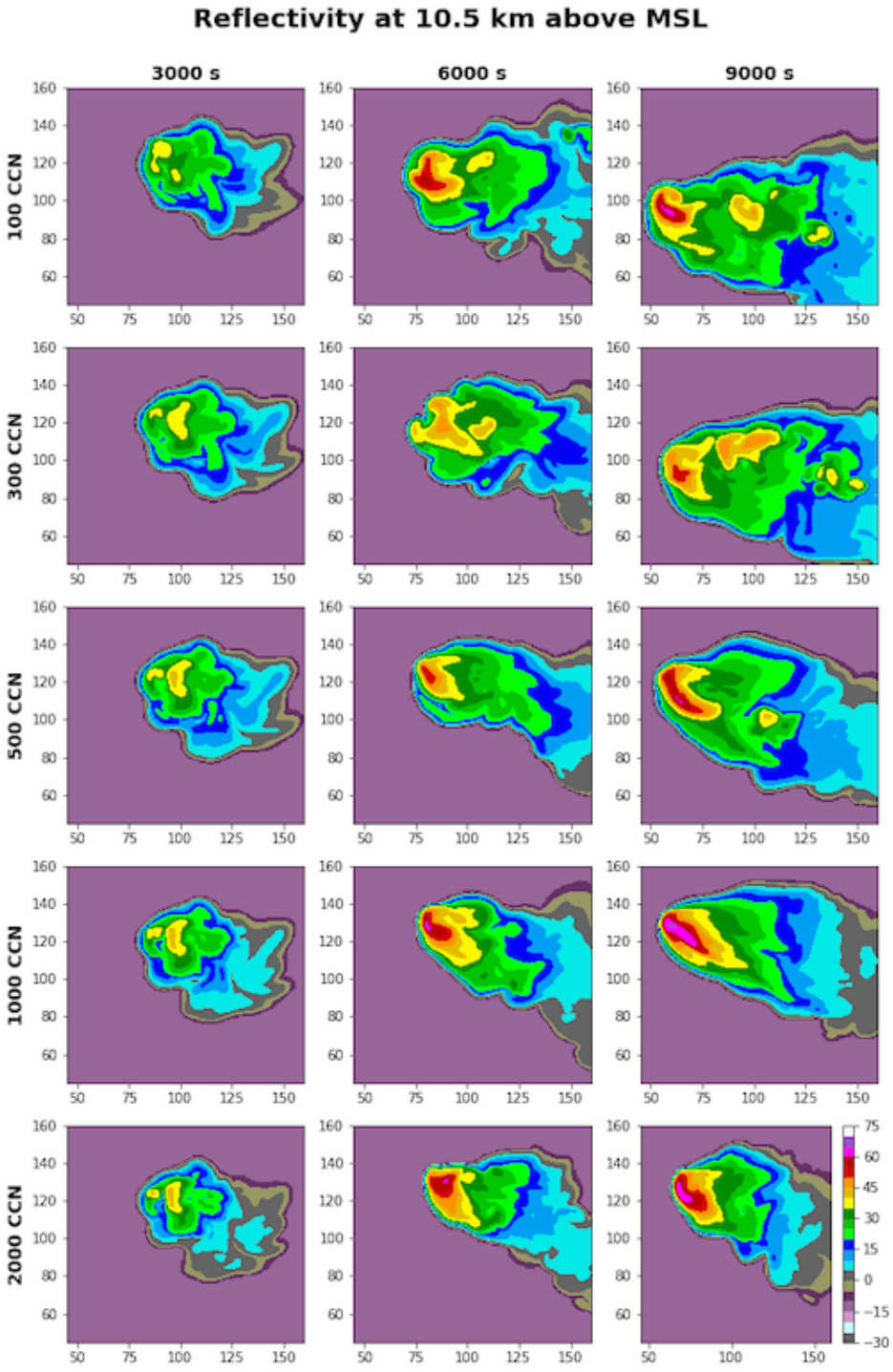

Figure 5.12: Same as Fig.5.9 but at 10.5 km MSL

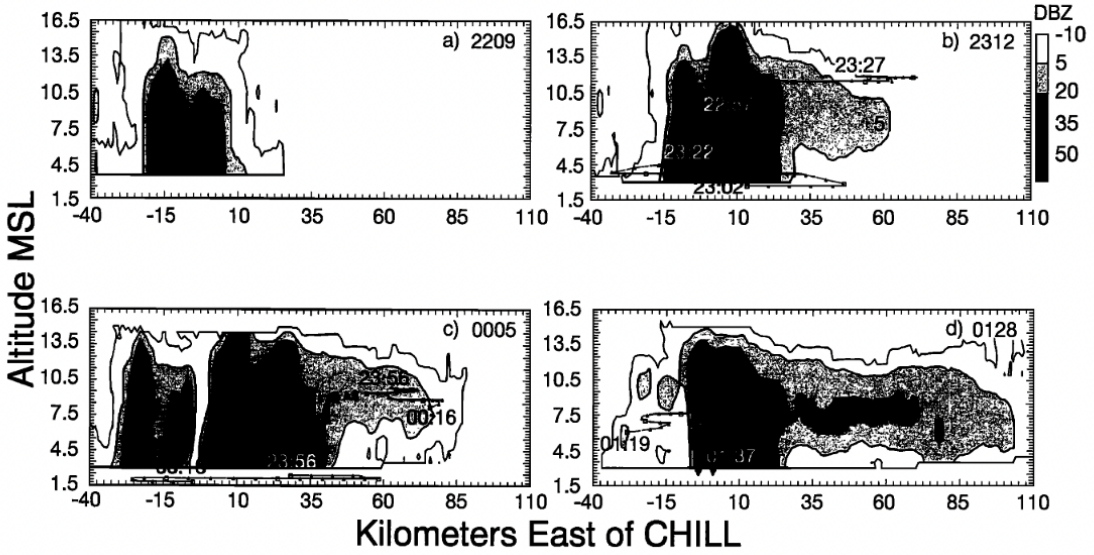

Figure 5.13: Constructed vertical sections through the core of the storm for the same time as those in Figures 10 and 13. The projections of Citation and WP3D tracks are superimposed. [Caption and figure adapted from Dye et al. (2000)]

At 0128, the radar observations show the large cell maintaining its strength but the smaller cells to the northwest and southeast weakening (Fig. 5.10d & 5.11d). In our simulations (Fig. 5.9), the three lowest CCN concentrations show these smaller cells strengthening with time, while the two highest CCN concentrations only display the largest cell. This pattern is also prominent at 10.5 km (Fig. 5.12). Observed cross sections at this time show one singular supercell (Fig. 5.13d). Similar to the Geary, OK case, no singular simulation stood out as a best match to the evolution of the observed storm. Initially, all the simulations closely matched the observations, but diverged over time. Considering mainly the evolution, the 500 and 1000 CCN cm^{-3} cases best resembled the radar analysis, but more detailed observations of electric structure would be beneficial to make this comparison. All five simulations reasonably

modeled the dynamic evolution of the observed supercell, suggesting the environment and microphysics used in the simulations are reasonable. This is turn helps support the case that the model is also doing reasonable things with electrification and its response to changes in CCN concentration.

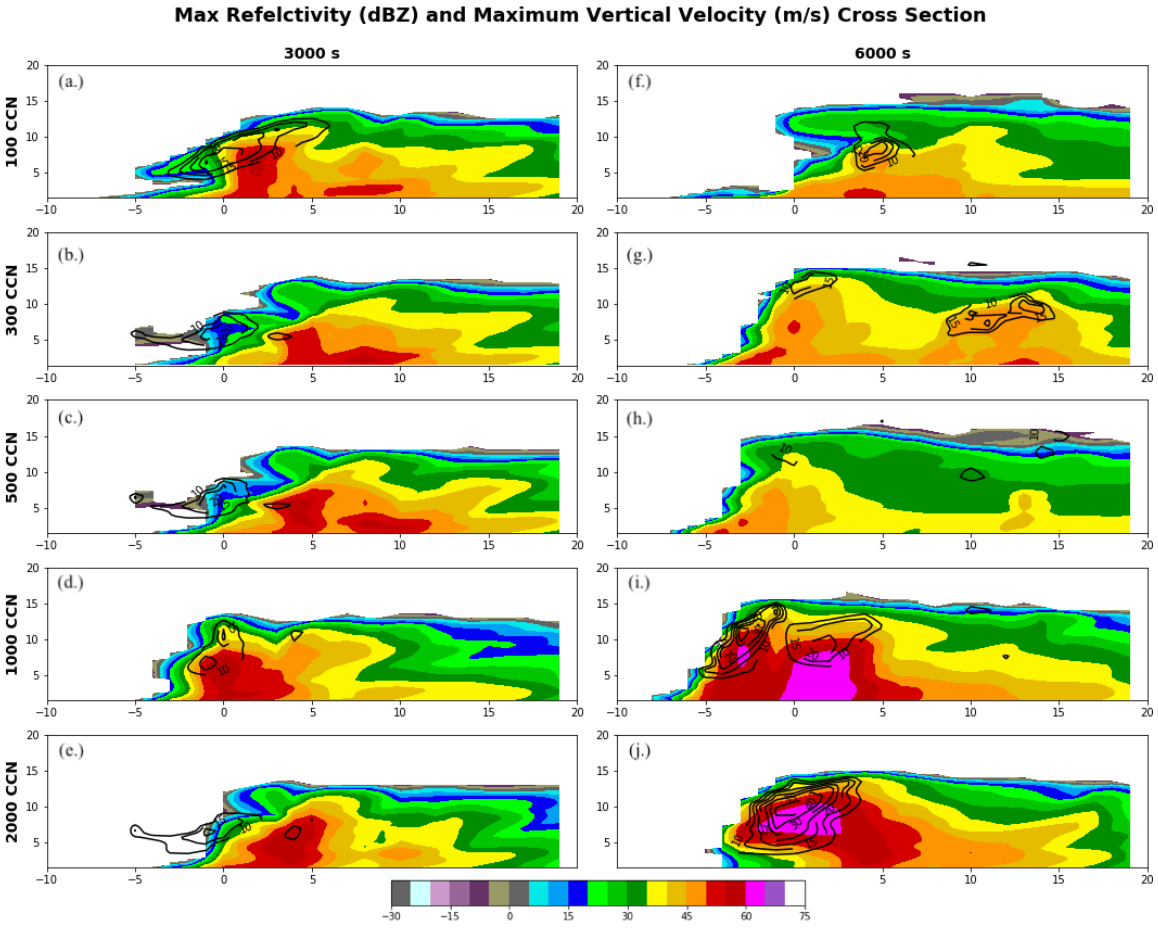

Figure 5.14: Cross sections taken at 150^o of reflectivity shaded every 10 dBZ and vertical velocity contoured every 10 ms^{-1} for simulations with 100, 300, 500, 1000, and 2000 CCN, at simulation times 3000s (a-e.) and 6000 s (f-j.). Altitude in MSL.

Chapter 6

Conclusions

Aerosols and cloud condensation nuclei are known to significantly impact the microphysical, electrical, and dynamic structures of thunderstorms. In this study, CCN influenced the dynamic and electric evolution of both high and low-precipitation supercells. In both cases, similar patterns in dynamic and electric development were seen when adjusting CCN concentrations in each simulation. These results suggest that the influence CCN concentrations has on the evolution of supercells is not largely dependent on the amount of precipitation within the storm and will still have an effect on the dynamic and electric structure of the storm despite the amount of precipitation supported by the background environment.

In both cases, the initial onset of precipitation was delayed at higher CCN concentrations, as more numerous smaller droplets weaken the collision and coalescence ("warm rain") processes. This pattern agrees with the findings of Twomey (1977); Albrecht (1989), and Gunn and Phillips (1957). The altitude of the initial onset of precipitation was also higher at higher CCN concentrations, which indicated a transition from less warm to more cold rain processes at higher CCN concentrations. The overall dynamic evolution of the storm appeared to be affected by CCN concentrations as well. At high CCN concentrations, the storm's evolution was delayed and horizontal extent limited. Warm rain processes and precipitation efficiency resulted in differences in rainfall amounts and hydrometeor sizes influence evaporative cooling near the surface and therefore cold pool formations. In the higher CCN cases, in which there is

less liquid precipitation and more cloud ice, cold pools are smaller and warmer. This set up a positive feedback loop, as smaller and weaker cold pools provide less forcing for secondary convection therefore leading to an overall reduction in convective coverage and intensity, and ultimately resulting in less precipitation and so on. This delayed evolution in more polluted air matches the findings of Storer et al. (2010); Lerach and Cotton (2012), and Khain et al. (2011). In both cases, updraft speed was not substantially affected by CCN concentration, but updraft volumes differed among the five CCN concentrations. Our findings suggest that an increase in CCN concentration results in smaller updraft volumes, and this supports the findings of Fan et al. (2009), who found suppression of convective strength by aerosols in cases where strong windshear is present.

The electric structure and evolution were also affected by CCN concentration. In both cases, higher lightning rates were produced at higher aerosol concentrations. These results are similar to results found by Mansell and Ziegler (2013); Altaratz et al. (2010); Ren et al. (2018); Lerach and Cotton (2012), and Kochtubajda et al. (2011). In these studies, lighting rates peaked at an intermediate CCN concentration, but our results had closer to a monotonic pattern. This pattern may change if the study were expanded to include higher CCNC. Flash rates were much lower under the TAK scheme then under the SP98 NI scheme but still produced the same trend with more flashes at higher CCN concentrations. The altitude of flash initiations was also found to differ with CCN concentrations. All five CCN concentrations produced the majority of initiations at 10 km for Geary and 8 km for Kimball. With the SP98 scheme, two additional layers of flash initiations were produced above and below the main layer. In both cases, these additional layers were not active at higher CCN concentrations. This pattern was not observed under the TAK NI scheme. A delay in the initial flash was only produced in the TAK simulations for Geary, but no delay occurred in the SP98

or any of the Kimball simulations. This lack of delay contradicts the findings of Sun et al. (2021). Average flash areas also differed among the simulations, although this was depended more on the NI scheme used. With the SP98 NI scheme, flash areas were smaller at higher CCN concentrations, which follows the typical inverse relationship between flash rates and areas (e.g., Bruning and Macgorman, 2013). With the TAK scheme, flash areas either remained constant or were larger at higher CCN concentrations, which would contradict the expected relationship between flash rates and areas mentioned above. Analysis of electric potential layers suggests that the difference between the two NI charging schemes is a response to the changing microphysical conditions and the horizontal homogeneity over which that occurs. Both NI schemes produced flash area distributions which became narrower at high CCN concentrations, suggesting that at high CCN flash areas remained more homogeneous in size.

The electric structure of the storm was very dependent on the NI charging scheme used, as seen in previous studies (Helsdon et al., 2001; Mansell et al., 2005). In both cases under the SP98 NI scheme, at low CCN the net charge structure could be described as a positive (normal) dipole structure, but at higher CCN the net charge structures were closer to inverted dipole structures with pronounced upper positive screening layers. In both cases at 300 CCN cm^{-3} the net polarity evolved throughout the simulation, suggesting that at this concentration a transition between dominant NI charging mechanisms exists. Higher net charge densities occurred at higher CCN concentrations due to more ice particles participating in the electrification process, following the findings of Sun et al. (2021) and Zhao et al. (2015). Uusing the TAK NI scheme, simulations with low CCN produced an inverted dipole structure, while at higher CCN additional negative charge in the screening layer was observed above 15 km, which was different to the range of structures produced by the SP98 NI scheme. Cross-sections of the storms revealed that the charge structures of these supercells are

more complex than their domain-averaged charge densities, with simulations using the SP98 scheme producing a lot of small pockets of charge, especially above the updraft region, while the TAK scheme had more consistent and continuous charge layers, which contributed to the different flash sizes produced.

Comparing to observations, none of the Geary case simulations stood out as a best match for all features, but the 1000 CCN experiment from the control set of runs matched the evolution of this storm well, especially in the electrical evolution. This suggests the environment in which the Geary, OK supercell evolved in may have contained more polluted air. From the dynamic evolution alone, the Kimball, NE case observations best matched those to the 300 and 1000 CCN simulations, with the other three CCN concentrations still producing supercells reasonably similar to the observed storm, suggesting the environment and microphysics used in the simulations are reasonable. This helps support the case that model is also doing reasonable things with electrification and its response to changes in CCN concentration.

The work in this study could be expanded by modeling a broader range of CCN concentrations, like that of Mansell and Ziegler (2013). This would give a more detailed look at the microphysical and dynamic differences at some intermediate CCN concentrations and detail some complexities in the patterns produced in this study. In particular, the multiple transitions in the polarity of the charge distribution in the 300 CCN simulation may indicate the vicinity of an inflection point in the response to changes in CCN concentrations, so an analysis of CCN concentrations slightly above and below 300 cm^{-3} may be useful to explore the details of the changes in microphysical conditions and how they impact the NI charging mechanism across the inflection point. A comparison involving a broader range of storm environments would also be beneficial to this study. This would provide a more comprehensive look into whether the observed patterns mentioned above will hold in a variety of supercell environments.

Reference List

Albrecht, B. a., 1989: Aerosols, Cloud Microphysics, and Fractional Cloudiness. *Science*, **245**, 1227–1230.

Altaratz, O., I. Koren, Y. Yair, and C. Price, 2010: Lightning response to smoke from Amazonian fires. *Geophysical Research Letters*, **37 (7)**, 1–6, doi:10.1029/2010GL042679.

Baker, B., M. B. Baker, E. R. Jayaratne, J. Latham, and C. P. Saunders, 1987: The Influence of Diffusional Growth Rates On the Charge Transfer Accompanying Rebounding Collisions Between Ice Crystals and Soft Hailstones. *Quarterly Journal of the Royal Meteorological Society*, **113 (478)**, 1193–1215, doi:10.1002/qj.49711347807.

Baker, M., and J. Dash, 1994: Mechanism of charge transfer between colliding ice particles in thunderstorms. *Journal of Geophysical Research*, **99**, 10 621–10 626.

Balsara, D. S., and C. W. Shu, 2000: Monotonicity preserving weighted essentially non-oscillatory schemes with increasingly high order of accuracy. *Journal of Computational Physics*, **160 (2)**, 405–452, doi:10.1006/jcph.2000.6443.

Barth, M. C., and Coauthors, 2007: Cloud-scale model intercomparison of chemical constituent transport in deep convection. *Atmospheric Chemistry and Physics*, **7 (18)**, 4709–4731, doi:10.5194/acp-7-4709-2007.

Betten, D. P., M. I. Biggerstaff, and C. L. Ziegler, 2018: Three-Dimensional Storm Structure and Low-Level Boundaries at Different Stages of Cyclic Mesocyclone Evolution in a High-Precipitation Tornadic Supercell. *Advances in Meteorology*, **2018**, 1–24, doi:10.1155/2018/9432670.

Biggerstaff, M. I., and Coauthors, 2005: The Shared Mobile Atmospheric Research and Teaching Radar: A Collaboration to Enhance Research and Teaching. *Bulletin of the American Meteorological Society*, **86 (9)**, 1263–1274, doi:10.4324/9780203461549-14.

Brooks, I., C. P. Saunders, R. Mitzeva, and S. L. Peck, 1997: The effect on thunderstorm charging of the rate of rime accretion by graupel. *Atmospheric Research*, **43**, 277–295.

Brothers, M. D., E. C. Bruning, and E. R. Mansell, 2018: Investigating the relative contributions of charge deposition and turbulence in organizing charge within a thunderstorm. *Journal of the Atmospheric Sciences*, **75 (9)**, 3265–3284, doi:10.1175/JAS-D-18-0007.1.

Bruning, E. C., and D. R. Macgorman, 2013: Theory and observations of controls on lightning flash size spectra. *Journal of the Atmospheric Sciences*, **70 (12)**, 4012–4029, doi:10.1175/JAS-D-12-0289.1.

Calhoun, K. M., D. R. Macgorman, C. L. Ziegler, and M. I. Biggerstaff, 2013: Evolution of lightning activity and storm charge relative to dual-doppler analysis of a high-precipitation supercell storm. *Monthly Weather Review*, **141 (7)**, 2199–2223, doi:10.1175/MWR-D-12-00258.1.

Calhoun, K. M., E. R. Mansell, D. R. Macgorman, and D. C. Dowell, 2014: Numerical simulations of lightning and storm charge of the 29-30 may 2004 geary, Oklahoma, supercell thunderstorm using EnKF mobile radar data assimilation. *Monthly Weather Review*, **142 (11)**, 3977–3997, doi:10.1175/MWR-D-13-00403.1.

Chmielewski, V. C., D. MacGorman, M. I. Biggerstaff, D. Betten, and C. Ziegler, 2019: How did updraft variations in the geary supercell influence local electrification?, in Ninth Conference on the Meteorological Applications of Lightning Data, page P1.6, Phoenix, AZ. American Meteorological Society.

Chmielewski, V. C., D. R. MacGorman, C. L. Ziegler, E. DiGangi, D. Betten, and M. Biggerstaff, 2020: Microphysical and Transportive Contributions to Normal and Anomalous Polarity Subregions in the 29–30 May 2012 Kingfisher Storm. *Journal of Geophysical Research: Atmospheres*, **125 (16)**, 1–26, doi:10.1029/2020JD032384.

Coleman, L. M., T. C. Marshall, M. Stolzenburg, T. Hamlin, P. R. Krehbiel, W. Rison, and R. J. Thomas, 2003: Effects of charge and electrostatic potential on lightning propagation. *Journal of Geophysical Research: Atmospheres*, **108 (9)**, 1–27, doi:10.1029/2002jd002718.

Coniglio, M. C., D. J. Stensrud, and L. J. Wicker, 2006: Effects of upper-level shear on the structure and maintenance of strong quasi-linear mesoscale convective systems. *Journal of the Atmospheric Sciences*, **63 (4)**, 1231–1252, doi:10.1175/JAS3681.1.

Dawson, D. T., E. R. Mansell, Y. Jung, L. J. Wicker, M. R. Kumjian, and M. Xue, 2014: Low-level ZDR signatures in supercell forward flanks: The role of size sorting and melting of hail. *Journal of the Atmospheric Sciences*, **71 (1)**, 276–299, doi:10.1175/JAS-D-13-0118.1.

Defer, E., P. Blanchet, C. Théry, P. Laroche, J. E. Dye, M. Venticinque, and K. Cummins, 2001: Lightning activity for the July 10, 1996, storm during the Stratosphere-Troposphere Experiment: Radiation, Aerosol, and Ozone-A (STERAO-A) experiment. *Journal of Geophysical Research*, **106 (D10)**, 10 151–10 172.

Dye, J., and Coauthors, 2000: An Overview of the Stratospheric-Tropospheric Experiment: Radiation, Aerosols, and Ozone (STERAO)-Deep Convection experiment with

results for the July 10, 1996 storm. *Journal of Geophysical Research Atmospheres*, **105 (D8)**, 10 023–10 045.

Fan, J., and Coauthors, 2009: Dominant role by vertical wind shear in regulating aerosol effects on deep convective clouds. *Journal of Geophysical Research*, **114 (7)**, 1–9, doi:10.1029/2009JD012352.

Fuchs, B., E. C. Bruning, S. A. Rutledge, L. D. Carey, P. R. Krehbiel, and W. Rison, 2016: Climatological analyses of LMA data with an open-source lightning. *Journal of Geophysical Research Atmospheres*, 8625–8648, doi:10.1002/2015JD024663.

Gish, O. H., 1944: Evaluation and interpretation of the columnar resistance of the atmosphere. *Journal of Geophysical Research*, **49 (3)**, 159–168, doi:https://doi-org.ezproxy.lib.ou.edu/10.1029/TE049i003p00159.

Gunn, R., and B. B. Phillips, 1957: An Experimental Investigation of the Effect of Air Pollution on the Initiation of Rain. *Journal of Meteorology*, **14 (3)**, 272–280.

Helsdon, J. H., W. A. Wojcik, and R. D. Farley, 2001: Examination of thunderstorm-charging mechanism using a two-dimensional strom electrification model. *Journal of Geophysical Research*, **106 (D1)**, 1165–1192.

Hu, J., and Coauthors, 2019: Polarimetric Radar Convective Cell Tracking Reveals Large Sensitivity of Cloud Precipitation and Electrification Properties to CCN. *Journal of Geophysical Research: Atmospheres*, **124 (22)**, 12 194–12 205, doi:10.1029/2019JD030857.

Jayaratne, E. R., and C. P. R. Saunders, 1983: Charge on ice crystals in laboratory clouds. *Journal of Geophysical Research: Oceans*, **88 (C9)**, 5494–5496, doi:https://doi.org/10.1029/JC088iC09p05494, URL https://agupubs.onlinelibrary.wiley.com/doi/abs/10.1029/JC088iC09p05494, https://agupubs.onlinelibrary.wiley.com/doi/pdf/10.1029/JC088iC09p05494.

Jiang, G.-S., and C.-W. Shu, 1996: Efficient Implementation of Weighted ENO Schemes. *Journal of Computational Physics*, **126**, 202–228, doi:10.7551/mitpress/11358.003.0009.

Jouan, C., and J. A. Milbrandt, 2019: The importance of the ice-phase microphysics parameterization for simulating the effects of changes to CCN concentrations in deep convection. *Journal of the Atmospheric Sciences*, **76 (6)**, 1727–1752, doi:10.1175/JAS-D-18-0168.1.

Kalina, E. A., K. Friedrich, H. Morrison, and G. H. Bryan, 2014: Aerosol effects on idealized supercell thunderstorms in different environments. *Journal of the Atmospheric Sciences*, **71 (12)**, 4558–4580, doi:10.1175/JAS-D-14-0037.1.

Kasemir, H. W., 1960: A contribution to the electrostatic theory of a lightning discharge. *Journal of Geophysical Research*, **65 (7)**, 1873–1878, doi:10.1029/jz065i007p01873.

Khain, A., D. Rosenfeld, and A. Pokrovsky, 2005: Aerosol impact on the dynamics and microphysics of deep convective clouds. *Quarterly Journal of the Royal Meteorological Society*, **131 (611)**, 2639–2663, doi:10.1256/qj.04.62.

Khain, A., D. Rosenfeld, A. Pokrovsky, U. Blahak, and A. Ryzhkov, 2011: The role of CCN in precipitation and hail in a mid-latitude storm as seen in simulations using a spectral (bin) microphysics model in a 2D dynamic frame. *Atmospheric Research*, **99 (1)**, 129–146, doi:10.1016/j.atmosres.2010.09.015, URL http://dx.doi.org/10.1016/j.atmosres.2010.09.015.

Klemp, J. B., and R. B. Wilhelmson, 1978: The simulation of three-dimensional convective storm dynamics. *Journal of the Atmospheric Sciences*, **35 (6)**, 1070–1096, doi:10.1175/1520-0469(1978)035⟨1070:TSOTDC⟩2.0.CO;2.

Kochtubajda, B., and Coauthors, 2011: Exceptional cloud-to-ground lightning during an unusually warm summer in Yukon, Canada. *Journal of Geophysical Research: Atmospheres*, **116 (21)**, 9502–9523, doi:doi:10.1029/2011JD016080, URL https://doi.org/10.1029/2018JD029006@10.1002/(ISSN)2169-8996.DEEPCON1.

Kuhlman, K. M., A. U.S., and C. Ziegler, 2005: Numerical simulations of the 29 june 2000 steps supercell : Microphysics , electrification , and lightning. *Monthly Weather Review*.

Lance, S., and Coauthors, 2011: Cloud condensation nuclei as a modulator of ice processes in Arctic mixed-phase clouds. *Atmospheric Chemistry and Physics*, **11 (15)**, 8003–8015, doi:10.5194/acp-11-8003-2011.

Lang, T. J., S. A. Rutledge, J. E. Dye, M. Venticinque, P. Laroche, and E. Defer, 2000: Anomalously low negative cloud-to-ground lightning flash rates in intense convective storms observed during STERAO-A. *Monthly Weather Review*, **128 (1)**, 160–173, doi:10.1175/1520-0493(2000)128⟨0160:ALNCTG⟩2.0.CO;2.

Lang, T. J., S. A. Rutledge, and K. C. Wiens, 2004: Origins of positive cloud-to-ground lightning flashes in the stratiform region of a mesoscale convective system. *Geophysical Research Letters*, **31 (10)**, doi:10.1029/2004GL019823.

Lasher-Trapp, S., S. Kumara, D. H. Moser, A. M. Blyth, J. R. French, R. C. Jacksonc, D. C. Leon, and D. M. Plummer, 2018: On different microphysical pathways to convective rainfall. *Journal of Applied Meteorology and Climatology*, **57 (10)**, 2399–2417, doi:10.1175/JAMC-D-18-0041.1.

Lerach, D. G., and W. R. Cotton, 2012: Comparing aerosol and low-level moisture influences on supercell tornadogenesis: Three-dimensional idealized simulations. *Journal of the Atmospheric Sciences*, **69 (3)**, 969–987, doi:10.1175/JAS-D-11-043.1.

Li, Z., F. Niu, J. Fan, Y. Liu, D. Rosenfeld, and Y. Ding, 2011: Long-term impacts of aerosols on the vertical development of clouds and precipitation. *Nature Geoscience*, **4 (12)**, 888–894, doi:10.1038/ngeo1313.

MacGorman, D., and W. Rust, 1985: *The Electrical Nature of Storms*. Oxford University Press, 432 pp.

MacGorman, D. R., A. A. Few, and T. L. Teer, 1981: Layered lightning activity. *Journal of Geophysical Research: Oceans*, **86 (C10)**, 9900–9910, doi:https://doi.org/10.1029/JC086iC10p09900, URL https://agupubs.onlinelibrary.wiley.com/doi/abs/10.1029/JC086iC10p09900, https://agupubs.onlinelibrary.wiley.com/doi/pdf/10.1029/JC086iC10p09900.

MacGorman, D. R., W. D. Rust, P. Krehbiel, W. Rison, E. Bruning, and K. Wiens, 2005: The electrical structure of two supercell storms during STEPS. *Monthly Weather Review*, **133 (9)**, 2583–2607, doi:10.1175/MWR2994.1.

MacGorman, D. R., J. M. Straka, and C. L. Ziegler, 2001: A lightning parameterization for numerical cloud models. *Journal of Applied Meteorology*, **40 (3)**, 459–478, doi:10.1175/1520-0450(2001)040⟨0459:ALPFNC⟩2.0.CO;2.

MacGorman, D. R., and Coauthors, 2008: TELEX The Thunderstorm Electrification and Lightning Experiment. *Bulletin of the American Meteorological Society*, **89 (7)**, 997–1013, doi:10.1175/2007BAMS2352.1.

Maggio, C. R., T. C. Marshall, and M. Stolzenburg, 2009: Estimations of charge transferred and energy released by lightning flashes. *Journal of Geophysical Research: Atmospheres*, **114 (D14)**, doi:https://doi.org/10.1029/2008JD011506, URL https://agupubs.onlinelibrary.wiley.com/doi/abs/10.1029/2008JD011506, https://agupubs.onlinelibrary.wiley.com/doi/pdf/10.1029/2008JD011506.

Mansell, E. R., D. R. MacGorman, C. L. Ziegler, and J. M. Straka, 2002: Simulated three-dimensional branched lightning in a numerical thunderstorm model. *Journal of Geophysical Research D: Atmospheres*, **107 (9-10)**, 2–1, doi:10.1029/2000jd000244.

Mansell, E. R., D. R. MacGorman, C. L. Ziegler, and J. M. Straka, 2005: Charge structure and lightning sensitivity in a simulated multicell thunderstorm. *Journal of Geophysical Research D: Atmospheres*, **110 (12)**, 1–24, doi:10.1029/2004JD005287.

Mansell, E. R., and C. L. Ziegler, 2013: Aerosol effects on simulated storm electrification and precipitation in a two-moment bulk microphysics model. *Journal of the Atmospheric Sciences*, **70 (7)**, 2032–2050, doi:10.1175/JAS-D-12-0264.1.

Mansell, E. R., C. L. Ziegler, and E. C. Bruning, 2010: Simulated electrification of a small thunderstorm with two-moment bulk microphysics. *Journal of the Atmospheric Sciences*, **67 (1)**, 171–194, doi:10.1175/2009JAS2965.1.

Marshall, T. C., W. D. Rust, and M. Stolzenburg, 1995: Electrical structure and updraft speeds in thunderstorms over the southern great plains. *Journal of Geophysical Research: Atmospheres*, **100 (D1)**, 1001–1015, doi:https://doi.org/10.1029/94JD02607, URL https://agupubs.onlinelibrary.wiley.com/doi/abs/10.1029/94JD02607, https://agupubs.onlinelibrary.wiley.com/doi/pdf/10.1029/94JD02607.

Mason, B., and J. Dash, 2000: Charge and mass transfer in ice-ice collisions: Experimental observations of a mechanism in thunderstorm electrification. *Journal of Geophysical Research*, **105**, 10 185–10 192.

Mazur, V., and L. H. Ruhnke, 1993: Common physical processes in natural and artificially triggered lightning. *Journal of Geophysical Research*, **98 (D7)**, doi:10.1029/93jd00626.

Mitzeva, R., J. Latham, and S. Petrova, 2006: A comparative modeling study of the early electrical development of maritime and continental thunderstorms. *Atmospheric Research*, **82 (1-2)**, 26–36, doi:10.1016/j.atmosres.2005.01.006.

Mohr, C. G., J. L. Miller, R. L. Vaughan, and H. W. Frank, 1986: The Merger of Mesoscale Datasets into a Common Cartesian Format of Efficient ad Systematic Analysis. *Journal of Oceanic and Atmospheric Technologies*, 143–161.

Pawar, S. D., V. Gopalakrishnan, P. Murugavel, N. E. Veremey, and A. A. Sinkevich, 2017: Possible role of aerosols in the charge structure of isolated thunderstorms. *Atmospheric Research*, doi:10.1016/j.atmosres.2016.09.016.

Pereyra, R. G., E. E. Avila, and N. E. Castellano, 2000: A laboratory study of graupel charging. *Journal of Geophysical Research*, **105 (D16)**, 20 803–20 812.

Potvin, C. K., L. J. Wicker, M. I. Biggerstaff, D. Betten, and A. Shapiro, 2013: Comparison between dual-doppler and EnKF storm-scale wind analyses: The 29-30 May 2004 Geary, Oklahoma, supercell thunderstorm. *Monthly Weather Review*, **141 (5)**, 1612–1628, doi:10.1175/MWR-D-12-00308.1.

Pruppacher, H., and J. Klett, 1978: *Microphysics of Clouds and Precipitation*. Springer, 954 pp.

Ren, T., A. D. Rapp, S. L. Nasiria, J. R. Mecikalski, and J. Apke, 2018: Is the awareness of the aerosol state useful in predicting enhanced lightning for lightning-producing storms over Northern Alabama? *Journal of Applied Meteorology and Climatology*, **57 (8)**, 1663–1681, doi:10.1175/JAMC-D-17-0182.1.

Reynolds, S., M. Brook, and M. Gourley, 1957: Thunderstorm Charge Seperation. *Journal of the Atmospheric Sciences*, **14 (5)**, 426–436.

Rison, W., P. R. Krehbiel, M. G. Stock, H. E. Edens, X. M. Shao, R. J. Thomas, M. A. Stanley, and Y. Zhang, 2016: Observations of narrow bipolar events reveal how lightning is initiated in thunderstorms. *Nature Communications*, **7**, doi:10.1038/ncomms10721.

Rosenfeld, D., U. Lohmann, G. B. Raga, C. D. O'Dowd, M. Kulmala, S. Fuzzi, A. Reissell, and M. O. Andreae, 2008: Flood or drought: How do aerosols affect precipitation? *Science*, **321 (5894)**, 1309–1313, doi:10.1126/science.1160606.

Rust, W. D., and T. C. Marshall, 1996: On abandoning the thunderstorm tripole-charge paradigm. *Journal of Geophysical Research: Atmospheres*, **101 (D18)**, 23 499–23 504, doi:https://doi.org/10.1029/96JD01802, URL https://agupubs.onlinelibrary.wiley.com/doi/abs/10.1029/96JD01802, https://agupubs.onlinelibrary.wiley.com/doi/pdf/10.1029/96JD01802.

Rust, W. D., and Coauthors, 2005: Inverted-polarity electrical structures in thunderstorms in the Severe Thunderstorm Electrification and Precipitation Study (STEPS). *Atmospheric Research*, **76 (1-4)**, 247–271, doi:10.1016/j.atmosres.2004.11.029.

Saunders, C. P., H. Bax-Norman, C. Emersic, E. E. Avila, and N. E. Castellano, 2006: Laboratory studies of the effect of cloud conditions on graupel/crystal charge transfer in thunderstorm electrification. *Quarterly Journal of the Royal Meteorological Society*, **132 (621)**, 2653–2673, doi:10.1256/qj.05.218.

Saunders, C. P., and S. L. Peck, 1998: Laboratory studies of the influence of the rime accretion rate on charge transfer during crystal/graupel collisions. *Journal of Geophysical Research Atmospheres*, **103 (D12)**, 13 949–13 956, doi:10.1029/97JD02644.

Saunders, C. P. R., W. D. Keith, and R. P. Mitzeva, 1991: The effect of liquid water on thunderstorm charging. *Journal of Geophysical Research: Atmospheres*, **96 (D6)**, 11 007–11 017, doi:https://doi.org/10.1029/91JD00970, URL https://agupubs.onlinelibrary.wiley.com/doi/abs/10.1029/91JD00970, https://agupubs.onlinelibrary.wiley.com/doi/pdf/10.1029/91JD00970.

Seigel, R. B., and S. C. Van Den Heever, 2012: Dust lofting and ingestion by supercell storms. *Journal of the Atmospheric Sciences*, **69 (5)**, 1453–1473, doi:10.1175/JAS-D-11-0222.1.

Seimon, A., 1993: Anomalous cloud-to-ground lightning in an f5-tornado-producing supercell thunderstorm on 28 august 1990. *Bulletin of the American Meteorological Society*, **74**, 189–204, doi:10.1175/1520-0477(1993)074⟨0189:ACTGLI⟩2.0.CO;2.

Shu, C.-W., 2003: Higher Order Finite Difference and Finite Volume WENO Schemes and Discontinuous Galerkin Methods for CFD. *International Journal of Computational Fluid Dynamics*, **17**, 107–118.

Skamarock, W. C., and Coauthors, 2000: Numerical simulations of the July 10 Stratospheric-Tropospheric: Radiation, Aerosols, and Ozone/Deep Convection Experiment convective system: Kinematics and transport. *Journal of Geophysical Research*, **105 (D15)**, 19 973–19 990.

Solomon, S., Q. D, M. M., M. M., T. M., M. H. L., and Z.Chen, 2007: *Climate Change 2007 - The Physical Science Basis*. Cambridge University Press, 996 pp.

Stocker, T. F., and Coauthors, 2013: *Climate Change 2013 - The Physical Science Basis*. Cambridge University Press, 1535 pp.

Stolzenburg, M., W. D. Rust, and T. C. Marshall, 1998: Electrical structure in thunderstorm convective regions: 3. synthesis. *Journal of Geophysical Research: Atmospheres*, **103 (D12)**, 14 097–14 108, URL https://agupubs.onlinelibrary.wiley.com/doi/abs/10.1029/97JD03545, https://agupubs.onlinelibrary.wiley.com/doi/pdf/10.1029/97JD03545.

Storer, R. L., S. C. Van Den Heever, and G. L. Stephens, 2010: Modeling aerosol impacts on convective storms in different environments. *Journal of the Atmospheric Sciences*, **67 (12)**, 3904–3915, doi:10.1175/2010JAS3363.1.

Straka, J. M., and E. R. Mansell, 2005: A bulk microphysics parameterization with multiple ice precipitation categories. *Journal of Applied Meteorology*, **44 (4)**, 445–466, doi:10.1175/JAM2211.1.

Sun, M., and Coauthors, 2021: Aerosol Effects on Electrification and Lightning Discharges in a Multicell Thunderstorm Simulated by the WRF-ELEC Model. *Atmospheric Chemistry and Physics*, 1–37, doi:doi.org/10.5194/acp-2020-1284.

Takahashi, T., 1978: Riming Electrification as a Charge Generation Mechanism in Thunderstorms. *Journal of the Atmospheric Sciences*, **35**, 1536–1548.

Takahashi, T., 1984: Thunderstorm Electrification - a Numerical Study. *Nature*, **41 (17)**, 2541–2558, doi:10.1175/1520-0469(1984)041⟨2541:TENS⟩2.0.CO;2.

Tao, W.-K., J.-P. Chen, Z. Li, C. Wang, and C. Zhang, 2012: Impact of aerosols on convective clouds and precipitation. *Reviews of Geophysics*, **50 (2)**, doi:https://doi.org/10.1029/2011RG000369, URL https://agupubs.onlinelibrary.wiley.com/doi/abs/10.1029/2011RG000369, https://agupubs.onlinelibrary.wiley.com/doi/pdf/10.1029/2011RG000369.

Thomas, R. J., P. R. Krehbiel, W. Rison, S. J. Hunyady, W. P. Winn, T. Hamlin, and J. Harlin, 2004: Accuracy of the lightning mapping array. *Journal of Geophysical Research D: Atmospheres*, **109 (14)**, 1–34, doi:10.1029/2004JD004549.

Twomey, S., 1977: The Influence of Pollution on the Shortwave Albedo of Clouds. *Journal of the Atmospheric Sciences*, **34 (7)**, 1149–1152.

Wicker, L. J., and W. C. Skamarock, 2002: Time-splitting methods for elastic models using forward time schemes. *Monthly Weather Review*, **130 (8)**, 2088–2097, doi:10.1175/1520-0493(2002)130⟨2088:TSMFEM⟩2.0.CO;2.

Wicker, L. J., and R. B. Wilhelmson, 1995: Simulation and Analysis of Tornado Development and Decay within a Three-Dimensional Supercell Thunderstorm. *Journal of the Atmospheric Sciences*, **52 (15)**, 2675–2703.

Wiens, K. C., S. A. Rutledge, and S. A. Tessendorf, 2005: The 29 June 2000 supercell observed during STEPS. Part II: Lightning and charge structure. *Journal of the Atmospheric Sciences*, **62 (12)**, 4151–4177, doi:10.1175/JAS3615.1.

Williams, E. R., 1989: The tripole structure of thunderstorms. *Journal of Geophysical Research: Atmospheres*, **94 (D11)**, 13 151–13 167, doi:https://doi.org/10.1029/JD094iD11p13151, URL https://agupubs.onlinelibrary.wiley.com/doi/abs/10.1029/JD094iD11p13151, https://agupubs.onlinelibrary.wiley.com/doi/pdf/10.1029/JD094iD11p13151.

Zhao, P., Y. Yin, and H. Xiao, 2015: The effects of aerosol on development of thunderstorm electrification: A numerical study. *Atmospheric Research*, **153 (December)**, 376–391, doi:10.1016/j.atmosres.2014.09.011, URL http://dx.doi.org/10.1016/j.atmosres.2014.09.011.

Ziegler, C. L., 1985: Retrieval of Thermal and Microphysical Variables in Observed Convective Storms. Part 1: Model Development and Preliminary Testing. *Journal of the Atmospheric Sciences*, **42 (14)**, 1487–1509, doi:https://doi.org/10.1175/1520-0469(1985)042%3C1487:ROTAMV%3E2.0.CO;2.